



Balkan Journal of Electrical & Computer Engineering

An International Peer Reviewed, Indexed and Open Access Journal

www.bajece.com

Vol : 3
No : 3
Year : 2015
ISSN : 2147-284X



Sponsored by the

- Istanbul Technical University
- Klaipeda University



This journal is accredited by the Istanbul Technical University subsidy purposes. It is abstracted and indexed in, Index Google Scholarship, the PSCR, DOAJ, Research Bible, Indian Open Access Journals (OAJ), Institutional Repositories (IR), J-Gate (Informatics India), Ulrich's, ResearchGate, International Society of Universal Research in Sciences, DRJI, EyeSource.

General Publication Director & Editor-in-Chief

Ş. Serhat Seker, Istanbul Technical University, Turkey

Vice Editor

Eleonora Guseinoviene, Klaipeda University, Lithuania
Tahir Cetin Akinci, Kirklareli University, Turkey
Yogeshwarsing Calleecharan, University of Mauritius, Mauritius

Editorial board

Amir Tokić, University of Tuzla, Bosnia and Herzegovina
Audrius Senulis, Klaipeda University, Lithuania

Scientific Committee

Abhishek Shukla (India)
Aleksandar Georgiev (Bulgaria)
Ahmet Hamdi Kayran (Turkey)
Arif M. Hasimov (Azerbaijan)
Arunas Lipnickas (Lithuania)
Belgin E. Turkyay (Turkey)
Belle R. Upadhyaya (USA)
Brijender Kahanwal (India)
Daniela Dzhonova-Atanasova (Bulgaria)
Ferhat Sahin (USA)
Gursel Alici (Australia)
Hakan Temeltaş (Turkey)
Ibrahim Akduman (Turkey)
Jan Izykowski (Poland)
Javier Bilbao Landatxe (Spain)
Kunihiko Nabeshima (Japan)
Lambros Ekonomou (Greece)
Marcel Istrate (Romania)
Mehmet Korurek (Turkey)
Marija Eidukeviciute (Lithuania)
Milena Lazarova (Bulgaria)
Muhammad Hadi (Australia)
Muhamed Turkanović (Slovenia)
Mourad Houabes (Algerie)
Murari Mohan Saha (Sweden)
Okyay Kaynak (Turkey)
Osman Nuri Ucan (Turkey)
Ozgur E. Mustecaplioglu (Turkey)
Padmanaban Sanjeevikumar (India)
Rumen Popov (Bulgaria)
Tuiebakhova Zoya Kaimovna (Kazakhstan)
Sead Berberovic (Croatia)
Seta Bogosyan (USA)
Savvas G. Vassiliadis (Greece)
Suwarno (Indonesia)
Tahir M. Lazimov (Azerbaijan)
Tulay Adali (USA)
Vitalijus Volkovas (Lithuania)
Veselina Nedeva (Bulgaria)
YangQuan Chen (USA)
Youcef Soufi (Algeria)

Aim & Scope

The journal publishes original papers in the extensive field of Electrical-Electronics and Computer engineering. It accepts contributions which are fundamental for the development of electrical engineering, computer engineering and its applications, including overlaps to physics. Manuscripts on both theoretical and experimental work are welcome. Review articles and letters to the editors are also included.

Application areas include (but are not limited to): Electrical & Electronics Engineering, Computer Engineering, Software Engineering, Biomedical Engineering, Electrical Power Engineering, Control Engineering, Signal and Image Processing, Communications & Networking, Sensors, Actuators, Remote Sensing, Consumer Electronics, Fiber-Optics, Radar and Sonar Systems, Artificial Intelligence and its applications, Expert Systems, Medical Imaging, Biomedical Analysis and its applications, Computer Vision, Pattern Recognition, Robotics, Industrial Automation.

BAJECE

Balkan Journal of Electrical & Computer Engineering

An International Peer Reviewed, Indexed and Open Access Journal

© BAJECE

ISSN: 2147- 284X
Vol: 3
No : 3
Year: December 2015

CONTENTS

Y. Calleecharan; Spectral analysis and second-order cyclostationary analysis of the non-stationary stochastic motion of a boring bar on a lathe, ...**103-114**

Metia and S. Ghosh; Fuzzy based DG allocation for Loss Minimization in a Radial Distribution System,.....**115-123**

Y. Calleecharan, J.O. Aidanpää, and J.R. Brauer; No-load electromagnetic simulations of a hydropower generator considering the effect of rotor whirling,.....**124-134**

N. Vasilev and A. Bosakova-Ardenska; A New Sorting Algorithm with filling to the left and right,.....**135-141**

C. Bakir; Classification of ECG Signals By the Neighborhood Feature Extraction Meth,.....**142-145**

E. Hamiti, T. Berisha and F. Peci; In-Home PLC Coexistence with Wi-Fi and Ethernet access Networks,.....**146-153**

K. Lenin, B.R. Reddy, and M.S. Kalavathi; Blending of Genetic Algorithm with Fletcher Reeves Method to Solve Reactive Power Problem,.....**154-157**

N. Ben Si Ali and N. Benalia; Design of a MRAS, Speed and Flux Estimators used in Sensorless Control of Induction Motors,.....**158-163**

S. Lishev, R. Popov, and A. Georgiev; Laboratory SCADA Systems – the State of Art and the Challenges,**164-170**

BALKAN JOURNAL OF ELECTRICAL & COMPUTER ENGINEERING

(An International Peer Reviewed, Indexed and Open Access Journal)

Contact

Istanbul Technical University
Department of Electrical Engineering
Ayazaga Campus, Maslak, Istanbul-Turkey

Web: <https://www.bajece.com>
<http://dergipark.ulakbim.gov.tr/bajece/>

e-mail: editor@bajece.com
bajece.editor@gmail.com

Spectral analysis and second-order cyclostationary analysis of the non-stationary stochastic motion of a boring bar on a lathe

Y. Calleecharan

Abstract—In turning and boring, vibration is a frequent problem. The motion of a boring bar is frequently influenced by force modulation, i.e. the dynamic motion of the workpiece related to the residual rotor mass imbalance influences the motion of the boring bar via the relative dynamic motion between the cutting tool and the workpiece. Second-order cyclostationary analysis of the non-stationary stochastic motion of a boring on a lathe is carried out and compared with the conventional spectrum estimation method of the power spectral density. It is observed that the periodic nature of this dynamic motion suits well in the cyclostationary framework because of the rotating motion on the lathe. Also, it is found that cyclostationary analysis contains the time information in the metal cutting process and it can provide insight on the modulation structure of the frequencies involved in the boring operation.

Index Terms—boring bar, cyclostationary, lathe, power spectral density, second-order statistics

NOMENCLATURE

α	cyclic frequency [Hz]
ε_r	normalised random error
τ	continuous time lag parameter [s]
a	cutting depth [mm]
CAF	cyclic autocorrelation function
CDD	cutting depth direction
CSD	cutting speed direction
DCS	degree of cyclostationarity
f	spectral frequency [Hz]
F_s	sampling frequency [Hz]
i	integer index
I	power spectral density estimate
L	data length
m	discrete time index
n	discrete time index
N	positive integer number
PSD	power spectral density
\hat{r}	CAF or autocorrelation estimate
SCDF	spectral correlation density function
s	primary feed rate [mm/rev]
\hat{S}	SCDF estimate
t	continuous time parameter [s]
T	continuous domain time period [s]
U	window-dependent bandwidth normalisation factor
v	cutting speed [m/min]
w	time window

subscripts & superscripts

k	integer index
p	integer index
s	sampling

Y. Calleecharan is with the Department of Mechanical and Production Engineering, University of Mauritius, Réduit, 80837, Mauritius (email: y.callecharan@uom.ac.mu).

I. INTRODUCTION

THE presence of vibrations in the turning and boring operations in a lathe is a very common problem and leads to well-known undesirable effects such as degradation in the surface finish of the machined part, structural fatigue of the cutting tool and holder, and annoyingly high sound levels. Poor choices of cutting parameters, cutting of very hard materials, etc., typically lead to vibration problems. Tool chatter is an issue that has been studied in literature for a long time [1]. With the increasing demands of higher productivity coupled by the requirements for smaller tolerances in the machined part surfaces, the need arises to understand the dynamics in the cutting operation. Pioneering works in this field [2], [3] have been carried out in which the nature, causes and implications of the vibrations were unveiled and traditional spectral analysis techniques were used.

The dynamic motion of the boring bar in the metal cutting process originates from the deformation operation of the work material. This motion of a boring bar is frequently influenced by e.g. force modulation, i.e. the dynamic motion of the workpiece related to residual rotor mass imbalance influences the motion of the boring bar via the relative dynamic motion between the cutting tool and the workpiece. Now, if boring bar vibration is affected by force modulation, the vibration responses generally have non-stationary stochastic properties. However, there are strong indications due to the periodicity involved from the rotary motion on the lathe that the second-order statistic properties of the boring bar vibration have cyclostationary properties.

A number of experimental and analytical studies have been carried out on the study of tool vibration in turning. Most research has been carried out on the dynamic modelling of cutting dynamics [4]–[13] and usually concentrates on the prediction of stability limits as well as experimental methods for the estimation of model parameters related to the structural dynamic properties of the machine tool, the workpiece material, etc. A subset of the research on cutting dynamics has focussed on boring dynamics [14]–[19], which is more relevant to the present work. However, there are relatively few works which address the identification of dynamic properties of machine tool vibration [20]–[25] and especially the identification of dynamic properties of boring bar vibration [23]–[25]. In-depth literature surveys concerning the experimental and analytical studies are given in References [24], [25].

Vibration signals are usually investigated using signal processing tools. Usually, quantities such as variance, autocorrelation, power spectral density (PSD) and power spectrum are estimated for a vibration signal. Traditional time averaging or synchronous averaging are generally included in the estimation methods defined for the quantities mentioned previously. Care should be taken nevertheless with these stationary time-frequency methods since they can lead to ambiguous, if not misleading, results in an industrial environment where there is interference caused by random or periodic noise in the vicinity of the frequency bandwidth of interest. Synchronous averaging attenuates information in the vibration signal that is not harmonically related to the rotation. The part of the vibration signal related to the rotation may be investigated by e.g. the power spectrum estimator or by the PSD. More sophisticated and less common tools such as short time Fourier Transform, the pseudo Wigner-Ville Transform or the discrete

wavelet Transform include the time dimension parameter in the time-frequency analysis, but these methods have a severe drawback in that they cannot exploit any information which does not appear in the synchronous average such as periodically correlated random pulses or amplitude modulation of asynchronous signals which is common from rotating machinery [26].

In the case of periodically correlated random pulses or amplitude modulation of asynchronous signals that is common from rotating machinery, the second-order cyclostationary analysis method e.g. with its cyclic spectrum has proved to be useful—it is able to isolate amplitude modulation phenomena by its unique attribute of spectral correlation in the bi-frequency plane [26]. This paper uses both the traditional spectral analysis method namely the PSD and the less common second-order cyclostationary analysis on time vibration signals from the boring bar operation on a lathe to analyse the second-order characteristics of the boring process.

Though cyclostationary analysis was first applied in the field of telecommunications [27], several works [26], [28]–[31] have shown the usefulness of this technique in analysis and in condition monitoring of mechanical engineering equipment where rotating components exist. Cyclostationary analysis enables periodic amplitude modulation phenomena to distinguish themselves from other interfering vibrations or sounds on the shop floor and this allows in the case of amplitude-modulation signals to resolve the various components present in the signal. The usefulness of cyclostationary analysis is that firstly it is a tool that allows periodic phenomena to be distinguished from non-periodic ones as shown in Reference [32] and secondly, different periodic frequencies e.g. from rotating machines produce distinct frequency patterns in the bi-frequency plane from the cyclostationary analysis method [33]. It is the purpose of this article hence to demonstrate that the cyclostationary analysis framework is indeed a very suitable tool to investigate the force modulation phenomenon affecting the motion of the boring bar.

II. EXPERIMENTAL SET-UP

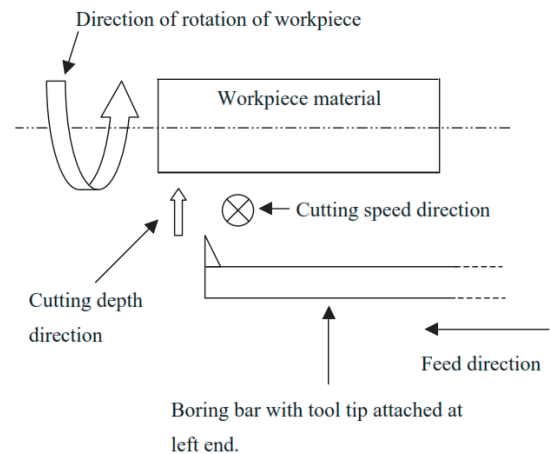
As with all machining operations, metal cutting takes place between a cutting tool and a workpiece material. For a lathe, the cutting tool is most often single-point attached to the tool holder e.g. a boring bar. The desired surface is created by providing suitable relative motion between the cutting tool and the workpiece material. This relative motion is composed of basically two components: primary- and secondary-feed motions. More specifically, the primary motion is generated by rotation of the workpiece material, while the secondary motion is the feed motion associated with the cutting tool. It is the simultaneous combination of these two relative motion components that lead to continuous chip removal from the workpiece material. The cutting operations have been carried out in a Mazak SUPER QUICK TURN—250M CNC turning center shown in Fig. 1 with 18.5 kW spindle power, maximal machining diameter 300 mm and 1007 mm between the centres. In order to save material, the cutting operation was performed as external turning operation, although a boring bar, WIDAX S40T PDUNR15, was used.

A. Measuring equipment and setup

In the vibration measurements, two PCB U353B11 accelerometers and a TEAC RD-200T DAT-recorder were used. The two accelerometers were mounted on the boring bar using threaded studs and they were placed as close as possible to the cutting tool bit—one in the cutting speed direction (CSD) and one in the cutting depth direction (CDD)—see Fig. 2.



Fig. 1. Figure shows the CNC equipment Mazak SUPER QUICK TURN used in the experiments



(a) Schematic plan view of experimental arrangement



(b) Experimental vibration measurement setup

Fig. 2. Top diagram illustrates a schematic plan view of boring bar arrangement with respect to the workpiece material. The cutting speed direction and the cutting depth direction are defined. Bottom diagram shows the two accelerometers mounted on the boring bar in the cutting speed direction and in the cutting depth direction respectively

B. Workpiece materials

Work materials are usually classified according to three production engineering application classes: K (cast irons), M (stainless steels) and P (alloyed steels), all standardised by ISO [34]. In the cutting experiments, three different workpiece materials, each belonging to a different class, have been used, namely: SS 0727-02 or nodular graphite cast iron as a K material, SS 2343-02 or austenitic stainless steel as an M material and SS 2541-03 or chromium molybdenum nickel steel as a P material. These materials have different properties from a production point of view. In American standards, the classes K, M and P correspond to AISI 80-55-06, AISI 316 and AISI 4340 respectively. The machinability or more specifically the cuttability of the materials differs and the chemical composition of the three materials, which is shown in Table I, is also different. The diameter of the workpiece materials is chosen large (around 200 mm); thus the workpiece vibrations may be neglected. Since the statistical properties of the cutting forces are to be investigated, the influence of the workpiece material is vital. The chemical composition and micro-structure of the materials as well as the strength and the thermodynamical properties determine the behaviour of the cutting process. The optimal workpiece material should, from a production engineering point of view, induce small cutting forces, be capable of producing a proper surface finish, have a fair chip breaking property, and not deteriorate the cutting tool. The selected materials have different properties with respect to these four aspects [21].

TABLE I
Chemical composition of workpiece materials

Production engineering application class	C [%]	Si [%]	Mn [%]	Cr [%]	Ni [%]	Mo [%]
K	3.7	2.2	0.4	Nil	Nil	Nil
M	0.05	Nil	Nil	18	12	2.7
P	0.36	0.27	0.62	1.53	1.41	0.17

C. Choice of cutting parameters

In the cutting experiments, standard 55° diagonal inserts have been used. They have tool geometry with the ISO code DNMG 150608-SL with chip breaker geometry for medium roughing. Different carbide grades but with the same geometries have been used for different materials. Carbide grade TN7015 was used for the cast iron and the alloyed steel materials, and carbide grade TN8025 was used for the stainless steel material.

The selection of the cutting data parameter space must be based on thorough knowledge of the cutting process itself. Excessive wear, catastrophic failure or plastic deformation may result if too high cutting speeds or feed rates are selected. This can in turn lead to results which are not characteristic to a turning operation under normal circumstances. The cutting data were chosen according to Table II. Also, no cutting fluid was applied during machining. The aim was to find a parameter space equal for all materials. However, it was found to be impossible to exceed 200 m/min in cutting speed for the stainless steel SS 2343-02.

III. SPECTRAL ANALYSIS

A. Theoretical development of cyclostationary analysis

A couple of definitions for a cyclostationary signal has been put forward [27]. Of relevance in this work is cyclostationarity of order 2, in which case then we are dealing with a quadratic transformation of the time signal. More specifically, a quadratic transformation of the type involving the product of a signal with a delayed version of itself, i.e. the autocorrelation function, will generate spectral lines. Thus, it

TABLE II
Cutting parameter space for the three materials used in the experiments

Material	Parameter	Range
SS 0727-02	Feed, s [mm/rev]	0.1–0.3, step 0.1
	Depth of cut, a [mm]	2
	Cutting speed [m/min]	50–300, step 25
SS 2343-02	Feed, s [mm/rev]	0.1–0.3, step 0.1
	Depth of cut, a [mm]	2
	Cutting speed [m/min]	50–200, step 25
SS 2541-03	Feed, s [mm/rev]	0.1–0.3, step 0.1
	Depth of cut, a [mm]	2
	Cutting speed [m/min]	50–300, step 25

means that a continuous signal $x(t)$ is cyclostationary of order two with fundamental cyclic frequency (or cycle frequency) α if and only if at least some of its delayed products namely $y(t) = x(t)x^*(t - \tau)$ for some delays τ exhibit a spectral line at this cyclic frequency α . The next important definition is the cyclic autocorrelation function (CAF) of a cyclostationary process which is defined as [27]:

$$r_{xx}^{\alpha k}(t) = \frac{1}{T} \int_{-\frac{T}{2}}^{\frac{T}{2}} r_{xx}\left(t + \frac{t}{2}, t - \frac{t}{2}\right) e^{-j2p\alpha k t} dt \quad (1)$$

The spectral correlation density function (SCDF) or cyclic spectrum is the frequency domain representation of the CAF according to the Wiener-Khinchin relation and is given in continuous time as [27]:

$$S_{xx}^{\alpha k}(f) = \int_{-\infty}^{\infty} r_{xx}^{\alpha k}(t) e^{-j2pft} df \quad (2)$$

The Degree of Cyclostationarity (DCS) is basically a measure of the degree of non-stationarity for a wide-sense cyclostationary process and its value lies between zero and unity. It can be computed either from the CAF or from the SCDF, and using the latter is defined in continuous domain as [35]:

$$DCS^{\alpha} = \frac{\int_{-\infty}^{\infty} |S_{xx}^{\alpha}(f)|^2 df}{\int_{-\infty}^{\infty} |S_{xx}^0(f)|^2 df} \quad (3)$$

B. Procedures for analysis

Preliminary analysis using the cyclostationary analysis with the experimental setup in this paper has been done [36], [37]. Reference [37] looked into the statistical evidence of cyclostationary behaviour of the boring bar vibrations. The analysis however did not investigate the force modulation phenomenon that the boring bar experiences when in operation. The process of machining a workpiece on a lathe is usually time-varying; for example we have variation in cutting speed, feed rate, cutting depth, tool wear, etc. [38]. Thus, the cutting process in the lathe can normally be expected to exhibit a non-stationary character, i.e. a process with time-varying properties. However, assuming that throughout the cutting process the following conditions hold namely: no alteration of cutting data (i.e. cutting speed, feed rate and depth of cut), slow deterioration rate of the tool, and time-invariance of the basic structure of the work material, then the cutting forces can be hypothesised as short time stationary random processes. It is of importance to be able to identify these so-called stationary segments of the data because it enables the usage of the toolbox defined for stationary random processes to analyse the data. Two commonly available tests for stationarity that are used in this work are the reverse arrangement test and the run test [39].

A block size has to be calculated for the stationary tests. In Reference [3], a block size of 2400 samples to filter out the first eigenfrequency of the boring bar of about 600 Hz was identified. This can be explained as follows: With the knowledge of an approximate

value of 600 Hz for the first eigenfrequency (in either CSD or CDD) and a sampling frequency F_s of 48 kHz, it can be readily observed that, choosing a block size of 2400 samples, the number of periods of this 600-Hz-eigenfrequency is 30 (in this 2400 samples). This value of 30 averages was considered sufficient to average out the eigenfrequency effect and it is important to note that in order not to interfere with any other phenomenon (periodic or not) present in the data, it is essential not to use more averages than necessary. This block size of 2400 samples corresponds to an averaging time of 0.05 s. Amplitude-modulated vibration signals emanating from rotating machinery generally involve harmonics of the rotating component. It is obvious that if the spindle rotation frequency is filtered out by some averaging time, then so are its harmonics. A simple and most straightforward method to achieve this is to increase the block size (from the 2400 samples) until we cannot observe any fluctuating trend in the mean square values. The optimum block size, in this respect, to filter out the low spindle rotation frequency of around 6 Hz was found to be 96 000 samples, implying an averaging time of 2 s.

Cyclostationarity (in the wide sense) implies periodic variation in the second-order characteristics, hence in the mean square values also. Now from the previous paragraph, it is clear that using a block size of 96 000 samples filters or smoothes out any periodic fluctuations in the mean square values. Therefore, it is obvious that any stationary segments identified in the time data record will contain cyclostationary components as well. It is useful to note that since the two stationarity tests rest on the normal distribution assumption, the minimum number of observations has been set to a value of 10. Also here, it is useful to point out that the level of significance was set to 0.05 and this irrespective of the number of observations. A Matlab [40] script has been written, the purpose of which is to help identifying stationary segments in the time data records and identifying the longest possible stationary segment so that in the analysis, we are sure to obtain the most reliable spectral estimates, be it with the PSD or with the cyclic spectrum in the cyclostationary analysis.

1) Selection of vibration data for analysis

A suitable approach had to be found to identify data that will most probably be of interest in the cyclostationary analysis. The essential steps in this selection procedure for each of the boring bar vibration data were to:

- 1) Identify the longest stationary segment in the data using the reverse arrangement test and the run test.
- 2) Compute the PSD in a frequency region around the first eigenfrequency of the boring bar (which is around 600 Hz in either CDD or CSD) over this longest stationary segment.
- 3) In the event that the PSD from Step 2 displays sufficient amplitude-modulation phenomenon (in the form of sidebands in the frequency region around the eigenfrequency), then the boring bar vibration data is considered as a potential candidate for cyclostationary analysis.

Having identified potential candidates for analysis, the next step was to compute the DCS function. The DCS function is expected to exhibit sufficient energy at α other than zero at twice the low spindle rotation frequency and also at high frequencies around twice the first eigenfrequency (assuming that these two frequency components are mainly responsible for the vibration of the boring bar). If the DCS does not show these features, the vibration data is discarded. It was not timely possible to investigate each of the boring bar vibration data, but it has been found in general that data with the highest primary feed rate of $s = 0.3$ mm/rev had the desired features. In this respect, data pertaining to this high feed-rate was investigated for various cutting speeds and for the three different workpiece materials mentioned in Table II, and the normalised random error was computed according to Reference [27].

2) Estimation of PSD

The Welch method [41] has been used for the computation of the PSD. The p^{th} periodogram of length N_1 with the use of windows is given by

$$\hat{I}_{xx}^p(f_k) = \frac{T_s}{N_1 U} \left| \sum_{i=0}^{N_1-1} x_p(i) w(i) e^{-j \frac{2\pi k n}{N_1}} \right|^2, \quad 0 \leq p \leq N_2 - 1 \quad (4)$$

where f_k is given by $f_k = \frac{k}{N_1 T_s}$ and

$$U = \frac{1}{N_1} \sum_{n=0}^{N_1-1} (w(n))^2 \quad (5)$$

is the window-dependent resolution bandwidth normalisation factor [42] for PSD estimation. Finally, the Welch estimate, \hat{I}_{xx} , is the average of all the periodograms over all segments N_2 as follows:

$$\hat{I}_{xx}(f_k) = \frac{1}{N_2} \sum_{p=0}^{N_2-1} \hat{I}_{xx}^p(f_k) \quad (6)$$

3) Estimation of SCDF in discrete time

The estimation method that has been adopted is the cyclic correlogram method [43]. Its formulation involves estimation of the CAF, $\hat{r}_{xx}(\alpha, m)$, and then of the SCDF, $\hat{S}_{xx}(\alpha, f)$, as shown in Fig. 3 and the estimators are provided in Equation (7).

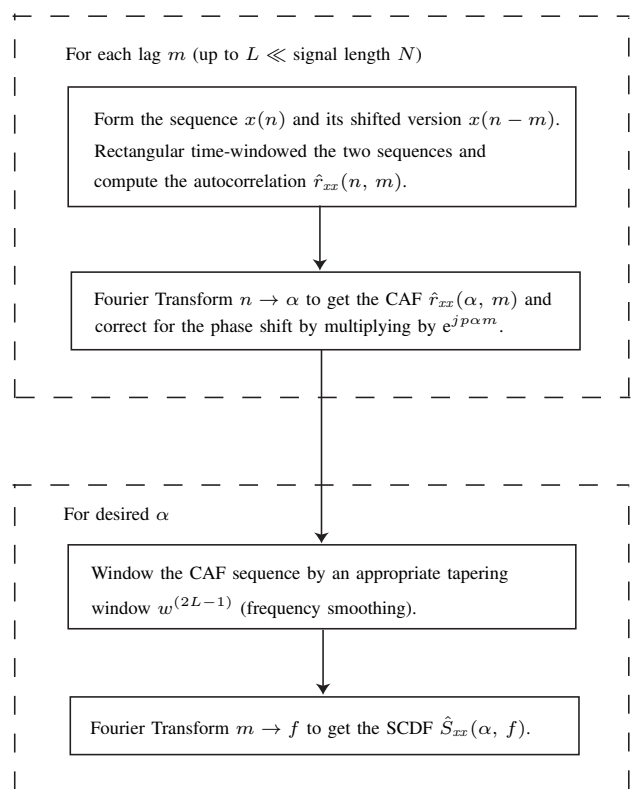


Fig. 3. Schematic representation of the estimation of the SCDF via the cyclic correlogram method. See also Equation (7)

The discrete time estimators for the CAF, $\hat{r}_{xx}(\alpha, m)$, and for the SCDF, $\hat{S}_{xx}(\alpha, f)$, [43] are given next in Equation (7):

$$\hat{r}_{xx}(\alpha_k, m) = \frac{1}{N} \sum_{n=0}^{N-1} x(n) x^*(n - m) e^{-j 2 p \alpha_k n} e^{j p \alpha_k m} \quad (7a)$$

$$\hat{S}_{xx}(\alpha_k, f_k) = \frac{1}{N} \sum_{m=-L}^L w^{(2L-1)}(m) \left[x(n)x^*(n-m)e^{-j2p\alpha_k n} e^{jp\alpha_k m} \right] e^{-\frac{j2pkm}{2L+1}} \quad (7b)$$

with the cyclic frequency $\alpha_k = k \frac{1}{T_s}$, $k = 0, \pm 1, \pm 2, \dots$ and $\frac{1}{T_s}$ is the fundamental frequency. It is readily apparent that when $\alpha_k = 0$, Equation (7a) reduces to the conventional autocorrelation function. Also, then a generally non-stationary process is said to exhibit cyclostationarity in the wide sense only if there exists correlation between some frequency-shifted versions of the process as opposed to a stationary process which exhibits no correlation between any frequency-shifted versions of the process.

In the computation of the CAF, a rectangular window was applied to the time shifted sequences. Similarly, in the computation of the SCDF (see Equation (7b)), a suitable window needs to be applied prior taking the Fourier Transform with respect to m . A symmetric window with tapering ends and having unity magnitude at $m = 0$ has the advantage of de-emphasising the unreliable parts of the CAF, thus reducing the variance in the computation of the SCDF. Thus in Equation (7b), the window w , with support $[-L, L]$ and of length $2L - 1$, is applied to the CAF sequence which has been calculated using Equation (7a) for both positive and negative lags k . The negative CAF values are obtained from the positive counterparts by exploiting the symmetry property of the CAF.

The PSD and SCDF estimation parameters are presented in Tables III and IV respectively. Of importance is to note that one optimisation made on the SCDF estimation code was to downsample the data and hence the sampling frequency F_s (from 48 kHz to 3 kHz). The resulting theoretical useful frequency range up to 1.5 kHz still encompasses the frequency region of interest in both axes of the SCDF bi-frequency plane. Statistical measures of the PSD and the SCDF are given in Tables III and V respectively. The normalised random error ε_r is also known as the coefficient of variation and is commonly used in spectral analysis [44]. Window characteristics are assessed using two important criteria, namely the equivalent noise bandwidth, B_e which provides a measure of the bandwidth of the window in the frequency domain [45] and the statistical bandwidth, B_s , which is also a measure of window bandwidth [44]. In Table V, the following relationship holds [27]:

$$\varepsilon_r \simeq \sqrt{\frac{B_e}{B_s}} \quad (8)$$

TABLE III
Parameters for PSD estimation

Parameter	Value
Data length (samples)	Longest stationary segment
Sampling frequency F_s [kHz]	48
Periodogram's length (samples)	65 536
Time window	Hanning
Overlapping [%]	50
Normalised random error, ε_r	0.1072–0.1387

TABLE IV
Parameters for SCDF estimation

Parameter	a -direction	f -direction
Original data length (samples)	819 200	32 768
Downsampled data length (samples)	51 200	2048
Window	Rectangular	Bartlett

TABLE V
Statistical measures of the SCDF

Parameter	Value
Equivalent noise bandwidth, B_e	0.0781
Statistical bandwidth, B_s	2.1973
Normalised random error, ε_r	0.1886

IV. RESULTS

Many of the data analysed had common features and the objective here is to give representative results either in CDD or in CSD. The parameters for the spectral analyses are based on Tables III to V in Section III-B3. The analysis results are presented in the following order: PSD estimates in the high frequency region (around the first eigenfrequency of the boring bar) and in the low frequency region (encompassing the spindle rotation frequency), and the SCDF contour plots at low cyclic frequencies but at high (spectral) frequencies and at high cyclic frequencies but at low (spectral) frequencies. Accompanying these SCDF contour plots are the DCS functions which facilitate the observation of the spectral correlation features. The results that follow next are for the three materials listed in Table II. Of importance is to note that the SCDF estimates were scaled for the random component and the corresponding SCDF contour plots in Matlab [40] had a level of detail set at 150. Also there were no significant differences between results in the cutting depth direction and in the cutting speed direction.

A. Workpiece material SS 0727-02

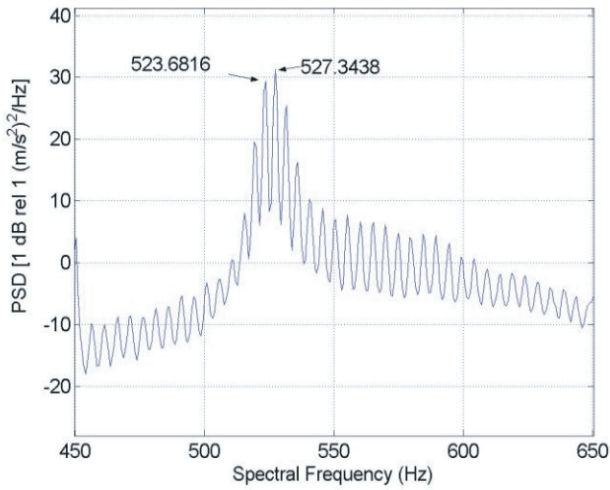
This section presents the results for material SS 0727-02. For the vibration data in CDD with $v = 175$ m/min and $s = 0.3$ mm/rev, Fig. 4 shows respectively the PSD estimate of the data in the high frequency and in the low frequency regions, and the SCDF contour plots are given in Fig. 5 for the low cyclic frequency region around twice the spindle rotation frequency and for the high cyclic frequency region at around twice the first eigenfrequency respectively. Figures 6 and 7 show the corresponding results for the vibration data in CDD with $v = 225$ m/min and $s = 0.3$ mm/rev.

B. Workpiece material SS 2343-02

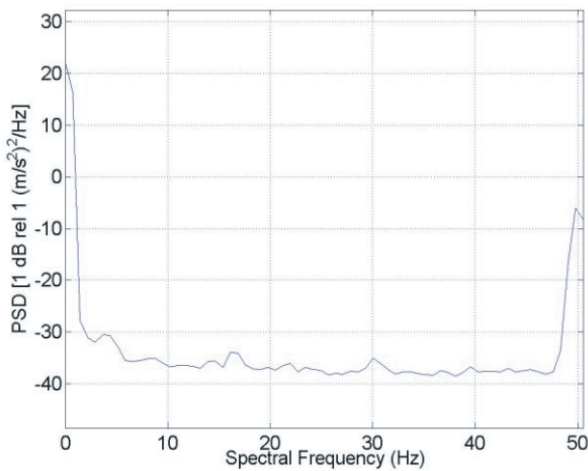
This section presents the results for material SS 2343-02 for vibration data in CSD with $v = 150$ m/min and $s = 0.3$ mm/rev. Figure 8 shows respectively the PSD estimate of the data in the high frequency and in the low frequency regions. The SCDF contour plots are given in Fig. 9 for the low cyclic frequency region around twice the spindle rotation frequency and for the high cyclic frequency region at around twice the first eigenfrequency respectively.

C. Workpiece material SS 2541-03

This section presents the results for material SS 2541-03 for vibration data in CDD with $v = 225$ m/min and $s = 0.3$ mm/rev. Figure 10 shows respectively the PSD estimate of the data in the high frequency and in the low frequency regions. The SCDF contour plots are given in Fig. 11 for the low cyclic frequency region around twice the spindle rotation frequency and for the high cyclic frequency region at around twice the first eigenfrequency respectively.

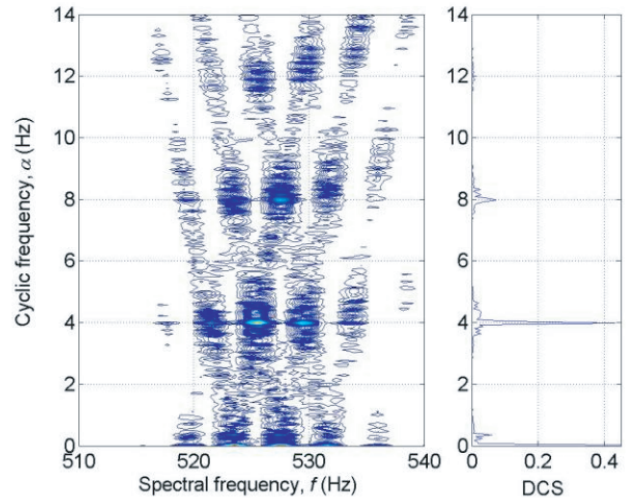


(a) PSD estimate in high frequency region

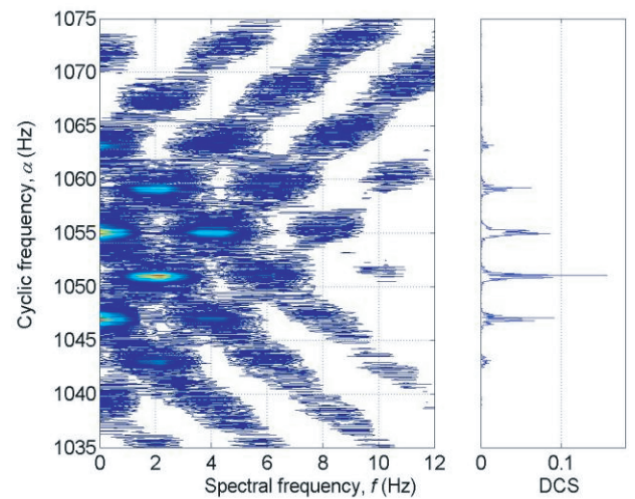


(b) PSD estimate in low frequency region

Fig. 4. PSD estimates in the high frequency region (top figure) and low frequency region (bottom figure) of the dynamic response of the boring bar in the cutting depth direction during a continuous cutting operation in material SS 0727-02, feed rate $s = 0.3$ mm/rev, cutting depth $a = 2$ mm, cutting speed $v = 175$ m/min, tool DNMG 150608-SL and grade TN7015. The number of periodogram averages was 87. The separation of the peaks is approximately 3.66 Hz in the top figure

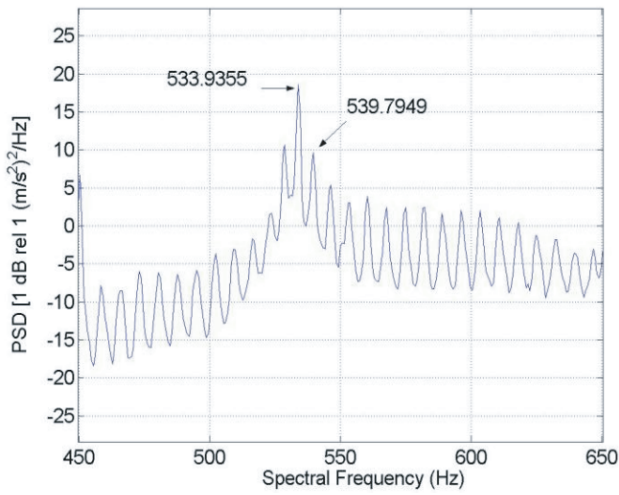


(a) PSD estimate in high frequency region

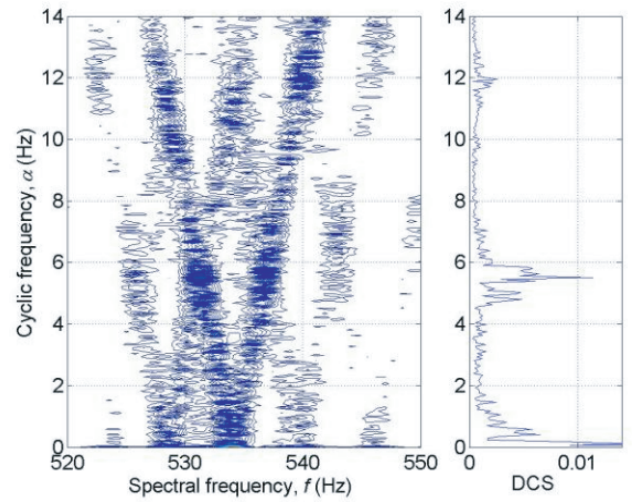


(b) PSD estimate in low frequency region

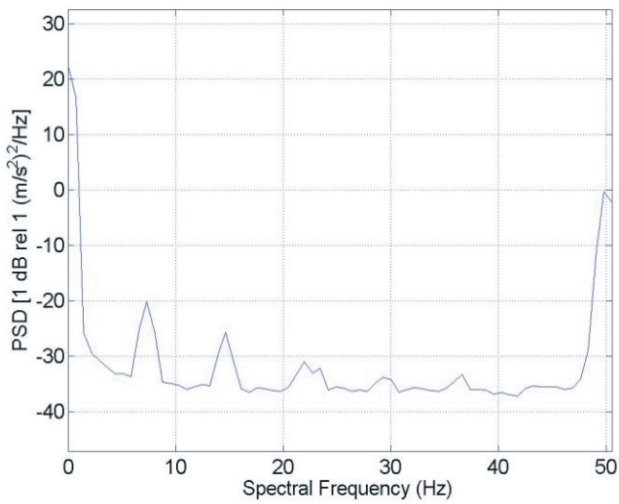
Fig. 5. The SCDF contour plots alongside with DCS functions of the dynamic response of the boring bar in the cutting depth direction during a continuous cutting operation in SS 0727-02, feed rate $s = 0.3$ mm/rev, cutting depth $a = 2$ mm, cutting speed $v = 175$ m/min, tool DNMG 150608-SL and grade TN7015. Top figure: low cyclic frequencies and high spectral frequencies; observe the two peaks in the DCS function at $\alpha = 3.9844$ Hz and 7.9688 Hz. Bottom figure: high cyclic frequencies and low spectral frequencies; observe the main peak in the DCS function at $\alpha = 1051.05$ Hz (around twice the 600 Hz eigenfrequency value)



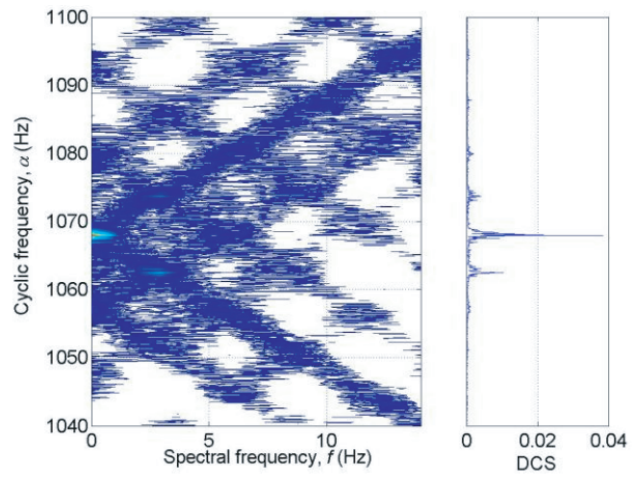
(a) PSD estimate in high frequency region



(a) PSD estimate in high frequency region



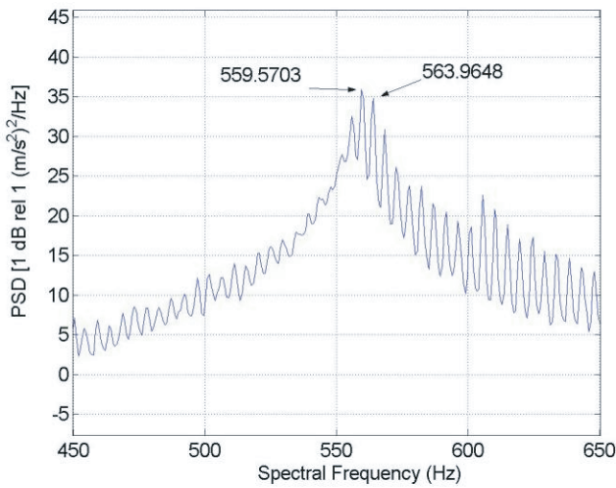
(b) PSD estimate in low frequency region



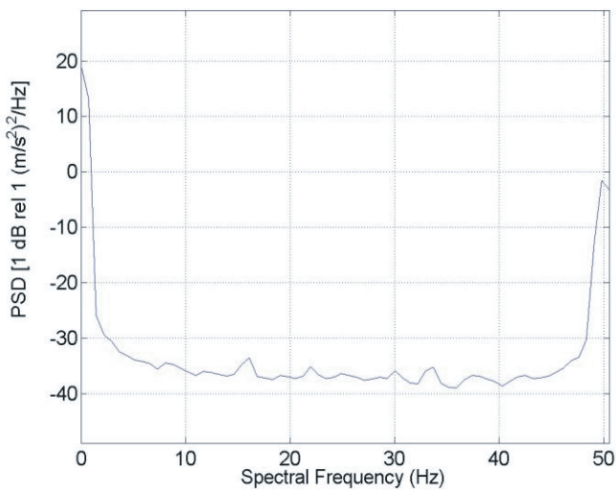
(b) PSD estimate in low frequency region

Fig. 6. PSD estimates in the high frequency region (top figure) and low frequency region (bottom figure) of the dynamic response of the boring bar in the cutting depth direction during a continuous cutting operation in material SS 0727-02, feed rate $s = 0.3$ mm/rev, cutting depth $a = 2$ mm, cutting speed $v = 225$ m/min, tool DNMG 150608-SL and grade TN7015. The number of periodogram averages was 75. The separation of the peaks is approximately 5.86 Hz in the top figure

Fig. 7. The SCDF contour plots alongside with DCS functions of the dynamic response of the boring bar in the cutting depth direction during a continuous cutting operation in SS 0727-02, feed rate $s = 0.3$ mm/rev, cutting depth $a = 2$ mm, cutting speed $v = 225$ m/min, tool DNMG 150608-SL and grade TN7015. Top figure: low cyclic frequencies and high spectral frequencies; observe the main peak in the DCS function at $\alpha = 5.5078$ Hz. Bottom figure: high cyclic frequencies and low spectral frequencies; observe the main peak in the DCS function at $\alpha = 1067.99$ Hz (around twice the 600 Hz eigenfrequency value)

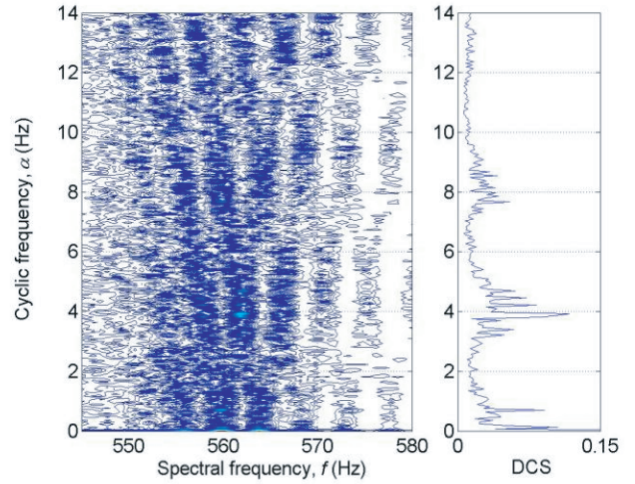


(a) PSD estimate in high frequency region

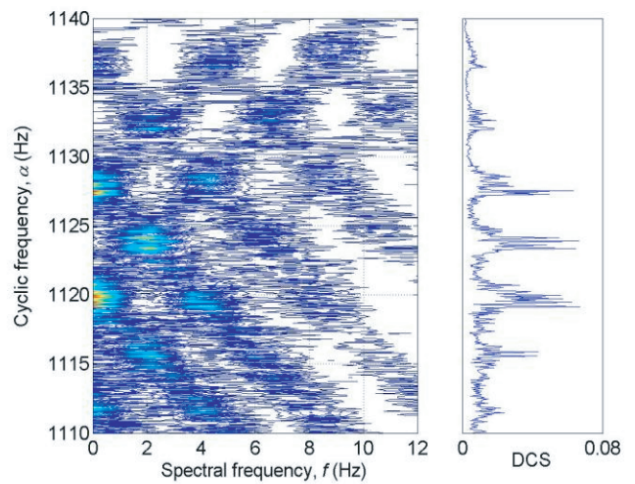


(b) PSD estimate in low frequency region

Fig. 8. PSD estimates in the high frequency region (top figure) and low frequency region (bottom figure) of the dynamic response of the boring bar in the cutting speed direction during a continuous cutting operation in material SS 2343-02, feed rate $s = 0.3$ mm/rev, cutting depth $a = 2$ mm, cutting speed $v = 150$ m/min, tool DNMG 150608-SL and grade TN8025. The number of periodogram averages was 87. The separation of the peaks is approximately 4.4 Hz in the top figure

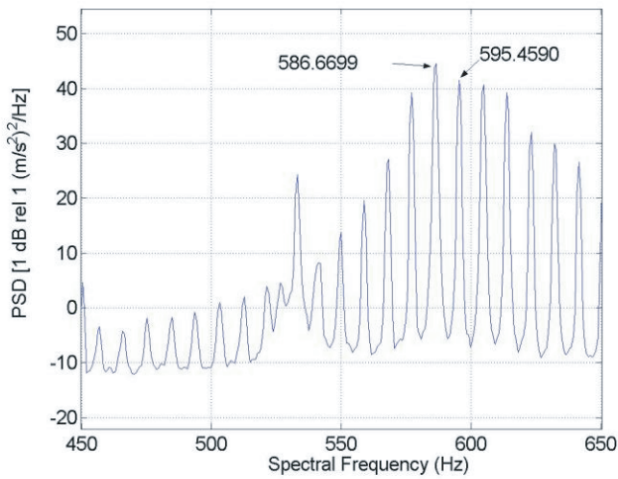


(a) PSD estimate in high frequency region

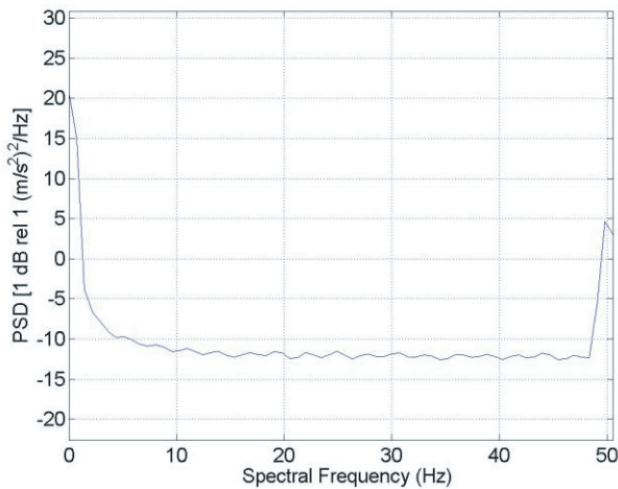


(b) PSD estimate in low frequency region

Fig. 9. The SCDF contour plots alongside with DCS functions of the dynamic response of the boring bar in the cutting speed direction during a continuous cutting operation in SS 2343-02, feed rate $s = 0.3$ mm/rev, cutting depth $a = 2$ mm, cutting speed $v = 150$ m/min, tool DNMG 150608-SL and grade TN8025. Top figure: low cyclic frequencies and high spectral frequencies; observe the main peak in the DCS function at $\alpha = 3.9258$ Hz. Bottom figure: high cyclic frequencies and low spectral frequencies; observe the three main peaks in the DCS function at $\alpha = 1119.14$ Hz, 1123.89 Hz and 1127.52 Hz (around twice the 600 Hz eigenfrequency value)

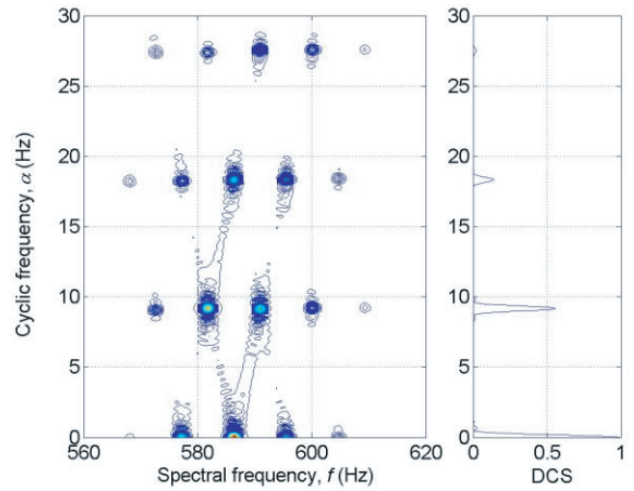


(a) PSD estimate in high frequency region

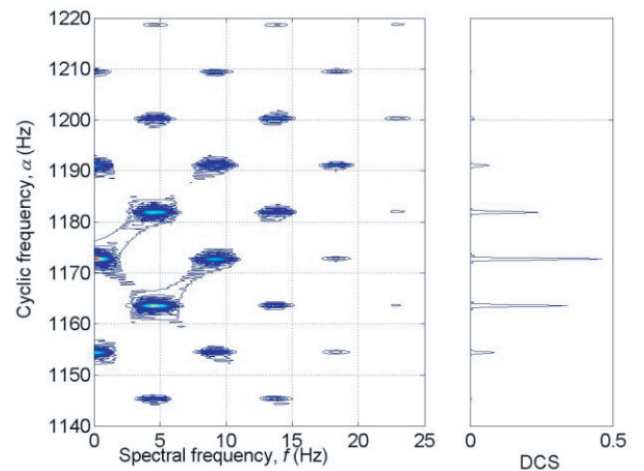


(b) PSD estimate in low frequency region

Fig. 10. PSD estimates in the high frequency region (top figure) and low frequency region (bottom figure) of the dynamic response of the boring bar in the cutting depth direction during a continuous cutting operation in material SS 2541-03, feed rate $s = 0.3$ mm/rev, cutting depth $a = 2$ mm, cutting speed $v = 225$ m/min, tool DNMG 150608-SL and grade TN7015. The number of periodogram averages was 87. The separation of the peaks is approximately 8.79 Hz in the top figure



(a) PSD estimate in high frequency region



(b) PSD estimate in low frequency region

Fig. 11. The SCDF contour plots alongside with DCS functions of the dynamic response of the boring bar in the cutting depth direction during a continuous cutting operation in SS 2541-03, feed rate $s = 0.3$ mm/rev, cutting depth $a = 2$ mm, cutting speed $v = 225$ m/min, tool DNMG 150608-SL and grade TN7015. Top figure: low cyclic frequencies and high spectral frequencies; observe the main peak in the DCS function at $\alpha = 9.1992$ Hz. Bottom figure: high cyclic frequencies and low spectral frequencies; observe the three main peaks in the DCS function at $\alpha = 1163.61$ Hz, $\alpha = 1172.70$ Hz and 1181.89 Hz respectively (around twice the 600 Hz eigenfrequency value)

V. DISCUSSIONS AND ANALYSES

In the PSD estimates of the boring bar vibration data, there seems to be a correlation between the adjacent sideband distance and the workpiece rotation frequency. This might suggest that workpiece motion at the rotation frequency amplitude modulates the response of the boring bar at its first eigenfrequency.

Two types of amplitude modulation phenomena are principally observed in the data for the three materials considered in the analysis. One type is observed for the material SS 0727-02 in Figs 4 and 5, and for the material SS 2343-02 in Figs 8 and 9. If amplitude modulation is assumed, this modulation might for instance explain the cyclic spectrum in Fig. 5 at the cyclic frequency of $\alpha = 3.9844$ Hz. If it is assumed that we have the eigenfrequency in the cutting depth direction at $\frac{1051.05}{2} \simeq 525.525$ Hz, then this may be described by the following amplitude modulation model:

$$x(n) = \left[1 + \sin\left(2\pi \frac{1051.05}{2} n\right) \right] \times \left[\sin\left(2\pi \frac{3.9844}{2} n\right) + \sin\left(2\pi \times 3 \times \frac{3.9844}{2} n\right) + \dots \right] \quad (9)$$

where $x(n)$ is the vibration signal. This model suggests an amplitude modulation of half the spindle rotation frequency.

The second type of amplitude modulation is observed for the material SS 0727-02 in Figs 6 and 7, and for material SS 2541-03 in Figs 10 and 11. Considering for instance Fig. 7 where the eigenfrequency in the cutting depth direction is $1067.99/2$ Hz and the fundamental cyclic frequency is 5.5078 Hz, the modulation pattern can be assumed to be of the form

$$x(n) = \left[1 + \sin(2\pi 5.5078 n) + \sin(2\pi \times 2 \times 5.5078 n) + \dots \right] \times \left[\sin\left(2\pi \frac{1067.99}{2} n\right) \right] \quad (10)$$

where $x(n)$ is the vibration signal. Here on the other hand, an amplitude modulation with the actual spindle rotation frequency is indicated. It is to be noted that in both Equations 9 and 10 element-wise multiplication is implied at the discrete time index n .

Next, variations in the peaks at the fundamental cyclic frequency are observed in the DCS functions accompanying the SCDF contour plots for the materials SS-0727-02 and SS 2343-02 (both with $s = 0.3$ mm/rev). This can be observed e.g. in Fig. 9. This variation implies a change in the cutting speed v occurring in the metal cutting process. This variation in frequency is known as frequency modulation. Furthermore, this results in spreading of energy to the surrounding peaks in the DCS function. On the other hand, this frequency modulation effect was observed to be much less severe for the material SS 2541-03. Besides it was found for this material that these frequency variations tend to disappear with higher cutting speeds. This is seen in Fig. 11 where one can observe that the peaks in the DCS function are well-defined. This cannot be explained by the resistance of the workpiece materials during the cutting process since material SS 0727-02 is cast iron whereas materials SS 2343-02 and SS 2541-03 are steel-based. Examining the contour SCDF plots alongside with the DCS functions allows one to resolve the type of amplitude modulation pattern present and this information is not readily available from a PSD estimate.

Furthermore, for a given amplitude modulation type, the size of the rhombic spectral correlation patterns of the SCDF plots in the bi-frequency SCDF plane is dictated by their cyclic frequencies,

the first eigenfrequency in CSD or CDD and possibly the cutting speed v . The low frequency modulating component appears to be the spindle rotation frequency. It is to be expected that the cyclic frequency is twice the spindle rotation frequency (considering the relationship of the cyclic frequency α to the spectral frequency f). Indeed, Reference [46] in the application of cyclostationary analysis to study bearings showed that this low modulating cyclic frequency can be in fact related to the rotation frequency of the bearing or to some bearing's fault such as an inner race fault, or to both of them. In this work, it is thus expected that the low cyclic frequency components observed in all of the vibration data has some direct relationship to the spindle rotation frequency.

Hence, after having found that second-order cyclostationary analysis can identify the modulation phenomenon present in the vibration data, a next crucial step is to identify the nature of the cyclic frequency components. To that end, the rotation speed was calculated (based on the workpiece diameter and the cutting speed) and compared to the cyclic frequency for each data. The workpiece diameter considered here is the diameter at the start of the cutting process. Table VI shows this comparison.

TABLE VI. Comparison of spindle rotation frequency with cyclic frequency

Vibration data ¹	Starting workpiece diameter [m]	Rotation frequency based on Column 2 [Hz]	Observed α in Section IV [Hz]	% magnitude difference between Columns 3 and 4 based on Column 4
Workpiece material SS 0727-02 (with $s = 0.3$ mm/rev)				
CDD—175	0.2000	4.6420	3.9844	16.50
CDD—225	0.1750	6.8209	5.5078	23.84
CSD—275	0.1900	7.6785	6.2695	22.47
Workpiece material SS 2343-02 (with $s = 0.3$ mm/rev)				
CDD—75	0.1662	2.3940	3.0469	21.43
CSD—150	0.1793	4.4382	3.9258	13.08
Workpiece material SS 2541-03 (with $s = 0.3$ mm/rev)				
CDD—225	0.1380	8.6497	9.1992	5.97

¹ The numerical value after CDD or CSD refers to the cutting speed v m/min

It can be seen from Table VI that there is a relatively small difference for the material SS 2541-03 (with $s = 0.3$ mm/rev). Although not shown here, the author has been able to find that this difference was in fact lower than 15 % for the other seven cutting data (three in the CDD and four in the CSD) for this material. The discrepancies are more severe for the materials SS 2343-02 and SS 0727-02. The diameters of the workpiece materials were measured by the CNC coordinate system in the lathe. Now, for each new insert the position of the tool tip is not calibrated so that in effect, it can be said that the coordinate system only provides us with an approximate value of the diameter of the workpiece. This leads to the conclusion that the spindle rotation frequencies calculated in Column 3 of Table VI represent in fact approximations to the true spindle rotation frequencies. It is also important here to take into account the frequency modulation effect observed in the data for the steel-based material SS 2343-02 and cast iron material SS 0727-02.

The true spindle rotation frequencies are in most cases observable from the PSD estimates at the lower frequencies. Based on the preceding discussions, it can be put forward that the spindle rotation frequency is in fact the cyclic frequency as observed in the SCDF plots. This leads us to think of some other phenomenon affecting the cutting process. In fact, in rotating machinery, it is not

uncommon to observe that looseness in some fixtures manifests itself by a sideband at half the rotation frequency of the main rotating component [47]. The fact that the cutting speed varies during cutting and that the SCDF plots suggest either an amplitude modulation of the eigenfrequency with half the workpiece rotation frequency or with the actual workpiece rotation frequency leads to the conclusion that the structure of the boring bar vibration is more complex than the hypothesised simple amplitude modulation structure.

VI. CONCLUSIONS

The objective of this work is to investigate the force modulation phenomenon associated with the dynamic motion of the boring bar in the metal cutting process on a lathe. In Reference [3] it has been shown that the effect of the material deformation process is to induce vibration in the boring bar at the first eigenfrequency in either CDD or CSD. Unbalance in the workpiece rotation was also known to affect the vibrations of the boring bar. The stochastic nature of the cutting process is exposed by the PSD analysis, but the latter is limited in analysis by its time-invariance property.

As seen in Sections IV and V, the PSD analysis has proved to be not quite effective in revealing whether there is modulation phenomenon occurring in the vibration data nor the exact form in case of occurrence of amplitude modulation. In the second-order cyclostationary analysis, the DCS function serves as preliminary tool to unveil the presence of modulation in the vibration data. Also, in-depth analysis with the SCDF bi-frequency contour plots could, in every case considered, provide concise and unambiguous information regarding the amplitude modulation phenomenon occurring. The DCS function could be computed separately before computing the SCDF which is more computationally expensive.

The results obtained in Section IV indicate that the cyclic spectrum (or SCDF plot) is likely to provide information concerning the frequency of the actual boring bar eigenfrequency from the force-modulated boring bar vibration data. Moreover, the cyclostationary analysis unwrapped new information from the cutting process. Firstly, the cycle frequencies obtained from the analysis may indicate the presence of looseness in the fixture of the boring bar. Secondly, frequency variations in the peaks of the DCS functions were observed for the materials SS 2343-02 (steel-based) and SS 0727-02 (cast iron). This variation in the DCS peaks leads to the phenomenon of frequency modulation, which has not been investigated further in this work. It is known that the cutting speed varies during cutting and this coupled to the fact that the cyclostationary analysis suggests either an amplitude modulation of the eigenfrequency with half the workpiece rotation frequency or with the actual workpiece rotation frequency, shows that the amplitude modulation models put forward in Section V may not be complete.

The manufacturing industry is always putting much effort to reduce the vibration emanating from the metal cutting process on a lathe. Thus, understanding the causes and sources of the vibration causing effect is fundamental. In this work, second-order cyclostationary analysis has revealed some looseness in the boring bar fixture; such information is vital to the vibration control engineers. In essence, cyclostationary analysis at the second order has demonstrated its ability to handle the non-stationary stochastic nature of the metal cutting process on a lathe.

ACKNOWLEDGMENTS

The author wishes to express his sincere thanks to Prof. Lars Håkansson of the Department of Applied Signal Processing, Blekinge Tekniska Högskola (Blekinge Institute of Technology), Sweden, for his assistance.

REFERENCES

- [1] Y. Altintas. *Manufacturing Automation, Metal Cutting Mechanics, Machine Tool Vibrations, and CNC design*. Cambridge University Press, 2000.
- [2] L. Håkansson. *Adaptive Active Control of Machine-Tool Vibration in a Lathe—Analysis and Experiments*. PhD thesis, Department of Production and Materials Engineering, Lund University, Sweden, 1999.
- [3] L. Pettersson. *Vibrations in metal cutting: measurement, analysis and reduction*. Licentiate thesis, Department of Telecommunications and Signal Processing, Blekinge Institute of Technology, Sweden, 2002.
- [4] J. Tlustý. Analysis of the state of research in cutting dynamics. In *Annals of the CIRP*, volume 27/2, pages 583–589. CIRP, 1978.
- [5] D.W. Wu and C.R. Liu. An analytical model of cutting dynamics—Part 1: Model building. *Journal of Engineering for Industry, Transactions of the ASME*, 107(2):107–111, May 1985.
- [6] D.W. Wu and C.R. Liu. An analytical model of cutting dynamics—Part 2: Verification. *Journal of Engineering for Industry, Transactions of the ASME*, 107(2):112–118, May 1985.
- [7] I.E. Minis, E.B. Magrab, and I.O. Pandelidis. Improved methods for the prediction of chatter in turning—Part 1: Determination of structural response parameters. *Journal of Engineering for Industry, Transactions of the ASME*, 112:12–20, February 1990.
- [8] I.E. Minis, E.B. Magrab, and I.O. Pandelidis. Improved methods for the prediction of chatter in turning—Part 2: Determination of cutting process parameters. *Journal of Engineering for Industry, Transactions of the ASME*, 112:21–27, February 1990.
- [9] I.E. Minis, E.B. Magrab, and I.O. Pandelidis. Improved methods for the prediction of chatter in turning—Part 3: A generalized linear theory. *Journal of Engineering for Industry, Transactions of the ASME*, 112:28–35, February 1990.
- [10] S.M. Pandit, T.L. Subramanian, and S.M. Wu. Modeling machine tool chatter by time series. *Journal of Engineering for Industry, Transactions of the ASME*, 97:211–215, February 1975.
- [11] S.M. Pandit, T.L. Subramanian, and S.M. Wu. Stability of random vibrations with special reference to machine tool chatter. *Journal of Engineering for Industry, Transactions of the ASME*, 97:216–219, February 1975.
- [12] T. Kalmár-Nagy, G. Stépán, and F.C. Moon. Subcritical Hopf bifurcation in the delay equation model for machine tool vibrations. *Journal of Nonlinear Dynamics*, 26:121–142, 2001.
- [13] J. Gradišek, E. Govekar, and I. Grabec. Chatter onset in non-regenerative cutting: A numerical study. *Journal of Sound and Vibration*, 242(5):829–838, 2001.
- [14] E.W. Parker. Dynamic stability of a cantilever boring bar with machined flats under regenerative cutting conditions. *Journal of Mechanical Engineering Science*, 12(2):104–115, February 1970.
- [15] G.M. Zhang and S.G. Kapoor. Dynamic modeling and analysis of the boring machining system. *Journal of Engineering for Industry, Transactions of the ASME*, 109(3):219–226, August 1987.
- [16] P.N. Rao, U.R.K. Rao, and J.S. Rao. Towards improved design of boring bars—Part 1: Dynamic cutting force model with continuous system analysis for the boring bar. *International Journal of Machine Tools and Manufacture*, 28(1):33–44, 1988.
- [17] F. Kuster and P.E. Gygax. Cutting dynamics and stability of boring bars. *CIRP Annals—Manufacturing Technology*, 39(1):361–366, 1990.
- [18] S. Jayaram and M. Iyer. An analytical model for prediction of chatter stability in boring. *SME technical paper, (MR00-202)*, Society of Manufacturing Engineers, 28:203–208, 2000.
- [19] I. Lazoglu, F. Atabey, and Y. Altintas. Dynamics of boring processes—Part III: Time domain modeling. *International Journal of Machine Tools & Manufacture*, 42:1567–1576, 2002.
- [20] M.K. Khraisheh, C. Pezeshki, and A.E. Bayoumi. Time series based analysis for primary chatter in metal cutting. *Journal of Sound and Vibration*, 180(1):67–87, 1995.
- [21] P-O. H. Sturesson, L. Håkansson, and I. Claesson. Identification of the statistical properties of the cutting tool vibration in a continuous turning operation—Correlation to structural properties. *Mechanical Systems and Signal Processing*, 11(3):459–489, 1997.
- [22] J. Gradišek, I. Grabec, S. Siebert, and R. Friedrich. Stochastic dynamics of metal cutting: Bifurcation phenomena in turning. *Mechanical Systems and Signal Processing*, 16(5):831–840, 2002.
- [23] E. Marui, S. Ema, and S. Kato. Chatter vibration of lathe tools—Part 1: General characteristics of chatter vibration. *Journal of Engineering for Industry, Transactions of the ASME*, 105(2):100–106, May 1983.
- [24] L. Andrén, L. Håkansson, A. Brandt, and I. Claesson. Identification of dynamic properties of boring bar vibrations in a continuous boring operation. *Mechanical Systems & Signal Processing*, 18(4):869–901, 2004.

- [25] L. Andren, L. Håkansson, A. Brandt, and I. Claesson. Identification of motion of cutting tool vibration in a continuous boring operation—Correlation to structural properties. *Mechanical Systems & Signal Processing*, 18(4):903–927, 2004.
- [26] A. McCormick and A.K. Nandi. Cyclostationarity in rotating machine vibrations. *Mechanical Systems and Signal Processing*, 12(2):225–242, 1998.
- [27] W.A. Gardner. *Statistical Spectral Analysis: A Non-Probabilistic Theory*. Prentice Hall, Englewood Cliffs, New York, 1987.
- [28] C. Capdessus, Sidahmed. M., and J.L. Lacoume. Cyclostationary processes: Application in gear faults early diagnosis. *Mechanical Systems and Signal Processing*, 14(3):371–385, 2000.
- [29] L. Bouillaut and M. Sidahmed. Cyclostationary approach and bilinear approach: comparison, applications to early diagnosis for helicopter gearbox and classification method based on HOCS. *Mechanical Systems and Signal Processing*, 15(5):923–943, 2001.
- [30] R.B. Randall, J. Antoni, and S. Chobsaard. The relationship between spectral correlation and envelope analysis for cyclostationary machine signals, application to ball bearing diagnostics. *Mechanical Systems and System Processing*, 15(5):945–962, 2001.
- [31] J. Antoni, J. Danière, and F. Guillet. Effective vibration analysis of IC engines using cyclostationarity—Part I: A methodology for condition monitoring. *Journal of Sound and Vibration*, 257(5):815–837, 2002.
- [32] M. Knaak and D. Filbert. Acoustical semi-blind source separation for machine monitoring. In *Proc. conference Indep. Compon. Anal. Signal*, pages 361–366, 2001.
- [33] J. Goerlich, D. Bruckner, A. Richter, O. Strama, R.S. Thomä, and U. Trautwein. Signal analysis using spectral correlation measurement. In *IEEE Instrumentation and Measurement Technology Conference, St. Paul, U.S.A*, volume 2, pages 1313–1318, May 18–21 1998.
- [34] Sandvik. General turning. Sandvik AB Coromant, [Online]. http://www2.coromant.sandvik.com/coromant/pdf/Metalworking_Products_061/tech_a_8.pdf.
- [35] W.A. Gardner and G.D. Zivanovic. Degrees of cyclostationarity and their application to signal detection and estimation. *Signal Processing*, 22(3):287–297, 1991.
- [36] Y. Calleecharan. Cyclostationary analysis of boring bar vibration. Master's thesis, Blekinge Institute of Technology, Sweden, ISRN: BTH-IMA-EX-2003/D-01-SE, January 2003.
- [37] A.H. Brandt, L. Håkansson, and I. Claesson. Cyclostationary analysis of boring bar vibrations. In *IMAC-XXII: Conference & Exposition on Structural Dynamics*. Society of Experimental Mechanics, 2004.
- [38] Sandvik. *Modern Metal Cutting: A Practical Handbook*. AB Sandvik Coromant, 1994.
- [39] J.S. Bendat and A.G. Piersol. *Random data: Analysis and Measurement Procedures*. John Wiley & Sons, second edition, 1986.
- [40] Matlab computing software, The MathWorks 2002. Version 6.5 (R13).
- [41] P.D. Welch. The use of Fast Fourier Transform for the estimation of power spectra: A method based on time averaging over short, modified periodograms. *IEEE Transactions on Audio and Electroacoustics*, Au-15(2):70–73, June 1967.
- [42] F. Harris. On the use of windows for harmonic analysis with the discrete Fourier Transform. In *Proc. of the IEEE*, volume 66, pages 51–83, 1978.
- [43] W.A. Gardner. *Cyclostationarity in Communications and Signal Processing*. IEEE Press, New Jersey, 1994.
- [44] J.S. Bendat and A.G. Piersol. *Random Data: Analysis and Measurement Procedures*. John Wiley & Sons, third edition, 2000.
- [45] H. Jokinen, J. Ollila, and O. Aumala. On windowing effects in estimating averaged periodograms of noisy signals. *Measurement*, 28:197–207, 2000.
- [46] I. Antoniadis and G. Glossiotis. Cyclostationary analysis of rolling-element bearing vibration signals. *Journal of Sound and Vibration*, 190(3):419–447, 1996.
- [47] V. Wovk. *Machinery Vibration: Measurement and Analysis*. McGraw-Hill, 1991.

BIOGRAPHY



Yogeshwarsing Calleecharan received the B.Eng. (Hons) degree in Mechanical Engineering from the University of Mauritius, Mauritius, in 2000, the M.Sc. degree in Mechanical Engineering from Blekinge Tekniska Högskola, Sweden, in 2003, and the Ph.D. degree in Solid Mechanics from Luleå Tekniska Universitet, Sweden, in 2013. Since 2014 he is a lecturer with the Mechanical and Production Engineering Department, University of Mauritius, Mauritius. His research interests include solid mechanics, vibration and signal analysis, rotordynamics, signal processing, electromechanics and software development with the Ada programming language.

Fuzzy based DG allocation for Loss Minimization in a Radial Distribution System

A. Metia and S. Ghosh

Abstract—Due to the restructuring in electricity market and environmental concerns penetration level of DG unit has been increased rapidly. It is also playing a significant role in minimization of line losses of a power system network. So it is very important to define the size and location of distributed generation unit to be allocated in a power system network. On the other hand due to radial distribution systems basic inherent features such as radial structure, a wide range of X/R ratios, and a large number of nodes; the optimal sizing and siting problem of a DG unit cannot be determined by the conventional techniques, which are used for transmission systems. A novel method for the estimation as well as minimization of losses in a radial distribution system with DG unit has been presented in this paper. It also improves the voltage profile of the existing power systems and in addition a combined and optimal power factor is also calculated. An algorithm is presented in this paper to obtain the optimum position of DG units in the distribution network based on the available amount of DG using Fuzzy logic. Forward backward sweep method makes the load flow solution faster. Test results on a 33-bus system reveal that the superiority and simplicity of the proposed algorithm.

Keywords— Fuzzy logic, distributed Generation, loss reduction, optimal location, optimal size.

I. INTRODUCTION

THE penetration level of distributed generators is increased due to the restructuring in electric power system. Distributed generators which are used for local power generation in a distribution system are generally connected to the load end directly. These DGs are normally ranged from few kW to few MW and they are not centrally placed. Most of the distribution systems are conventionally planned as passive network and they are capable of unidirectional power flow. However, distribution networks are transferred to active network with bidirectional power flow by installing a DG unit in the distribution system. In spite of the restructuring of electricity market, utilization of DG unit in the distribution system can make many benefits such as voltage profile improvement, real and reactive power loss reduction, environmental concerns, power quality improvement, investment risk reduction, reliability and security improvements [1, 2].

Avik Metia, is with Thapar University, Department of Electrical and Instrumentation Engineering, Patiala, India (e-mail: avik.ee08@gmail.com).

Smarajit Ghosh, is with Thapar University, Department of Electrical and Instrumentation Engineering, Patiala, India (e-mail: smarajite@hotmail.com).

Power loss is varied from one country to another country which can be found from different statistics and studies. Different studies and statistics showed that distribution losses are 70% of the total power losses of the system [3] and 20% of total generated power is transferred into losses in a network [4, 5], and it would make a cost millions of dollar every year. So power loss reduction is one of the important solutions to improve the overall efficiency of a distribution system. To reduce the distribution system losses there are three well known techniques are available; network reconfiguration, optimal capacitor allocation and DG placement. Out of these three techniques DG allocation has both technical as well as economic benefits that have presented in the research paper [7-10].

Recently many studies have been employed to reduce the system losses by optimal sizing and siting of DG. Most of the methods are analytical and some of them are heuristic and metaheuristic methods. In the research paper [11] a reduced gradient approach has been presented to obtain the appropriate size of DG unit. An analytical method based on 2/3 rule as a rule of thumb has been presented in this research paper to obtain optimal placement and optimal size of DG unit [12]. Many analytical approaches [4-8] were utilized for the DG allocation and sizing. Two analytical methods for a fixed size DG allocation are introduced in the research paper [4] out of which first one is applicable for radial system whereas second one is applicable for meshed network. Exact loss formula based analytical method is presented in [18] whereas analytical expressions for multi DG units are developed in the research paper [14]. A loss sensitivity factor based analytical method has been proposed to obtain the optimal size and position of a single DG unit in a distribution system [15]. A probabilistic approach has been developed in [19] for the selection of distributed generator location an hourly load or daily load changes are weighted according to the load magnitude and the location points are also weighted according to their load magnitude. The application of the proposed method demonstrated the efficiency of the method to solve the problem of DG sizing and siting. In [20] a MTLBO algorithm has presented to determine optimal size and optimal location of distributed generators in a distribution system. The optimal positioning and sizing problem was considered as MINLP problem in this paper. Authors in [21] has presented simultaneous allocation of distributed generators and capacitors for reducing active as well as reactive power loss minimization in a radial distribution network using a memetic algorithm which is the combination

of local search and genetic algorithm. A PSO algorithm with constriction factor has been used in [22] to determine the optimal sizes and location of multiple DG units. A predetermined load growth with voltage regulation for five year was considered as constraints in this research paper. The results proved that multiple DG units which are allocated in distribution system can reduce both real and reactive power loss, purchase cost of energy, voltage deviation in the distribution system. A BSOA algorithm has been adopted to assign distributed generator units in a radial distribution network in [23], where the weighting factor is adopted with objective function to minimize real power loss and also to improve the voltage profile. The numerical results described that the proposed method is more effective and efficient in comparisons with the analytical and other heuristics methods. In this paper a backward forward sweep methodology has been used for estimation of losses in a radial distribution system. After the estimation of losses a fuzzy expert system is implemented to standard test system to find the suitable node where the DG unit is to be placed such that the system losses is minimized as well as voltage profile of the system is improved. After getting the suitable node an analytical methodology has been used to compute optimum size of DG unit. It is considered that the DG unit is located in the primary of the distribution system to reduce the losses. The developed methodology is effective and suitable for allocating a single DG unit in the radial system.

The rest of the research paper is developed as follow: section II includes location and sizing problem of DG units. Section III contains modeling and problem formulation. Section IV contains Backward/forward sweep method for load flow and section V includes proposed fuzzy expert system to find optimal location, the analytical approach to obtain optimal size of DG unit is described in the section VI. Optimal results are presented and summarized in section VII. At final section VIII conclusions and remarks are described.

II. ALLOCATION AND SIZING PROBLEM

The optimal allocation and sizing of a DG unit is one of the important factors for loss reduction in a distribution system. *Fig. 1* shows a three dimensional plot between power losses and DG size at each buses in a distribution system. Figure 1 shows that as the DG size is increased for a particular bus the losses of a distribution network are reduced. However the loss is increased if the DG size is increased beyond the optimal DG size at that particular location. So whenever the DG size is increased more than the optimal value, the loss is increased and it may go beyond the loss of the base case loss. It is also important that minimization of losses are directly depends on location of DG.

From the *Fig. 1* it can be concluded that for a particular distribution system it is irrelevant to construct very high capacity DG unit. Allocation of a high capacity DG unit will cause very high system losses. So the size selection process of DG unit is carried out based on the size of distribution system (based on load in MW). The reason for the relation between higher DG unit capacity with higher losses can be explained that the distribution system is designed in such a way that such the power flows initially from sending end to the receiving end.

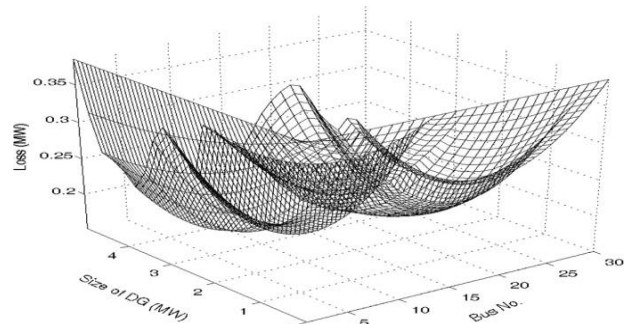


Fig.1. Effect of different DG size and their location on losses [18]

The conductor sizes are generally reduced from sending end towards the receiving end. So without change of network any installation of a large size DG unit will make excessive power flow in small size conductors and as a result it causes higher losses.

The DG placement problem is solved by location issue first then followed by the sizing issue

III. MODELING AND PROBLEM FORMULATION

3.1 Different Load model

In power system loads are modeled into three categories based on the static characteristics of the load. These are as follows.

- **Constant power:** In this load model active power and reactive power are independent of the voltage changes.
- **Constant current:** In this load model bus voltage is directly proportional with the active and reactive power respectively.
- **Constant impedance:** In this load model active power and reactive power are directly proportional to the square of the bus voltage.

In this paper the loads are modeled as constant power model to study the behavior of loads.

3.2 DG model and their types

Based upon different point of view such as; type of connection, types, different operation mode DG unit can be modeled as PV bus or DG unit can also be modeled as PQ bus [24]. A DG unit which is already modeled as PQ bus can also modeled into three other types such as: DG unit has constant P and Q [25], DG unit having a certain specified value of P and power factor (PF) [25]. As a varying Q generator DG unit can also be modeled [25]. A DG unit having specified real power and bus voltage magnitude is modeled as PV bus DG unit [25]. DG units are many times modeled as PV node without considering dummy branch; they can inject reactive power to the distribution system and support the voltage profile [26].

DGs with smaller capacity and in the form of constant PQ model are very much sufficient for the loss minimization of a radial distribution system. DG unit as negative load is assumed in this presented research paper.

Various types of DG technologies used in a distribution system are presented in TABLE I.

TABLE I
DIFFERENT DG TECHNOLOGIES

Types of DG	Real power (P)	Reactive power (Q)	Example
1	+	0	PV arrays, Battery, fuel cells
2	0	+	Capacitor
3	+	+	Diesel engine based Synchronous generators
4	+	-	Induction generators
(+ Produces		(-) Absorbs	

IV. OBJECTIVE FUNCTION AND BACKWARD/FORWARD SWEEP POWER FLOW METHOD

4.1 Objective function

‘Exact loss’ formula [30] can be used for the estimation of total real power losses of a radial distribution system by equation (1).

$$\text{Min } P_L = \sum_{i=1}^N \sum_{j=1}^N [\alpha_{ij}(P_i P_j + Q_i Q_j) + \beta_{ij}(Q_i P_j - P_i Q_j)] \quad (1)$$

Where $\alpha_{ij} = \frac{r_{ij}}{v_i v_j} \cos(\delta_i - \delta_j)$, $\beta_{ij} = \frac{r_{ij}}{v_i v_j} \sin(\delta_i - \delta_j)$
 and $r_{ij} + jx_{ij} = z_{ij}$; is the impedance of ij th matrix.

4.2 Backward/ Forward sweep power flow method

Three phase distribution system is balanced considering this a load-flow solution is carried out, so the three phase system can be represented as a single line diagram. A direct load flow can be used for the radial distribution system [27]. Now considering branch-1 the receiving end node voltage can be calculated as

$$V(2) = V(1) - I(1)Z(1) \quad (2)$$

Similarly for branch 2

$$V(3) = V(2) - I(2)Z(2) \quad (3)$$

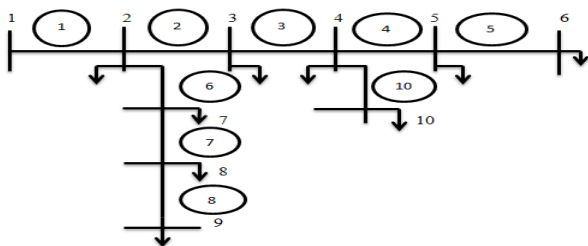


Fig.2. A simple radial distribution system

So as the source node voltage $V(1)$ is already known so if we can determine the branch current $I(1)$ then it will be very easy to compute $V(2)$ from Eq. (2). So in the same way by computing the branch current $I(2)$ we can easily determine the node voltage $V(3)$. Similarly we can determine the node voltages of node 1, 2 ... N_{no} (no. of nodes) in forward sweep.

So based on the above equation the voltage of node ‘i’ can be written as

$$V(i) = V(i - 1) - I(i)Z(i) \quad (4)$$

The load current of node ‘i’; $I_L(i)$ can be calculated as:

$$I_L(i) = \frac{P_L(i) - jQ_L(i)}{V(i)^*}; \quad \text{for } i=1,2,\dots,N_{no} \quad (5)$$

Where $P_L(i)$ = active power of load connected to node ‘i’

$Q_L(i)$ = reactive power of load connected to node ‘i’

Branch current through node ‘i’ i.e. $I(i)$ is the sum of load current $I_L(i)$ of node ‘i’, and the branch currents which are connected to this line can be represented as

$$I(i) = I_L(i) + \sum_{j \in \gamma_i} I(j) \quad (6)$$

Where γ_i is consisting of all the branches connected to node ‘i’ and γ_i is zero for all terminal node.

So the current $I(i)$ connected to end node ‘i’ can be expressed as

$$I(i) = I_L(i) \quad (7)$$

So equation (6) and (7) are utilized in backward sweeps from all end nodes towards the root node for calculation of current.

4.2.1 Calculation of real and reactive power losses

The real and reactive power loss of a distribution system can be expressed as given below

$$P_L(i) = |I(i)|^2 R(i) \quad (8)$$

$$Q_L(i) = |I(i)|^2 X(i) \quad (9)$$

V. OPTIMAL NODE DETERMINATION USING FUZZY EXPERT SYSTEM (FES)

For a given single source radial distribution system it is not possible to reduce the losses which are associated with real and reactive component of the branch currents because all these real and reactive power is supplied by the single source at the source node. This limitation can be overcome by placing DG units at different nodes of the system for loss reduction. So the real and reactive powers are generated locally by installed DG unit. The location of DG is chosen based on fuzzy expert system. The location must be one that gives minimum losses along with the best voltage profile.

5.1 FES implementation

The fuzzy expert system (FES) consists of a set of rules. These rules are developed in a standard way. Different rules are designed and defined to determine the suitable node at which DG could be placed in fuzzification process. In the fuzzification process, the power loss factor (PLF) and voltage index (VI) are converted into fuzzy. Linguistic terms for power loss factor (PLF) is described by very low (VL), low (L), medium low (ML), medium high (MH), high (H), very high (VH) and linguistic terms for voltage index is described as low (L), medium low (ML), medium (M), medium high (MH), high (H). Different membership functions are generated to represent all these linguistic terms. Trapezoidal type membership functions are used in the following fuzzy expert system and they are shown in the Fig. 3 and Fig. 4 respectively.

The power loss factor (PLF) and the voltage index (VI) are the two inputs to the fuzzy (FIS), which determines the optimal position for allocation of DG by fuzzy inferencing. The inference involves heuristic rules for the determination of output decisions. In this fuzzy inference system there are two input variables (PLF, VI) and (7, 5) fuzzified variables respectively so that the fuzzy inference system has a set of 35 rules.

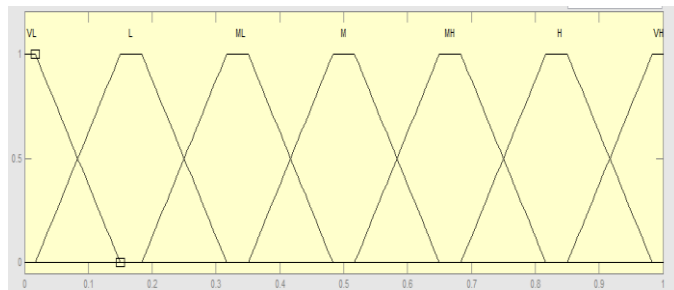


Fig.3. Power loss factor membership functions.

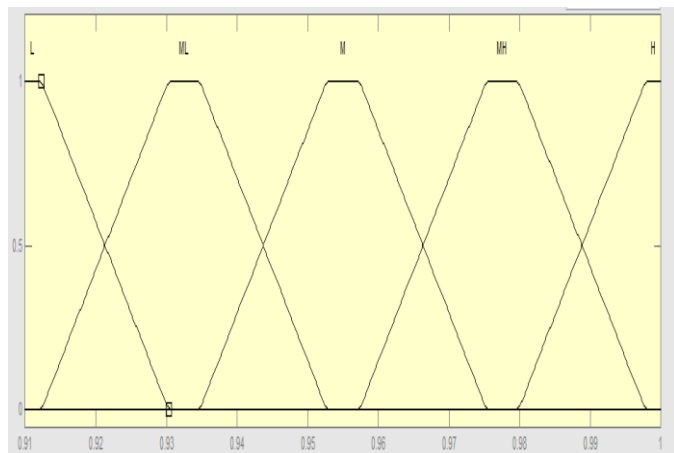


Fig.4. Voltage index membership functions

The DG unit is allocated in a radial distribution system in such a way that power loss factor should be maximum and the voltage index should be minimum. These two objectives are more important while designing the heuristic rules for fuzzy inference system (FIS). All these rules are expressed as the following way:

IF premise (antecedent).THEN conclusion (consequent).

To determine the DG suitability at a node a set of fuzzy rules have been employed. The rule base for optimal DG placement is presented in the fuzzy decision matrix shown in Table 2 and illustrated in Fig. 6. The output of fuzzy inference system is DG placement suitability index and it is also described by the linguistic terms very low (VL), low (L), medium low (ML), medium (M), medium high (MH), very high (VH). These linguistic terms are also represented by membership functions and it is shown graphically in Fig.5.

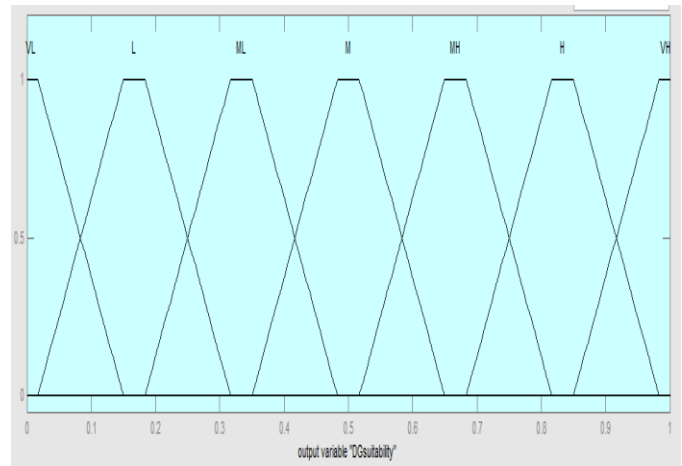


Fig.5. DG placement suitability index membership functions

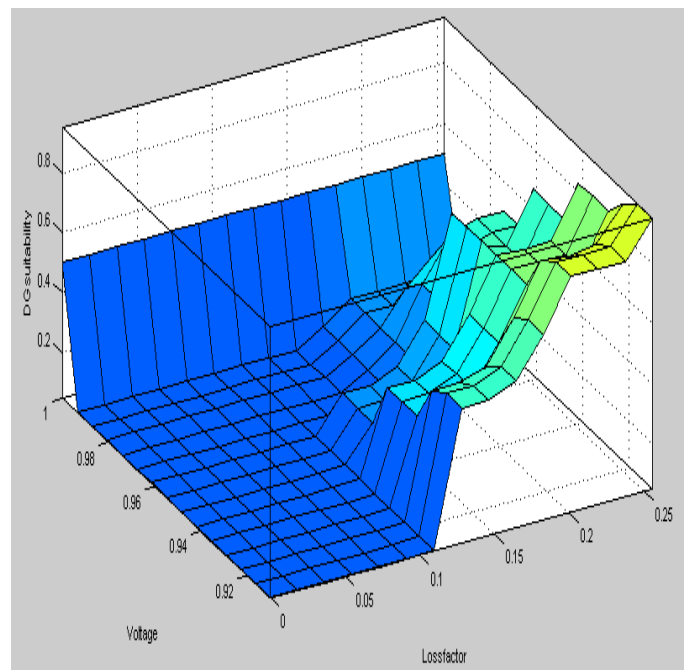


Fig.6. Fuzzy rules in graphical representation

TABLE II
FUZZY DECISION MATRIX

AND	Voltage index (VI)					
		Low (L)	Medium Low (ML)	Medium (M)	Medium High (MH)	High (H)
Power loss factor (PLF)	Very Low (VL)	VL	VL	VL	VL	VL
	Low (L)	VL	VL	VL	VL	VL
	Medium Low (ML)	M	ML	L	VL	VL
	Medium (M)	MH	M	ML	L	L
	Medium High (MH)	H	MH	MH	ML	L
	High (H)	H	MH	M	M	ML
	Very High (VH)	VH	H	MH	M	L

5.2 Fuzzy inference and defuzzification technique

Several rules are implemented with some degree of membership after the inputs are given to the fuzzy expert system (FES) which is obtained from the load-flow program i.e. power loss factor and voltage index. In this fuzzy expert system method Mamdani’s maximum-minimum method of inference has been used. Regarding the DG placement problem, the DG suitability membership function, μ_s of node i for k fired rules are given by the equation (10)

$$\mu_s(i) = \max[\min[\mu_p(i), \mu_v(i)]] \tag{10}$$

The two membership functions of power loss factor and voltage index are represented by μ_p and μ_v respectively. After the calculation of DG suitability membership function for a particular node it must be defuzzified to a scalar value. This defuzzification method helps to determine the ranking of different node’s suitability. To defuzzify the fuzzified values a centroid method has been used. DG suitability index can be determined as,

$$S = \frac{\int \mu_s(z).zdz}{\int \mu_s(z)dz} \tag{11}$$

VI. OPTIMAL DG SIZING BY ANALYTICAL METHOD

We are considering $a = (sign)\tan(\cos^{-1}PF_{dg})$ [17] for optimal positioning of a DG unit in a radial distribution system. The reactive power generated by a DG unit can be expressed by the following equation as:

$$Q_{dgi} = aP_{dgi} \tag{12}$$

In which

- $sign = +1$: reactive power supplied by a DG.
- $sign = -1$: reactive power absorbed by a DG.
- PF_{dg} = Power factor of DG

The active power and reactive power injected at bus i by a DG can be given by the following equation (13) and (14).

$$P_i = P_{dgi} - P_{di} \tag{13}$$

$$Q_i = Q_{dgi} - Q_{di} = aP_{dgi} - Q_{di} \tag{14}$$

From equation (1), (13), (14) the active power loss which occurred in the distribution system can be computed in the following way

$$P_L = \sum_{i=1}^N \sum_{j=1}^N [\alpha_{ij}[(P_{dgi} - P_{di})P_j + (aP_{dgi} - Q_{di})Q_j] + \beta_{ij}[(aP_{dgi} - Q_{di})P_j - (P_{dgi} - P_{di})Q_j]] \tag{15}$$

The partial derivative of Eq. (15) with respect to the active power injection from DG at bus ‘ i ’ becomes zero to obtain reduced active power loss.

$$\frac{\partial P_L}{\partial P_{dgi}} = 2 \sum_{j=1}^N [\alpha_{ij}(P_j + aQ_j) + \beta_{ij}(aP_j - Q_j)] = 0 \tag{16}$$

Equation (16) can be written in the following way:

$$\alpha_{ii}(P_i + aQ_i) + \beta_{ii}(aP_i - Q_i) + \sum_{j=1, j \neq i}^N (\alpha_{ij}P_j - \beta_{ij}Q_j) + a \sum_{j=1, j \neq i}^N (\alpha_{ij}Q_j + \beta_{ij}P_j) = 0 \tag{17}$$

Now Let $X_i = \sum_{j=1, j \neq i}^N (\alpha_{ij}P_j - \beta_{ij}Q_j)$

And $Y_i = \sum_{j=1, j \neq i}^N (\alpha_{ij}Q_j + \beta_{ij}P_j)$ (18)

From the equation (13), (14), (17) and (18) we can obtain the equation (19) state as below

$$\alpha_{ii}(P_{dgi} - P_{di} + a^2P_{dgi} - aQ_{di}) + \beta_{ii}(Q_{di} - aP_{di}) + X_i + aY_i = 0 \tag{19}$$

Rearranging the above equation we can obtain equation (20) to get the formulae to compute the best size of a DG to be placed in distribution system to reduce losses

$$P_{dgi} = \frac{\alpha_{ii}(P_{di} + aQ_{di}) + \beta_{ii}(aP_{di} - Q_{di}) - X_i - aY_i}{a^2\alpha_{ii} + \alpha_{ii}} \tag{20}$$

The power factor of a DG unit is very important to minimize the total system losses and it also depends upon the DG type and its operating condition. When the power factor of a DG unit is specified then its size can be determined in the following way:

Type 1 DG: This kind of DG is injecting only active power such as fuel cells, photovoltaic system, micro-turbines. Power factor is unity for this type i.e. $PF_{dg} = 1$, $a = 0$. By reducing the equation (21) we can get the size of Type 1 DG.

$$P_{dgi} = P_{di} - \frac{1}{\alpha_{ii}} \left[\beta_{ii} P_{di} + \sum_{j \neq i}^N (\alpha_{ij} P_j - \beta_{ij} Q_j) \right] \quad (21)$$

Type 3 DG: This kind of DG is generating active power as well as reactive power such as diesel generators. Power factor is in the range $0 < PF_{dg} < 1$, $sign = +1$ and a is a constant. The best size of Type 3 DG for minimum loss can be obtained from the equation (14) and (20).

6.1 Optimal power factor

Let a distribution system having two buses, a source, a load. The DG unit is connected at load end as shown in Fig.6.

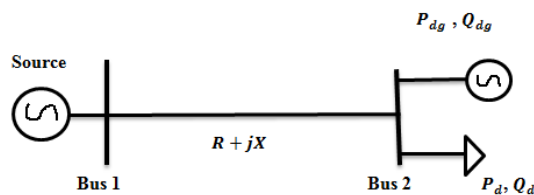


Fig.6. Distribution system with single DG unit.

PF of the single DG (PF_{dg}) connected to the distribution system can be obtained as,

$$PF_{dg} = \frac{P_{dg}}{\sqrt{P_{dg}^2 + Q_{dg}^2}} \quad (21)$$

PF of a single load (PF_d) can be obtained as,

$$PF_d = \frac{P_d}{\sqrt{P_d^2 + Q_d^2}} \quad (22)$$

When the PF of a single DG is equal to PF of combined load at that time the total load PF can be computed by Eq. (22) at that calculation the total active and reactive power can be obtained as,

$$P_d = \sum_{i=1}^N P_{di} \quad (23)$$

$$Q_d = \sum_{i=1}^N Q_{di} \quad (24)$$

It is found that minimum loss will be obtained if the power factor of DG (PF_{dg}) is equal to power factor of total load (PF_d). This can be expressed by equation (25)

$$PF_{dg} = PF_d \quad (25)$$

6.2 Computational procedure for the approach

The procedure to allocate a DG unit for loss minimization in a radial distribution system represented as below:

Step 1) Run the forward/ backward sweep load-flow for base case and find each branch as well as total losses and node voltages for the specified test system.

Step 2) Find the optimal node to allocate a DG unit.

(a) Develop the two input membership functions based on branch losses and node voltages and one output membership function of DG suitability index.

(b) Develop fuzzy rules (5×7) using Mamdani's method and defuzzify that to get optimal node for DG placement.

Step 3) Find the optimal power factor using equation (25).

Step 4) Obtain the optimal size of DG and compute the losses using the following steps:

(a) Allocate the DG unit at the appropriate position obtained from step 2, and vary the DG sizes in a very small steps using equation (14), (20), (21), by updating the values of ' α ' and ' β ' and finally compute the total real power losses by using the steps given below

(b) Select and store the DG size which gives minimum losses and discard other results.

Step 5) Update load data which is obtained in step 3, after allocating the DG unit with optimal size.

Step 6) Stop the procedure if the following occurs:

(a) If the voltage value at a particular node violate its upper limit.

(b) If the loss obtained in new iteration is greater than the previous iteration loss then the previous iteration loss is saved (or) repeat steps 1 to 5.

VII. RESULTS AND DISCUSSIONS

The methodology has been tested on IEEE 33 bus test system. This test system has real and reactive load of 3.715 MW and 2.3 MVAR respectively [29]. It is found that combined load PF of the system is about 0.85 lagging. The computer program has been implemented in MATLAB 2014 for estimation of losses with/without DG for the given test system. The fuzzy toolbox is also used to solve the optimal position problem of DG unit (Type1 and Type 3).

TABLE III
NODE VOLTAGES OF TEST SYSTEM WITH/WITHOUT DG UNIT

Node number	Node voltages without DG	Node voltage with Type 1 DG	Node voltage with Type 3 DG
1	1.000000000	1.000000000	1.000000000
2	0.997039361	0.998654349	0.999131941
3	0.982982915	0.993247363	0.996257585
4	0.975529053	0.992202789	0.997063298
5	0.968160451	0.991517465	0.998285682
6	0.949813660	0.987770407	1.001485037
7	0.946361134	0.984283150	0.998207992
8	0.941515601	0.979660855	0.993624526
9	0.935265575	0.973609229	0.987710219
10	0.929468555	0.968000431	0.982225353
11	0.928608019	0.967180532	0.981412025
12	0.927107591	0.965750144	0.979993996
13	0.921021555	0.959842463	0.974236052
14	0.918775865	0.957627812	0.972109060
15	0.917374388	0.956254483	0.970782383
16	0.916013920	0.954931635	0.969495316
17	0.914010371	0.952949948	0.967597348
18	0.913406606	0.952363422	0.967026217
19	0.996511413	0.998126964	0.998605169
20	0.992937295	0.994556829	0.995038978
21	0.992233905	0.993854055	0.994337184
22	0.991597779	0.993218410	0.993702520
23	0.979398339	0.989695290	0.992722822
24	0.972730390	0.983082611	0.986148815
25	0.969407570	0.979787464	0.982872917
26	0.947897949	0.985964576	0.999673351
27	0.945353259	0.983568876	0.997267145
28	0.933954444	0.972714394	0.986487659
29	0.925770144	0.964934940	0.978748585
30	0.922247158	0.961638965	0.975417874
31	0.918068967	0.957577271	0.971467673
32	0.917148828	0.956679505	0.970597711
33	0.916863664	0.956400843	0.970328094

Based on the proposed method the base case power flow gives the total real power loss 201.7543 kW and the fuzzy expert system gives the optimal node 6 for DG placement. The analytical method already written in section VI gives the optimal size of Type 1 and Type 3 DG unit 2.59 MVA and 3.1 MVA respectively. The percentage of loss reduction after the allocation of Type 1 and Type 3 DG unit is 49.05% and 69.44% respectively. It is also proved that the DG with the power factor equal to combined load power factor i.e. 0.85 lag gives the best result as compared to others.

TABLE IV
DG SIZES WITH OPTIMAL POWER FACTOR AND PERCENTAGE OF LOSS REDUCTION

Optimal power factor	Minimum real power loss (kW)	DG size (MVA)	Optimum location	Percentage of loss reduction
unity	102.7790	2.59	6	49.05%
0.85 lag	61.6505	3.1	6	69.44%

TABLE V
COMPARISON OF THE RESULTS OF DIFFERENT APPROACHES FOR TYPE 1 DG UNIT

Method	Optimal location	DG size (MVA)	Percentage of loss reduction
PSO [31]	6	2.567	47.40%
ABC [32]	6	3.380	44.83%
PSO [33]	6	2.570	47.37%
Proposed Fuzzy based approach	6	2.590	49.05%

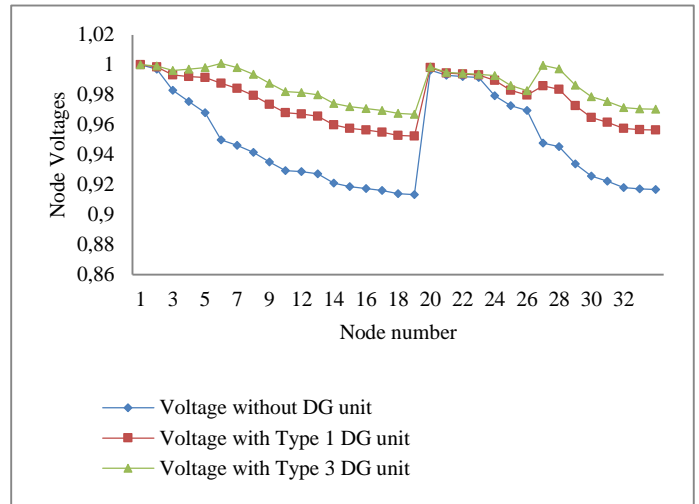


Fig.7 Voltage profile with/ without DG unit.

The voltage profile improvement and percentage of loss reductions are shown in TABLE III and TABLE IV respectively. A graphical representation of voltage profile improvement and real power losses for Type 1 and Type 3 DG unit are shown in Fig.7 and Fig.8 respectively. From the Fig.7 it is observed that the voltage profile of the given bus system is improved more by installing Type 3 DG unit as compared to Type 1 DG unit. TABLE V represents the results of the analytical methods using PSO [31], ABC [32] and other evolutionary techniques (PSO) [33] and these results are compared with the proposed fuzzy-based method to allocate Type 1 DG unit.

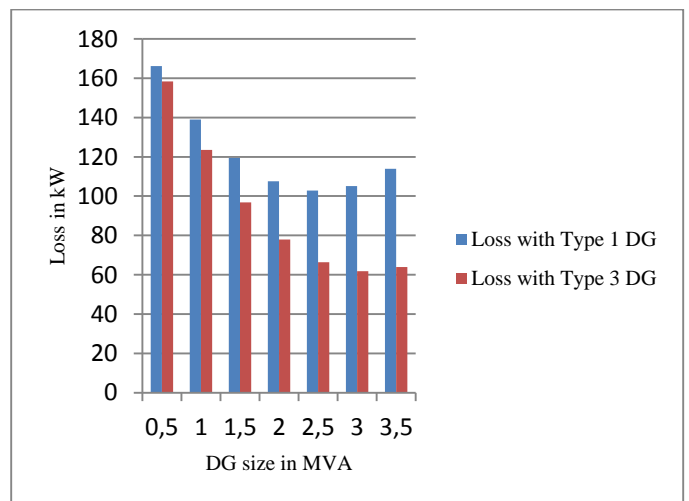


Fig.8 Real power loss reduction by Type 1 and Type 3 DG unit

VIII. CONCLUSION

This paper presents a novel fuzzy expert system to find the optimal node for DG allocation to minimize the real power losses in a radial distribution system as well as to improve the voltage profile. The sizing problem is solved using an analytical method considering combined load power factor. Validity of the method is tested on IEEE 33-node radial distribution system. Results showed that appropriate size, location and power factor of a DG unit will lead a significant role to minimize the losses in distribution system.

IX. ACKNOWLEDGEMENT

The author would like to acknowledge Faculty of Electrical and Instrumentation Engineering, Thapar University, Patiala in supporting this work.

REFERENCES

- [1] R.S Rao, K Ravindra, K. Satish and S.V.L Narasimham, "Power loss minimization in distribution system using network reconfiguration in the presence of distributed generation." IEEE Transactions on Power system, vol. 28, no. 1, pp. 317-325, Feb. 2013.
- [2] P. Chiradeja and R. rajkumar, "An approach to quantify the technical benefits of distributed generation." IEEE Transactions on Energy Conversion, vol. 19, no. 4, pp. 764-773, Dec. 2004.
- [3] R.A. Gallego, A.J. Monticelli and R. Romero, "Optimal capacitor placement in radial distribution networks." IEEE Transactions on Power Systems, vol. 16, no. 4, pp. 630-637, Nov. 2001.
- [4] Y.H. song, G.S. Wang, A.T Johns and P.Y Wang, "Distribution network reconfiguration for loss reduction using fuzzy controlled evolutionary technique." Proceedings. IEE, Generation Transmission and Distribution, vol. 144, no. 4, pp. 345-350, Jul. 1997.
- [5] T.N Shukla, S.P Singh, V Srinivasrao and K.B. Naik, "Optimal sizing of distributed generation placed on radial distribution system." Electric Power Components Systems, vol. 38, no. 3, pp. 260-274, 2010.
- [6] M. Raoufat and A.R. Malekpour, "Optimal allocation of distributed generation and remote controllable switches to improve the network performance considering operating strategies of distributed generations." Electric Power components systems, vol. 39, no. 16, pp. 1809-1827, 2011.
- [7] El-Hattam and M.M.A Salama, "Distributed generation technologies, definitions and benefits." Electric Power system Research, vol. 71, no. 2, pp. 119-128, 2004.
- [8] M. Gomez-Gonzalez, F.J Ruiz-Rodriguez and F. Jurado, "A binary SFLA for probabilistic three-phase load flow in unbalanced distribution systems with technical constraints." International Journal of Electric Power and energy Systems, vol. 48, no. 1, pp. 48-57, 2011.
- [9] T.D.T Naguyen, J. ruan, Q.N. Naguyen, N.G. Lee, D. Tan and L. Hu, "Study of Economical-technical impacts of distributed generation on medium voltage grid." Telkonnika, vol. 12, no. 2, pp. 1177-1187, 2014.
- [10] A.S.A Awad, T.H.M El-Fouly and M.M.A. Salama, "Optimal distributed generation allocation and load shedding for improving distribution system reliability." Electric Power Components Systems, vol. 42, no. 6, pp. 576-584, 2014.
- [11] N.S. Rau and Y.H. Wan, "Optimal location of resources in distributed planning." IEEE Transactions on Power Systems, vol. 9, no. 4, pp. 2014-2020, 1994.
- [12] H.L. Willis, "Analytical methods and rules of thumb for modeling DG distribution interaction." In Proceedings of IEEE Power Energy Society summer meeting 2000, pp. 1643-1644.
- [13] Wang C, Nehrir MH, "Analytical approaches for optimal placement of distributed generation sources in power system." IEEE Transaction on Power System, vol. 19, no. 4, pp. 2068-2076, 2004.
- [14] P.M. Costa and M.A. Matos, "Avoided losses in a LV networks as a result of microgeneration." Electric Power System Research, vol. 79, no. 4, pp. 629-634, 2009.
- [15] T. Gozel, M.H.Hocaoglu, "An analytical method for the sizing and siting of the distributed generators in radial system." Electrical Power System and research, vol. 79, no. 6, pp. 912-918, 2009.
- [16] S.H. Lee and J.W Park, "Selection of optimal location and size of multiple distributed generation by using kalman filter algorithm." IEEE Transactions on Power Systems, vol.24, no. 3, pp. 1393-1400, 2009.
- [17] D.Q. Hung, N. Mithulananthan, R.C. Bansal, "Analytical expressions for DG allocation in primary distribution network." IEEE Transaction on Energy Conversion, vol. 25, no. 3, pp. 814-820, 2010.
- [18] N. Acharya, P. Mahat, N. Mithulananthan, "An analytical approach for DG allocation in distribution network." International Journal of Electric Power and Energy System, vol.28, no. 10, pp.669-678, 2006.
- [19] H.M. Khodr, M.R. Silva, Z. Vale and C. Ramos, "A probabilistic methodology for distributed generation location in isolated service area." Electric Power System and Research, vol. 80, no. 4, pp. 390-399, 2010.
- [20] J.A.M Garcia and A.J.G Mena, "Optimal distributed generation location and sizing using modified teaching learning based optimization algorithm." Electric Power and Energy systems, vol. 50, pp. 65-75, 2013.
- [21] S.M. Sajjadi, M.R. Haghifam and J. Salehi, "Simultaneous placement of distributed generators and capacitors in distribution networks considering voltage stability index." Electric Power and Energy systems, vol. 46, pp. 366-375, 2012.
- [22] K.D. Mistry and R. Roy, "Enhancement of loading capacity of distribution system through distributed generators placement considering techno-economic benefits of load growth." Electric Power and Energy Systems, vol. 54, pp. 505-515, 2014.
- [23] Attia El-Fergany, "Optimal allocation of multi-type distributed generators using backtracking search optimization algorithm." Electric Power and Energy Systems, vol. 64, pp. 1197-1205, 2015.
- [24] S.M. Moghaddas-Tafreshi and Elahe Mashour, "Distributed generation modeling for power flow studies and three phase unbalanced power flow solution for radial distribution system considering distributed generations." Electric Power System Research, vol. 79, no. 4, pp. 680-686, 2009.
- [25] J-H. Teng, "Modeling of distributed generations in three-phase distribution load flow" IET Generation Transmission and Distribution, vol. 2, pp. 330-340, 2008.
- [26] H.E Farag, H.F El-Sadany, R. El-Shatshat and A. Jidan, "A generalized power flow analysis for distribution system with high penetration of distributed generation." Electric Power System Research, vol. 81, no. 7, pp. 1499- 1506, 2011.
- [27] S. Ghosh and D. Das, "Method for load-flow solution of radial distribution networks." IEE Part C, Generation Transmission and Distribution, vol. 146, no. 6, Nov. 1999.
- [28] L. Wang and C. Singh, "Reliability constrained optimal placement of reclosures and distributed generators in distribution networks using an ant colony system algorithm." IEEE Transactions on systems, man and cybernetics, Part C: Application and Review, vol. 38, no. 6, pp. 757-764, 2008.
- [29] M.E Baran and F.F. Wu, "Network reconfiguration in distribution systems for loss reduction and load balancing." IEEE Transactions on Power Delivery, vol. 4, no. 2, pp. 1401-1407, 1989.
- [30] D.P. Kothari and J. S. Dhillon, Power System Optimization, New Delhi: Prentice-Hall, India, 2006.
- [31] A.A Bagheri, A. Habibzadeh, S.M Alizadeh "Comparison of the effect of combination of different DG types on loss reduction using A PSO algorithm." Canadian Journal of Electrical and Electronics Engineering, vol 2, pp. 468-474, 2011.
- [32] F.S Abu-Mouti, M.E. El-Hawary, "Optimal distributed generation allocation and sizing in distribution systems via artificial bee colony algorithm." IEEE Transactions on Power Delivery, vo. 26, no. 4, pp. 2090, 2101, 2011.
- [33] Peyman Karimyan, G.B. Gharehpetian, M. Abedi and A. Gavili, "Long term scheduling for optimal allocation and sizing of DG unit considering load variations and DG type." Electrical Power and Energy Systems, vol. 54, pp. 277-287, 2014.

BIOGRAPHIES



AVIK METIA received B.Tech from West Bengal University of Technology in Electrical Engineering in the year of 2012. He is currently pursuing M.E in Power System in Thapar University, Patiala, India, in the Department of Electrical and Instrumentation Engineering. His research interest includes distribution system, distributed generation unit and different loss minimization techniques used in distribution

system.



SMARAJIT GHOSH serving as a Professor in Thapar University, Department of Electrical and Instrumentation Engineering. He did his B.Sc (Physics Hons.), B.Tech,(Electrical Engineering) and M.Tech (Electrical Machines and Power Systems) from Calcutta University in 1991, 1994 and 1996 respectively. Finally, he did his Ph.D. from Indian Institute of Technology, Kharagpur, India in 2000. His research areas include load-flow study, network reconfigurations, optimum capacitor allocation,

and application of soft computing in Electrical Power Distribution Systems.

No-load electromagnetic simulations of a hydropower generator considering the effect of rotor whirling

Y. Calleecharan, J.O. Aidanpää, and J.R. Brauer, *Life Fellow IEEE*

Abstract—Electromagnetic (EM) analysis of hydropower generators is common practice but there is little emphasis on studying the effect of rotor whirling in the analysis. This paper explores the effect on electromagnetic analysis as the rotor is allowed to whirl both in forward and in backward directions under no-load conditions. As a hydropower generator rotor shaft can experience whirling when under eccentric operation, the objective is to examine how whirling can affect the unbalanced magnetic pull (UMP), flux densities, damper currents, and ohmic losses in a synchronous hydropower generator. These results are obtained in a commercial FEM-based EM field modelling software package that allows various degrees of freedom in motion types and multiple motion components to be set. It is seen that backward whirling tends to induce higher eddy currents than forward whirling does.

Index Terms—eccentricity, electromagnetic simulations, hydropower rotor, no-load, whirl

NOMENCLATURE

Γ	domain boundary
μ	magnetic permeability [H/m]
σ	electrical conductivity [S/m]
ρ_V	charge density [C/m ³]
ω	angular velocity [rad/s]
Ω	domain
∇	differential operator
\mathbf{A}	magnetic vector potential [T m = Wb/m]
\mathbf{B}	magnetic flux density [T]
\mathbf{D}	electric flux density [C/m ²]
\mathbf{E}	electric field strength [V/m]
f	frequency in linear spectrum estimation [Hz]
F	Force [N]
\mathbf{H}	magnetic field strength [A/m]
\mathbf{J}	current density [A/m ²]
l	frequency index in linear spectrum estimation
n	time index in linear spectrum estimation
N	positive integer number
t	time [s]
U	window-dependent resolution bandwidth normalisation factor
UMP	unbalanced magnetic pull [N]
\mathbf{v}	velocity [m/s]
w	data window
\hat{X}	one-sided linear spectrum estimate

Y. CALLEECHARAN is with the Department of Mechanical and Production Engineering, University of Mauritius, Réduit, 80837, Mauritius (email: y.calleecharan@uom.ac.mu).

J.O. AIDANPÄÄ is with the Department of Engineering Sciences and Mathematics, Luleå Tekniska Universitet, Luleå, 971 87, Sweden (email: joa@ltu.se).

J.R. BRAUER is with the Department of Electrical Engineering and Computer Science, Milwaukee School of Engineering, Milwaukee, Wisconsin, 53202, USA (email: jbrauer@ieee.org).

subscripts & superscripts

ro	rotor
s	sampling
wh	whirl
whr	whirl ratio
0	impressed current
c	conducting
n	non-conducting
LS	linear spectrum

I. INTRODUCTION

ROTOR-stator eccentricity in electrical machines is an issue that has caught attention for a long time [1], [2] and is an important item in condition monitoring [3] in electrical machines. Though many papers in the literature [4]–[8] have addressed the issue of eccentricity in rotating electrical machines, there has been a paucity of papers that account for the effect of whirling of the rotor. Examples of publications that have considered whirling include [9], [10].

Rotor whirling in hydropower machines is not uncommon [11]. Whirling motion is associated with any eccentric motion of the rotor where the geometric centre of the rotor does not coincide with the axis of rotation of the rotor. In a two-dimensional setting neglecting mass eccentricity effects, we may say that a whirl velocity component only exists between two points when there is relative motion between them. The simplest form of whirling thus occurs with a purely dynamic eccentricity motion and the latter is discussed in the next section. Whirling in a hydropower rotor can occur apart from unbalance effects because of, for example, play in bearings, the pulling effect of the UMP and also water forces hitting the turbines' blades that can aggravate any pre-existing play in the bearings supporting the rotor. While backward whirling of a rotor is considered to occur less commonly in practice, the electromagnetic (EM) simulations in the present paper aims to investigate the effects of both forward (positive direction) and backward (negative direction) motion types of the rotor. It has been found that many FEM-based EM field modelling software packages cannot handle dynamic eccentricity motion, and worse a combination of static and dynamic eccentricities motion. The latter motion combination is more amenable to model what actually happens in a hydropower machine but will not be discussed in this paper. A large majority of existing FEM-based EM software products cannot handle eccentricity cases and have made no provisions for the user to be able to add whirling effects since there can be perhaps only very little demand from users to simulate whirling behaviour. And it turns out that the main users of these FEM-based EM software packages are electrical machine designers whose primary interests rest in the electrical characteristics of a machine rather in their electromechanical aspects.

Previous works [12], [13] carried out by two of the authors have had goals to examine the rotor movements and the stability of an industrial hydropower generator under a purely dynamic eccentricity motion. These two papers however only emphasised the importance of whirling as a mechanical issue and not as an electromechanical one. The present paper takes a step back and investigates what useful

information can be gained rather directly from the field solutions in the EM analysis, and indirectly from post-processed results in the software package under zero eccentricity condition, a purely static eccentricity condition, and finally a purely dynamic eccentricity condition. In a future work, it is hoped that a more electromechanical approach can thus be undertaken whereby EM field solutions and post-processed results can be linked seamlessly with a mechanical analysis.

The simulations in this article furthermore demonstrate the capabilities of one FEM-based EM field modelling software product. There is a need to motivate electrical machine designers on the need to consider whirling of the rotor when designing hydropower generators as whirling effects occur in reality. Thus to aid the machine designers, information on the EM field solutions such as the flux densities and ohmic losses are provided in addition to current waveforms, and forces (unbalanced magnetic pull) due to eccentricity effects or asymmetry in flux distribution around the rotor. This information will normally complement a dynamic analysis of the generator. Examples of dynamic analyses for a generator considering both the range of forward and backward whirls, and where a purely dynamic eccentricity motion exists are given in [12], [13].

Present models in the hydropower industry in Sweden use only a single value of the unbalanced magnetic pull (UMP) (see e.g. [12]). Though this UMP value tells us the maximum radial force (at synchronous rotor whirl) and hence the maximum force acting between the rotor and the stator given that the radial force is normally greater than the tangential component, relying upon this single value estimate can be misleading as was shown in [12], [13]. This is because the whirling frequency of the rotor is changing all the time when the generator is under operation in an actual hydropower machine, and one has to consider the effect of both the radial and the tangential forces then so as to grasp the dynamics of the machine. Hence the present paper also comes in as a step to strengthen the fact that a complete EM analysis of a hydropower generator needs consideration of the whirling frequency of the rotor both in the positive and in the negative whirl directions.

A small-scale synchronous generator [14] which has been specially made available for hydropower research is used in this study. Measurements have not been performed by the authors. However, it is mentioned in Section IV-A that an experimental measurement of the force or the UMP was carried out by Uppsala Universitet [14] on a static eccentricity motion case. Simulations and analysis by the present authors have then become possible after the FEM-based software package used in the present paper reported in a corresponding static eccentricity simulation a UMP magnitude value comparable to that obtained in the experimental measurement.

There is also a caveat in doing proper eccentricity measurements in an experimental setup. If one is able to set up a desired purely static eccentricity or a purely dynamic eccentricity on a rotor, it is to be realised that when the generator is put in service, then any UMP that arises because of the eccentricity or because of any other reason that leads to an asymmetric distribution of flux around the rotor will affect the eccentricity value set by the experimenter on the rotor. This implies that the eccentricity at which one is doing the measurement will change value, making the measurement of the UMP in practice rather an impossible task at the given fixed eccentricity setting of the rotor that is set and sought by the experimenter.

II. CLARIFICATION OF STUDIED ECCENTRICITY TYPES

Two types of eccentricities in a two-dimensional setting are considered in this article, namely purely static eccentricity and purely dynamic eccentricity. Mixed eccentricities, whereby both types of eccentricities are present, are not within the scope of the present study

though in practice separating a mixture of these two types of eccentricities can be an impossible task. It is to be reminded that an actual generator rotor motion is inclined to embrace a mixed eccentricities motion in practice. Also, eccentricities that involve offset of the stator bore centre or simultaneous offset of the former together with offset of the rotor centre are not treated in this paper. The two types of eccentricities are shown in Fig. 1. It is to be noted that though a static eccentricity in the positive Cartesian x -direction (see Fig. 1a) has been studied in this article, eccentricities in other Cartesian directions (positive and negative) have as similar corresponding behaviours as that displayed by the considered positive x -direction eccentricity.

In the case of a purely static eccentricity in the positive Cartesian x -direction which is shown in Fig. 1a, the axis of rotation of the rotor (marked as x in the figure) and the geometric centre of the rotor (marked as o) coincide with each other, and are at an eccentric distance in the positive x -direction from the geometric centre of the stator bore (marked as $+$). Put in another words, for a static eccentricity in the positive x -direction, the geometric centre of the rotor is displaced by x_s in the positive x -direction from the geometric centre of the stator bore. Since the geometric centre of the rotor coincides with the axis of rotation of the rotor based on the sound assumption that there is usually no unbalance in the rotor, the axis of rotation of the rotor is also displaced by the vector $(x_s, 0)$ from the stator bore centre.

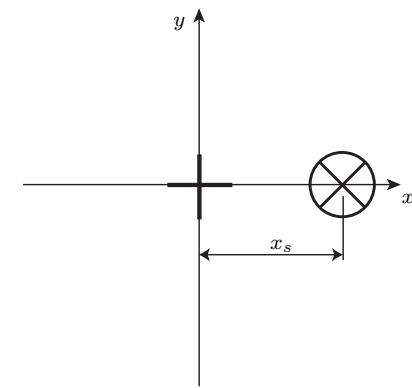
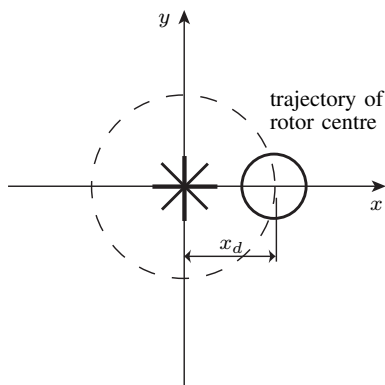
The case with a purely dynamic eccentricity is more complex to describe. In this case, the following conditions apply to Fig. 1b:

- The axis of rotation of the rotor (marked as x in the figure) coincides with the geometric centre of the stator bore (marked as $+$ in the figure);
- The axis of rotation of the rotor is displaced by a dynamic offset vector from the geometric centre of the rotor;
- The geometric centre of the rotor (marked as o in the figure) orbits around the geometric centre of the stator bore;
- The geometry is invariant with position along the machine axis.

For a purely dynamic eccentricity say of dynamic offset vector $(-x_d, 0)$, at time $t = 0$ the geometric centre of the rotor is displaced by a distance of $+x_d$ from the geometric centre of the stator bore. The axis of rotation of the rotor remains concentric with the stator bore and is displaced by a distance $-x_d$ in the x -direction at the same time instant $t = 0$ from the geometric centre of the rotor. As the rotor revolves, the geometric centre of the rotor traces out a circular path which is concentric with the geometric centre of the stator bore. This circular path is shown by the dotted circle in Fig. 1b.

A 10 % eccentricity value or ratio was used in this paper in the purely static and purely dynamic eccentricities simulations since manufacturers tend to limit the amount of eccentricity to this value [15]. This 10 % eccentricity value or ratio for the generator studied in this article is taken of the mean air-gap length given in Table I. Of importance is to note that rotors in hydropower generators are normally short and fat as opposed to long rotors used in turbo-generators.

There can be various reasons for the occurrence of rotor whirling as was briefly discussed in the introductory section. Mass eccentricity that entails unbalance only gives rise to synchronous whirling. This paper however is going beyond the usual simplification in literature that whirling solely refers to synchronous (forward) whirling. In a hydropower machine, the UMP and whirling mutually influence each other. This mutual effect can be too complex to model in a FEM-based EM software product. This issue is re-visited in the second paragraph in Section III-C. That being said, the UMP can be viewed as one factor that causes dynamic eccentricity and hence whirling since the radial UMP always tends to pull the rotor towards the stator bore inner surface, causing the rotor to bend. Another factor that can give rise to

(a) Purely static eccentricity in the x -direction

(b) Purely dynamic eccentricity

Fig. 1. The different eccentricity motion types explored in this paper are shown. Fig. 1a portrays a purely static eccentricity in the positive x -direction whereas Fig. 1b depicts the case of a purely dynamic eccentricity with the rotor centre taking the dotted path. The rotor geometric centre o is initially placed at the point $(x_d, 0)$. For the meaning of the symbols x , o and $+$, see text

the phenomenon of whirling in hydropower generators is the effect of the water hitting the turbines' blades that are fixed at the bottom of the rotor shaft. This external forcing due to the water brings about more play in the bearings that support the generator rotor, hence imparting whirling motion as well. A further example of a cause of whirling is an initially bent rotor taking the form of a circular arc between the bearings holding the generator rotor.

For the alternator under study, the direction of rotation of the rotor is counterclockwise viewing from above. This implies that with a positive whirling, the whirling takes place in the same direction as the rotating rotor and the path taken by the moving centre of the rotor then follows an anticlockwise direction along the dotted trajectory of Fig. 1b in the purely dynamic eccentricity motion. An explanation of having a whirling speed other than the synchronous mechanical angular velocity of the rotor, ω_{ro} , is in place here when considering a purely dynamic eccentricity motion. In particular, with the case of forward synchronous whirling i.e. when the whirling velocity has the same speed as ω_{ro} and the rotor is whirling in the same direction as the rotor spin, after one full revolution of the path that the geometric centre of the rotor takes, a fixed point on the rotor other than the latter's geometric centre has also undergone a similar full revolution. In other words, a cycle of whirling takes the same amount of time that the fixed point of the rotor takes to make one complete revolution. The case of non-synchronous whirling for a purely dynamic eccentricity motion in an EM analysis is rarely treated in the literature according

to the best knowledge of the authors. For the situation where there is whirling in the backward direction with a whirling speed say two times the speed ω_{ro} of the rotor, this means that a cycle of whirling takes half the amount of time that the aforementioned fixed point of the rotor takes to make one complete revolution. Put differently, the geometric centre of the rotor is moving much faster with twice the corresponding speed of ω_{ro} in the backward direction as opposed to the rotor that is rotating in the forward direction with a speed of ω_{ro} .

Fig. 1b also shows that there is just one whirl velocity component since we only have two points that are in relative motion with each other (in a two-dimensional frame). These two points are firstly the moving rotor centre on the dotted trajectory and secondly the fixed stator bore centre at $(0, 0)$. We have a constant whirling velocity since the magnitude of the dynamic offset vector that represents the eccentricity value or ratio is constant and the rotation velocity of the rotor geometric centre is uniform along the dotted trajectory.

III. THE GENERATOR MODEL

A. Physical parameters of the generator unit

A two-dimensional model of the rotor and the stator of the generator was considered sufficient for the modelling on the computer as skewing effect(s) of the rotor is(are) not accounted for. Thus the eccentricities and geometries considered are independent of the axial Cartesian direction z . The main parameters of the 185 kW 3-phase salient-pole type alternator that are useful in the simulations are given in Table I. The rotor poles sit outwards on the rotor rim which in turn is fixed on the spider. This is shown in Fig. 2. It is to be noted at this stage that the simulations in this article were carried out using the full two-dimensional model of the generator and not with just the one-pole pitch model as shown in Fig. 2 as eccentricity destroys any spatial periodicity in the EM model(s).

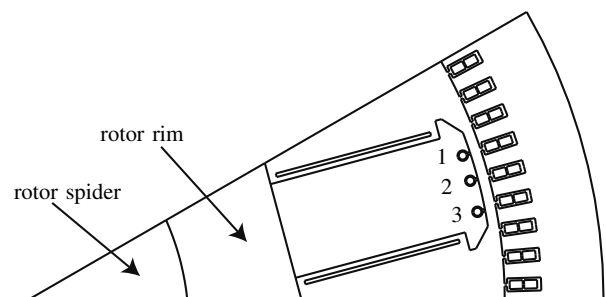


Fig. 2. Fig. shows the cross section of one EM model of the generator studied for one pole pitch only and when there is no eccentricity. The solid rotor rim sits on the solid spider. The uneven spatial distribution of the three damper bar slots on a pole shoe can also be seen. The two damper bars Bars 1 and 3 on every pole shoe are in an asymmetric configuration around the centre damper slot that holds Bar 2. More explicitly, if a line is drawn from the rotor geometric centre through the centre damper slot, then the angle subtended by the line from the rotor centre through the damper slot for Bar 3 is greater than the corresponding angle subtended for the damper slot with Bar 1 considered instead. In the simulations, the direction of rotation of the rotor is anticlockwise with Bar 1 leading. The damper bar slots are open at the top of the pole shoe

All the simulations in this paper are for the no-load case. This was preferred to the load condition since measurements are easier to do when currents are not flowing in the stator coils. Also, vibrations that appear when the generator is operating under a no-load condition may be masked once the stator terminals start supplying current to a load source.

TABLE I. Important dimensions and parameters of the generator

Parameter	Value
Rotor axial length [mm]	305
Rotor spider radius, [mm]	120.1
Rotor rim external radius [mm]	200.1
Rotor external radius ¹ [mm]	354.1
Mean air-gap length, [mm]	8.4
Mechanical angular velocity, ω_{ro} [rad/s]	52.36
Number of poles	12
Number of stator slots	108

¹ This includes the pole shoe height

B. The eddy current problem in a generator

In any electrical machine, there are regions which are conducting and regions which are not conducting in regard to eddy current presence [16]. If we write the Maxwell's Equations with respect to the fixed stator reference frame, then we have [17]

$$\begin{aligned}\nabla \times \mathbf{H} &= \mathbf{J} \\ \nabla \times \mathbf{E} &= -\frac{\partial \mathbf{B}}{\partial t} \\ \nabla \cdot \mathbf{D} &= \rho_V \\ \nabla \cdot \mathbf{B} &= 0\end{aligned}\quad (1)$$

$$\text{where } \mathbf{J} = \begin{cases} \mathbf{J}_0 & \text{in } \Omega_n \\ \sigma(\mathbf{E} + \mathbf{v}_{ro} \times \mathbf{B}) & \text{in } \Omega_c \end{cases} \quad (2)$$

In Equation (2), the region Ω_n refers to the non-conducting domain with boundary Γ_n and Ω_c refers to the eddy current conducting domain with Γ_c as its boundary respectively. A solution to the magnetic field in the whole domain $\Omega_n \cup \Omega_c$ only becomes possible when the coupling that exists at the interface(s) between the separate regions in terms of the continuity of $\mathbf{H} \times \mathbf{n}$ and $\mathbf{B} \cdot \mathbf{n}$ is maintained and the constitutive equations of matter are introduced as well. For a two-dimensional setting, a generator will have a magnetic vector potential A_z and current density J_z . Equations (1) and (2) can then be cast together as

$$-\frac{\partial^2 A_z}{\partial x^2} - \frac{\partial^2 A_z}{\partial y^2} = \mu J_z \quad (3)$$

and

$$-\frac{\partial^2 A_z}{\partial x^2} - \frac{\partial^2 A_z}{\partial y^2} = -\sigma \mu \frac{\partial A_z}{\partial t} + \sigma \mu \left(\mathbf{v}_{ro} \times \left[\frac{\partial A_z}{\partial y} - \frac{\partial A_z}{\partial x} \right] \right) \quad (4)$$

with the boundary condition as $A_z = 0$ on the stator yoke of the generator. A list of common assumptions governing Maxwell's equations as applied to electrical machines is listed in [18], [19].

Whirling term(s) is(are) not seen in Equations (3–4). This is because the FEM-based EM software product, MagNet [20], that is used accounts for the effect(s) of whirling in the modelling process and the user does not have access to the field equations being solved. By allowing multiple degrees of freedom to be set on the rotor with different motion components, the effect(s) of rotor whirling come(s) into being by relative motion between the geometric centre of the rotor and an axis of rotation of the rotor in the modelling stage. This axis of rotation in a purely static eccentricity as shown in Fig. 1a is at a fixed point $(x_s, 0)$ and for the case of a purely dynamic eccentricity is at the centre of the stator bore at the point $(0, 0)$ as displayed in Fig. 1b.

C. Parameters used in the simulations

For all the simulations, the EM model was set up with no running up of the rotor. In other words, the speed of the rotor was at its synchronous value right from the start of the simulations and this

remains so till the end of the simulations. Moreover, the model makes all current sources to be on at the onset of the simulations. The time step in the transient simulations had a value of 0.1 ms and it took 120 ms of simulation time for a fixed point on the rotor to make one complete revolution (see also Table II). For the eccentric motion simulations, the initial position of the rotor has been set to lie on the positive side of the Cartesian x -axis.

The two types of eccentricities that are covered in this article have been examined in Section II. As regard to the purely static eccentricity simulations, ten revolutions of the rotor were deemed necessary before steady state operation was reached. The steady state condition in the EM simulations can be gauged for instance by waiting for when the ohmic losses in the rotor rim stabilise. As for the purely dynamic eccentricity simulations, three rotor revolutions were prescribed irrespective of the whirling velocity and whirling direction that the rotor takes. It is to be expected that as the rotor whirls, the flux densities on the rotor vary as well which in turn affect the whirling velocity of the rotor. This additional complexity was not introduced in the model. The rotor has been set to whirl with a constant whirling velocity for the whole duration of the simulations. The goal with such a simulation type is to find the steady state field solutions corresponding to a particular whirling frequency.

Different whirling speeds have been considered in the simulations within a range of six times the synchronous velocity (or the rotor mechanical angular velocity) of $\omega_{ro} = 52.36$ rad/s both in the positive and in the negative whirl directions. This wide whirling frequencies span was considered suitable subject to a reasonable amount of computation time that it requires and of course it can be enlarged or decreased if desired. The range of whirling frequencies considered may be viewed as excessively wide. However, it is to be remarked that in the general case where a combination of purely static eccentricity and a purely dynamic eccentricity exists, then the whirling frequency may expect to vary by large amounts depending upon the static and dynamic eccentricity ratios therein. With mixed eccentricities motion, the whirling frequency of the moving geometric centre of the rotor with respect to the fixed stator bore centre becomes non-constant while the local whirling frequency, with respect to the axis of rotation at coordinates $(x_s, 0)$, due to the dynamic eccentricity component is still constant. So while considering a wide whirling ratio range $-6.0 \leq \omega_{whr} \leq 6.0$ in the purely dynamic eccentricity simulations may appear superfluous and not possibly be observed in practice, it is to be emphasised that mixed eccentricities motion reflects better the motion of a hydropower rotor and in this case the whirling ratios embrace a wide range of whirling frequencies. Hence, examining a wide ω_{whr} range as done in this paper is relevant as this wide range gives valuable information of the effect(s) of what a more accurate whirling behaviour due to mixed eccentricities motion can bring. A subset of whirling velocities have been picked to illustrate the results and these whirling frequencies are given in Table II. Halfway whirling ratio values of the extremum whirling ratios of -6.0 and 6.0 which are at $\omega_{whr} = -3.0$ and 3.0 respectively are proper choices to study.

Furthermore, in all the three sets of simulations for the no eccentricity case, the purely static eccentricity case and the purely dynamic eccentricity case, the magnetomotive force of the field windings was constant at 2430 A–turns. Also, the damper bars, which are made of copper, were connected in a circuit as a squirrel cage with interconnections between poles.

IV. RESULTS AND ANALYSIS

A. Force on the rotor

In this section, the forces acting on the rotor are presented for different cases, namely first for an ideal case without any rotor-stator eccentricity, secondly for a rotor that is statically eccentric at 10 %

TABLE II. Whirling speeds used in the simulations

Whirling ratio, ω_{whr}	Whirling speed, ω_{wh} [deg/s] ^a	Whirling speed, ω_{wh} [rad/s]
-6.0	-18 000	-314.16
-3.0	-9 000	-157.08
1.0 ^b	3 000	52.36
3.0	9 000	157.08
6.0	18 000	314.16

^a This unit can be conveniently set within MagNet [20]

^b This value represents (forward) synchronous whirl and has been included in the table to give an idea of the magnitudes of the whirling speeds used in the simulations

ratio in the x -direction and thirdly for a rotor that undergoes a purely dynamic eccentricity motion with 10 % offset or eccentricity ratio. For the latter case, the whirling speeds as listed in Table II are considered. MagNet [20] computes the forces acting on the rotor through the latter's centre of mass. For the rotor under study that is assumed to be homogeneous and that has a perfectly circular structure, this centre of mass coincides with the geometric centre of the rotor.

Fig. 3 next shows the time histories of the forces in the Cartesian x -direction for the case with no eccentricity and for the case with a static eccentricity of 10 % in the positive x -direction respectively. Furthermore, Fig. 4 shows the variations of the forces in the Cartesian x -direction over time for some different whirling frequencies. In addition, estimates of the spectrum contents for each of the force curves of Fig. 4 have been provided in Fig. 5. While the objective with the spectrum estimates is the identification of the frequency contents of the signals, the tonal components have been scaled as a one-sided RMS-scaled linear spectrum estimates using the Welch method [21]. This non-parametric estimate is given by

$$\hat{X}^{LS}(f_l) = \sqrt{\frac{2}{N_2 N_1 U} \sum_{n_2=0}^{N_2-1} \left| \sum_{n_1=0}^{N_1-1} x_l(n) w(n) e^{-j \frac{2\pi n l}{N_1}} \right|^2}, \quad f_l = \frac{l \cdot f_s}{N_1} \quad (5)$$

where N_1 is the length of one periodogram, N_2 is the number of periodograms, $l = 0, \dots, N_1/2$, f_l is the frequency at index l , f_s is the sampling frequency, $w(n)$ is the data window and

$$U = \frac{1}{N_1} \left(\sum_{n=0}^{N_1-1} w(n) \right)^2 \quad (6)$$

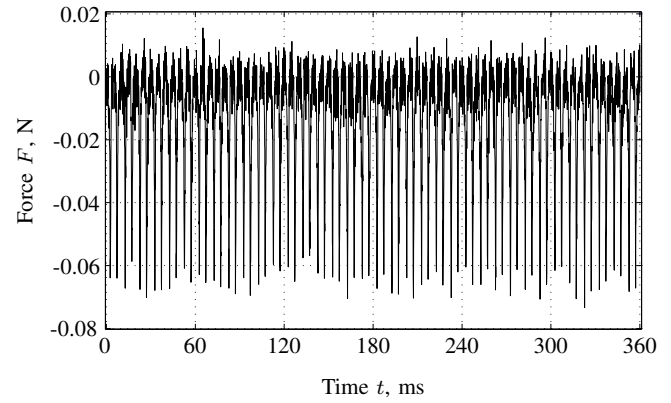
is the window-dependent resolution bandwidth normalisation factor [22] for power spectrum estimation. It is essential to note that the factor of 2 is not used in Equation (5) at index $l = 0$. The selected linear spectrum estimation parameters are shown in Table III. Next, Fig. 6 displays the steady state average UMP in the radial and tangential directions respectively over the whole span of the whirling range of six times the synchronous whirl speed both in the forward and in the backward whirls motion.

TABLE III. Linear spectrum estimation parameters in Equation (5)

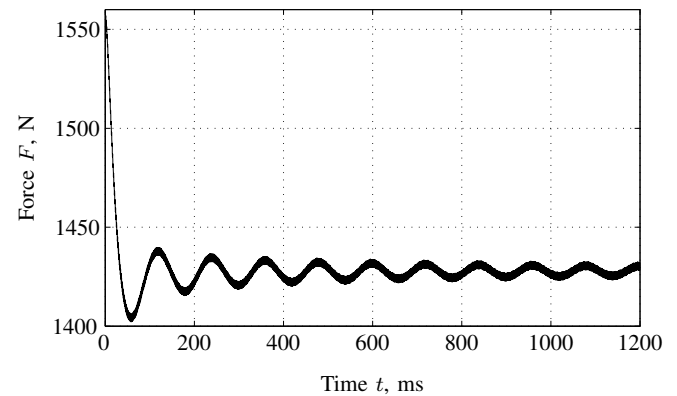
Parameter	Value or name
Data length (samples)	3 201
Sampling frequency, f_s [kHz]	10
Length of periodogram, N_1 (samples)	3 201
Time window, w	Flat top ¹
Number of periodograms, N_2	1

¹ This is the flattopwin window in MATLAB [23]

Two observations can be made from the results presented in this section. Firstly, Figs 4 and 5 show that the whirling frequency dictates the frequency of the force variations. For example, considering Fig. 4c



(a) No rotor-stator eccentricity

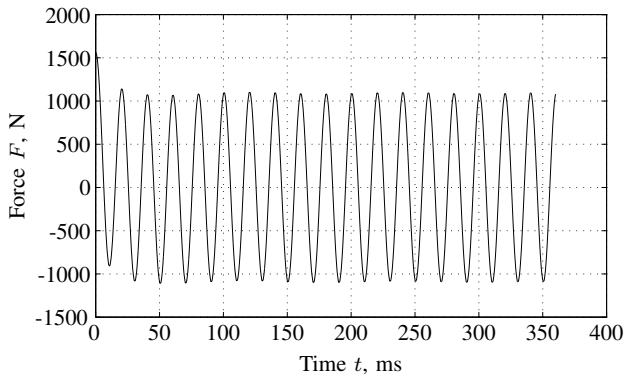


(b) Static eccentricity of 10 %

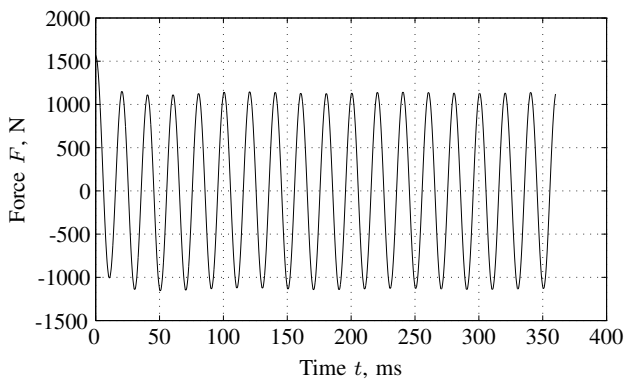
Fig. 3. Time histories of the forces acting on the rotor in the Cartesian x -direction. The result for no eccentricity is shown in Fig. 3a for three rotor revolutions whereas the result for a static eccentricity of 10 % eccentricity ratio of the mean air-gap length in the positive x -direction is shown in Fig. 3b over ten rotor revolutions. Fig. 3b shows that it takes a long simulation time for steady state condition in the force curve to be reached

for a case of whirling ratio $\omega_{whr} = -3.0$, the time period of the sinusoidal force variation is one third of the time for the case of synchronous whirling (not shown in this paper) which gives 40 ms (see also Table II and Section III-C). Secondly, Fig. 6 shows that the UMP components both in the radial and in the tangential directions do not have high magnitudes for the 10 % eccentricity ratio studied. The dampening effect of the damper windings is estimated to be a substantial amount of around 30 % in Fig. 6 for the radial UMP component at high whirling ratios of -6.0 and 6.0 in relative to the magnitude of the radial UMP component at synchronous whirl speed.

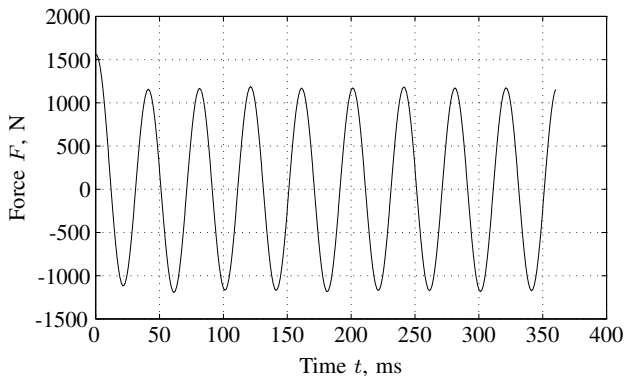
Of importance is to note that force measurements were carried out [14] and it has been reported that a static eccentricity in the x -direction of 24 % gives a horizontal force on the rotor of around 4 kN when no damper windings are present. A corresponding purely static simulation in MagNet [20] gave a comparable answer; This result is not shown in this article. We should however remark that a purely static eccentric rotor is almost impossible to achieve in practice unless both a static and dynamic balancing of the rotor have been properly carried out. No thorough information on the rotor balancing for the generator under study was available though. Besides, as in the case of a purely static eccentricity motion as given in Fig. 3b in the x -direction, the corresponding force curve and spectrum contents are expected to be similar in the Cartesian y -direction as well.



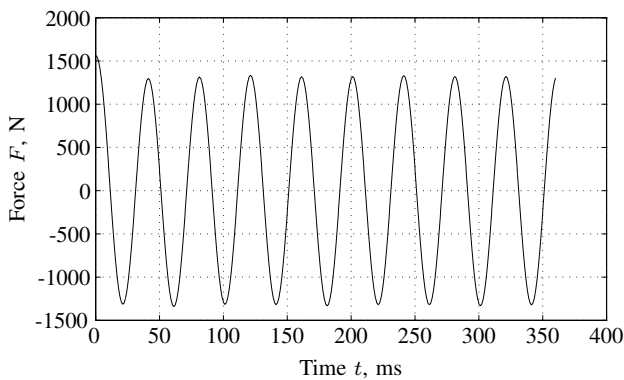
(a) Whirling ratio of -6.0



(b) Whirling ratio of 6.0

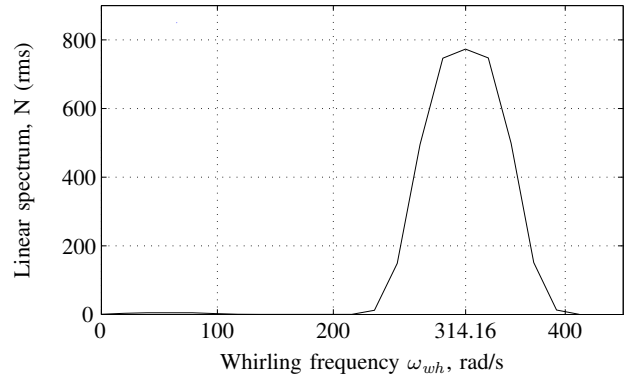


(c) Whirling ratio of -3.0

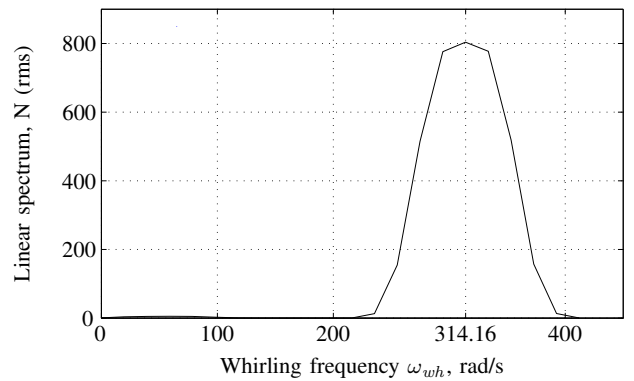


(d) Whirling ratio of 3.0

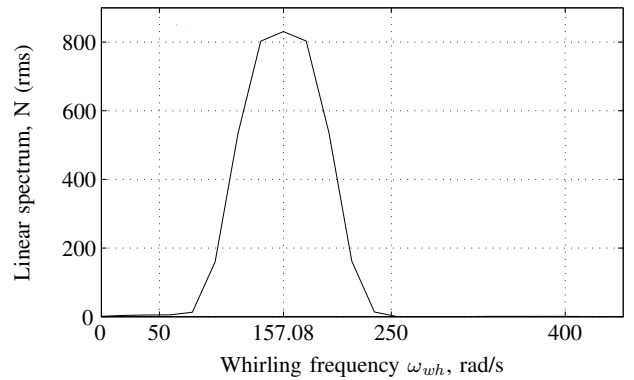
Fig. 4. Time histories of the forces acting on the rotor in the horizontal direction in the case of a purely dynamic eccentricity motion of the rotor of 10 % eccentricity ratio for different whirling ratios namely -6.0, 6.0, -3.0 and 3.0



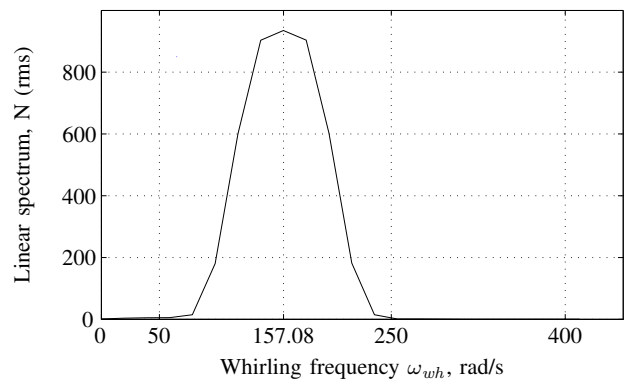
(a) Whirling ratio of -6.0



(b) Whirling ratio of 6.0

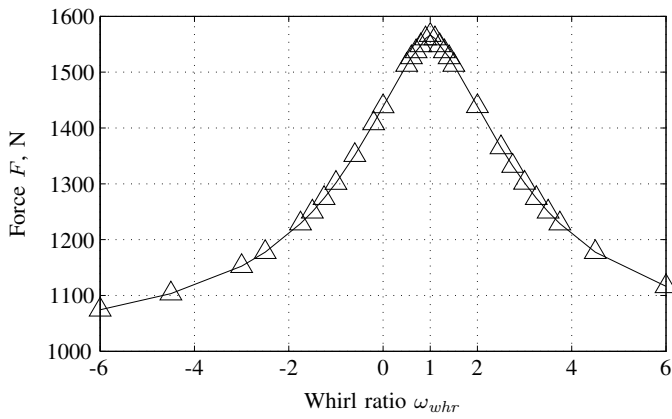


(c) Whirling ratio of -3.0

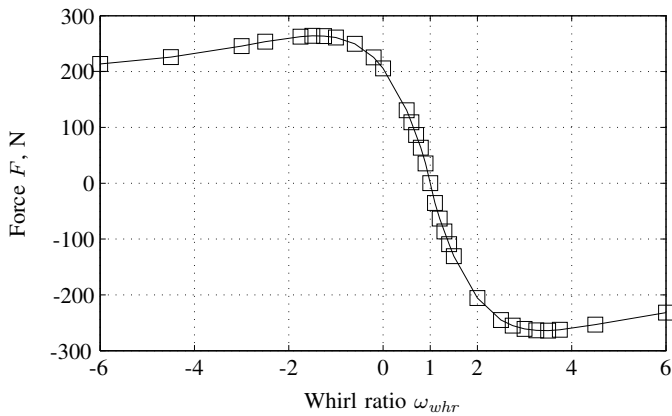


(d) Whirling ratio of 3.0

Fig. 5. One-sided linear spectrum estimates of the force time histories of Fig. 4 in the range 0 rad/s to 400 rad/s (see Table II) for different whirling ratios namely -6.0, 6.0, -3.0 and 3.0. The parameters used in the spectrum analysis are given in Table III. A whirl ratio of unity corresponds to a whirling frequency of 52.36 rad/s



(a) Radial force on the rotor



(b) Tangential force on the rotor

Fig. 6. Radial force and tangential force on the rotor with a purely dynamic eccentricity motion of 10 % eccentricity ratio. The transparent triangles and squares on the graphs depict the whirling frequencies used in the simulations expressed as whirl ratios and the corresponding force values are joined with straight lines. Synchronous whirl is marked on the graph as the point $\omega_{whr} = 1$

B. Flux density distribution and harmonics in the air-gap

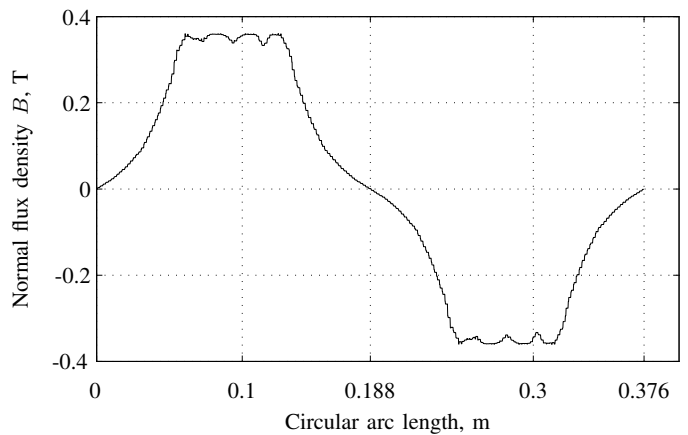
The flux density \mathbf{B} together with the currents flowing in the various parts of the generator, in principle, provide all the information from which any other EM parameter of interest can be derived. Current values and their interpretation are postponed to the next section and this section presents flux density information. A knowledge of \mathbf{B} provides, among other things, information on how much use of the iron is made in the generator and this indirectly tells us whether the size of the generator is right for its power output.

Figs 7 and 8 display the spatial variation of the flux density in the air-gap in the normal direction over two consecutive poles at the last time instant in the simulations for the different motion cases as considered in Section IV-A. The two consecutive poles which were chosen faced the smallest air-gap position. The arc length considered is at a radius of 359 mm (see Table I) which is well into an air-layer in the air-gap where force computations take place and the spatial circular arc length over two consecutive poles amounts to $2 \times 359 \text{ mm} \times \frac{\pi}{6} \approx 376 \text{ mm}$. A spatial resolution of 2048 points exists in Figs 7 and 8.

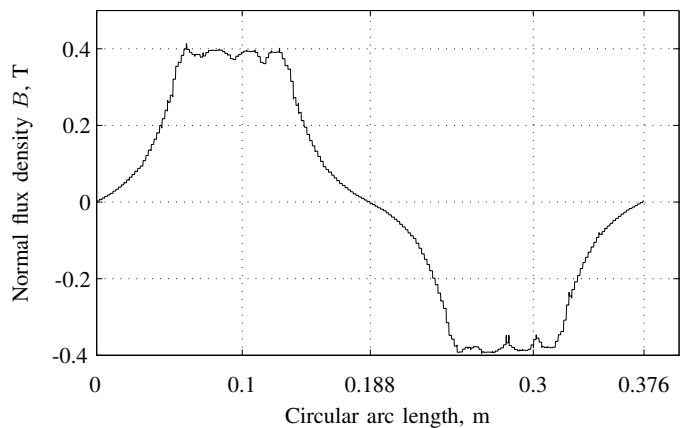
Figs 9 and 10 give the harmonic contents of the spatial variation of the flux density distributions of Figs 7 and 8 respectively. We are interested in the frequency contents in order to view what kinds of frequencies whirling can bring but the amplitude levels are amenable

to comparison as well since the latter are the absolute magnitude values from the Fourier Transform results of the spatial variation of the flux densities. The amplitudes of the peaks in the Fourier Transform estimates have been normalised with the sampling wavenumber which is around 5444.96 m^{-1} .

It is immediately obvious from the flux density estimates in Figs 7 and 8 that the eccentricity we are considering can be small in addition to the generator having perhaps not a small air-gap in relation with the diameters of the rotor and that of the stator (see Table I), and this is causing the flux density behaviours to be practically the same even at very high whirling ratios. In the simulations a maximum value of $B \leq 0.4 \text{ T}$ was noted in all cases and this also explains the relatively low force magnitudes as seen in Section IV-A. At this flux density value, we are perhaps not making use of the whole iron available to us in the generator. This situation can nevertheless be different with a higher eccentricity ratio value.



(a) No rotor-stator eccentricity



(b) Static eccentricity of 10 %

Fig. 7. Spatial distribution of the normal flux density in the air-gap over a pole pair for the case of no rotor stator eccentricity in Fig. 7a and for the case with a purely static eccentricity ratio of 10 % of the mean air-gap length in the positive x -direction in Fig. 7b. A circular length of around 188 mm subtends an angle of 30° mechanical for one pole pitch

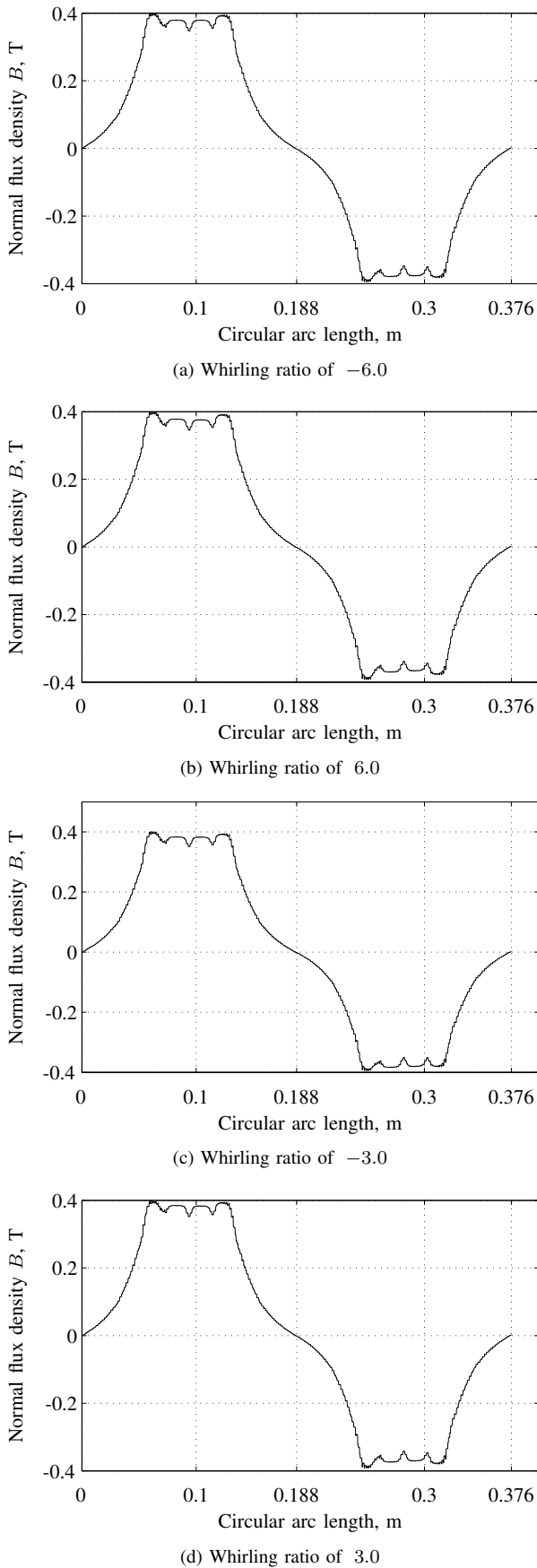


Fig. 8. Spatial distribution of the normal flux density in the air-gap over a pole pair for different whirling ratios namely -6.0, 6.0, -3.0 and 3.0. The motion type is a purely dynamic eccentric motion of the rotor of 10 % eccentricity ratio of the mean air-gap length. A circular length of around 188 mm subtends an angle of 30° mechanical for one pole pitch

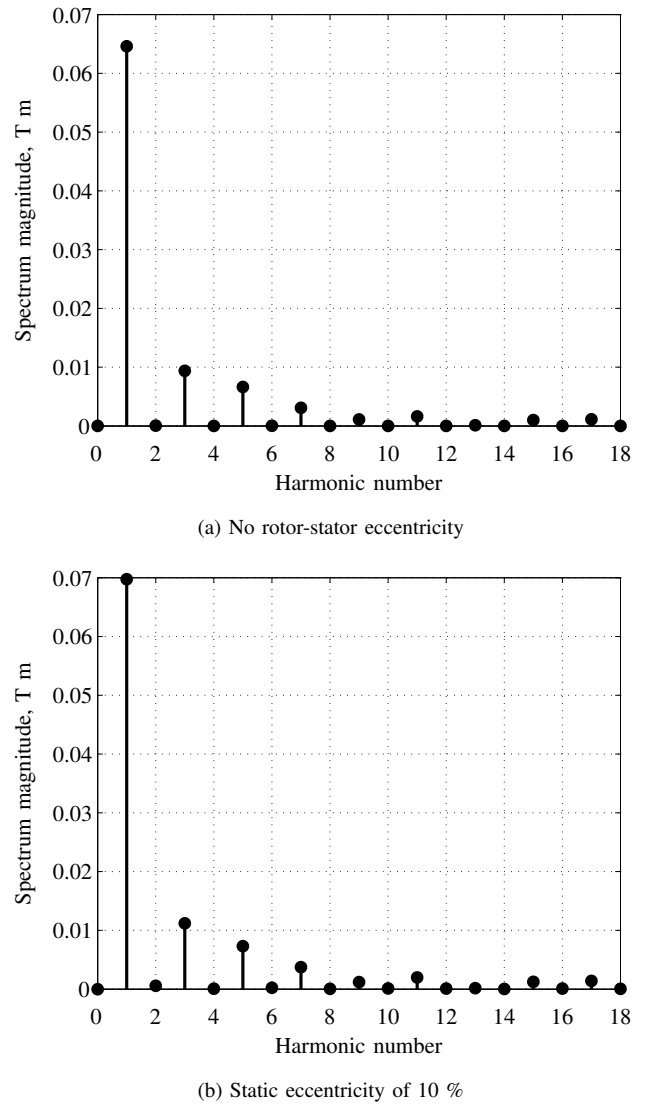


Fig. 9. Flux density spatial spectrum estimates stem plots as a function of harmonic number showing the first eighteen harmonics for the case of no rotor stator eccentricity in Fig. 9a and for the case with a purely static eccentricity ratio of 10 % of the mean air-gap length in the x -direction in Fig. 9b. The amplitudes of the spectrum estimates represent absolute magnitude values from the Fourier Transform computation that have been scaled down by the sampling wavenumber. Refer also to Fig. 7 for the flux density spatial variation

C. Maximum currents in the damper bars and in the rotor rim

Induced currents, whether desirable or undesirable, exist in any generator. Damper bars allow the flow of currents in order to minimise oscillations of the rotor and this is a desirable feature. On the other hand, induced currents flow for example in the solid rotor rim on which the poles lie and this is undesirable. While the solid rotor rim and the solid spider on which the former is fixed have been modelled with the same electrical resistivity value, only the conducting rotor rim will be considered here as the eddy currents affect the solid rim considerably more than the solid spider since the latter is much further away from the poles (see also Fig. 2). The pole shoes and the stator materials are laminated and hence do not have induced currents.

The roles and importance of the damper bars have been documented in the literature [1], [24]. For an alternator standing alone, pole slipping is not an issue and as mentioned in Section III-C, the rotor speed ω_{ro} is kept at its synchronous value (see Table I) irrespective

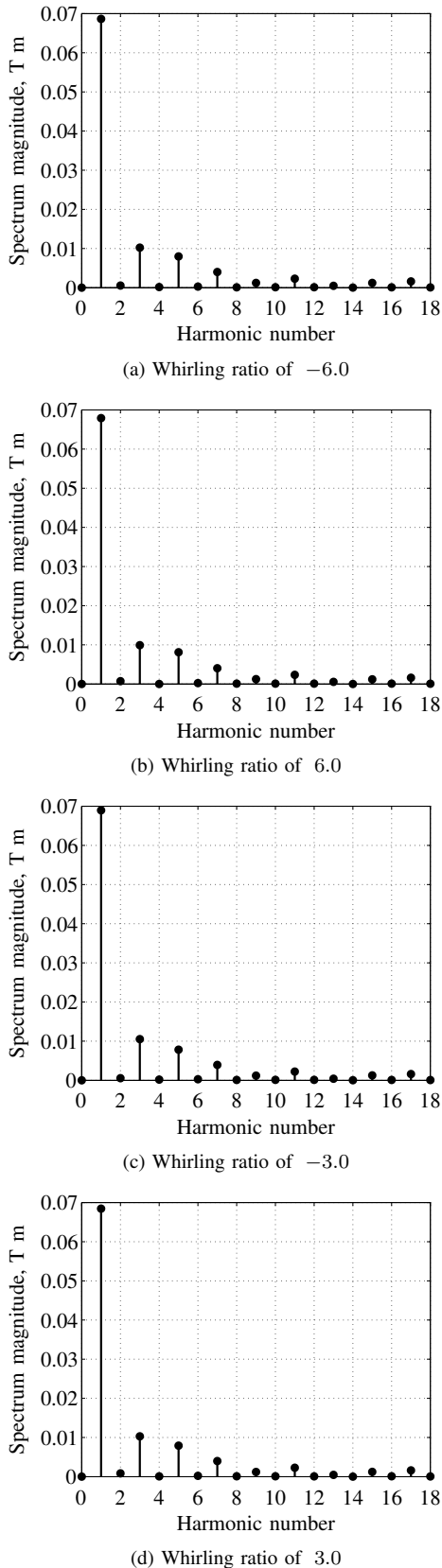


Fig. 10. Flux density spatial spectrum estimates stem plots as a function of harmonic number for different whirling ratios namely -6.0, 6.0, -3.0 and 3.0 showing the first eighteen harmonics. The motion type is a purely dynamic eccentric motion of the rotor of 10 % eccentricity ratio of the mean air-gap length. The amplitudes of the spectrum estimates represent absolute magnitude values from the Fourier Transform computation that have been scaled down by the sampling wavenumber. Refer also to Fig. 8 for the flux density spatial variation

of the whirling speed ω_{wh} used in Table II. The problem of having a high current flow can be immediately linked to heat dissipation in the machine, depending also on the resistivity of the material. It is to be noted that vents and cooling ducts were not modelled in the EM analysis since these geometric features will only require finer mesh densities in the finite element analysis, which would increase the solver time. The electrical resistivities of the conducting rim and those of the damper bars were 5×10^{-7} ohm-m and 2.092×10^{-8} ohm-m respectively.

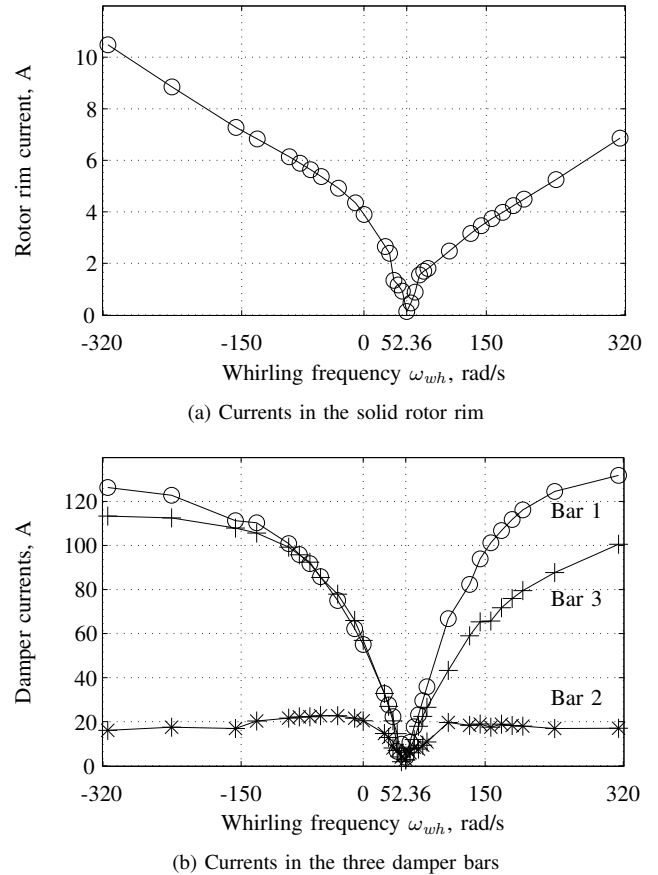


Fig. 11. Fig. 11a shows the maximum induced current flowing into the solid rotor rim while Fig. 11b presents the maximum damper currents flowing in the damper bars. The currents are for one pole only and the pole chosen is the one that adjoins the minimum air-gap length. The range of whirling frequencies considered is in the whirling ratio range of -6.0 to 6.0. Synchronous whirl is marked on the graph as the point $\omega_{wh} = 52.36$ rad/s (see also Table II). The arrangement of the damper bars, Bars 1 to 3, is according to the schematic shown in Fig. 2. The case for static eccentricity of 10 % can be read from the plots at the value $\omega_{wh} = 0$ rad/s

Fig. 11 presents the maximum currents flowing in the damper bars and in the rotor rim for one pole that adjoins the minimum air-gap length. The currents' variations have tonal components, and Fig. 11a and 11b shows the peak values of these sinusoidal time series. Visual inspection of Fig. 11 reveals that the currents can increase to very high levels (see Fig. 11b) when there is rotor whirling, be it in the forward or in the reverse whirl direction. A high current level can break down the insulation surrounding the damper bar. It is to be noted that in the simulations, information pertaining to the insulation type and material was not available. The level of currents in the rotor rim is not high and this can be attributed to the fact that the rim is recessed away from the air-gap. Besides, we can note that forward synchronous whirling at $\omega_{wh} = 52.36$ rad/s produces the least current flow and this whirling case is more common in hydropower

generators. Synchronous (forward) whirling can be associated to a stable operating condition of a hydropower generator as was seen in an earlier work by two of the authors [13].

On a machine without rotor eccentricity, it has been found that a current of about 0.02 A and currents of around 1 A were flowing in the solid rotor rim and damper bars respectively. These low currents are expected in a machine with perfectly centred rotor and stator. This provides a useful check for the EM models used in the simulations. It is thought that the centre damper bar has the smallest current produced by the whirling due to the fact that the outer damper bars (see Fig. 11b) act as shields [19].

D. Ohmic losses in the rotor rim

In solid materials, power losses are dissipated. In the model, only a few parts are electrically conducting and the stator material together with the pole shoes material are modelled with zero electrical conductivity. Since the poles sit outside on the rim, the magnetic diffusion of the magnetic field into the rim is small with a low value of the flux density and ohmic losses appear almost instantaneously at switch-on time without any considerable magnetic diffusion time. Ohmic losses in the damper bars and in the rotor rim are expected to have the same behaviours as in Fig. 11 from Section IV-C. In MagNet [20], the ohmic loss calculations for solid conductors neglect the hysteresis loss component. Table IV presents time average ohmic losses due to the eddy currents for some whirling cases as considered in this paper.

TABLE IV. Time average ohmic losses in the complete rotor rim structure for different whirling frequencies in the purely dynamic eccentricity motion cases

Whirling ratio	Whirling speed [rad/s]	Ohmic loss, [W]
-6.0	-314.16	27.828
-3.0	-157.08	10.908
3.0	157.08	3.720
6.0	314.16	15.672

Backward whirling is seen to produce considerably higher eddy current losses in the rotor rim than the corresponding forward whirling speeds do. It is also noted that the ohmic losses are very low. Low flux density values as observed in Section IV-B together with the outwards geometric configuration of the rotor poles (see Fig. 2) are the causes for such low ohmic losses. As expected, the ohmic losses are practically nil for the case without any eccentricity with a loss value of about 0.08 W (not included in the results of Table IV).

V. CONCLUSIONS

This paper aimed at bridging the gap between what electrical engineers usually want from EM simulations and what mechanical engineers would like to see. In this respect, whirling dependent behaviours of the rotor motion for a purely static eccentricity case and for a purely dynamic eccentricity case have been studied. The effects of whirling from a mechanical point of view were earlier treated by two of the authors [12], [13]. The present article serves to illustrate the importance of whirling but from an electrical engineering perspective. A hydropower machine is complex to model as there are so many variables that come into play and any artificial schism between the two above-mentioned engineering fields can only be eliminated when the generator is not viewed as an isolated item but instead as one which is under the influence of other parts in motion in a hydropower machine. MagNet [20], by being a general purpose FEM-based EM field modelling software product, allows a body to have several degrees of freedom and hence this advantage was taken of when building the necessary models in this paper.

Perhaps due to the large air-gap length that is providing high reluctance in the magnetic circuit, the results presented in this paper tend to have low order of magnitudes and no drastic changes in the force or in the flux density magnitudes for instance have been noted in the simulations. Higher eccentricity values other than the studied 10 % were not considered as they do not occur in a generator when under normal operating conditions. It has also been seen (see Fig. 6) that the effect of the damper bars become pronounced on the force magnitudes at large whirling ratios. In addition, it has been found that backward whirling tends to induce higher eddy currents than forward whirling does. The very low ohmic losses in the rotor rim also represent a key finding in this paper. A no-load model is considered sufficient though it can be argued that the (radial) UMP magnitudes may decrease when there is load. That said, the objective of this paper was not to compare the effect of a loaded versus an unloaded generator but to see how whirling affects important EM parameters that are normally used by electrical engineers.

A new contribution to the field of EM analysis of hydropower generators is the treatment of non-synchronous whirling in this paper and demonstration of its effect(s) on some EM parameters. This new addition has been combined with common eccentricity types that are reported in the literature.

ACKNOWLEDGMENTS

This project has been sponsored by Svenskt VattenkraftCentrum (SVC) in Sweden. The main author wishes to express his sincere thanks to the MagNet's Support team at Infolytica Europe. Information regarding the generator has been supplied by Dr Urban Lundin from Uppsala Universitet, Sweden.

REFERENCES

- [1] M. Walker. *Specification and Design of Dynamo-Electric Machinery*. Longmans' Electrical Engineering Series, 1915.
- [2] E. Rosenberg. Magnetic pull in electrical machines. *Transactions of the American Institute of Electrical Engineers*, 37(2):1425–1469, 1918.
- [3] I. Ozelgin. Analysis of magnetic flux density for airgap eccentricity and bearing faults. *International Journal of Systems Applications, Engineering & Development*, 4(2):162–169, 2008.
- [4] D. de Canha, W.A. Cronje, A.S. Meyer, and S.J. Hoffe. Methods for diagnosing static eccentricity in a synchronous 2 pole generator. In *Power Tech, IEEE, Lausanne*, pages 2162–2167, July 2007.
- [5] I. Tabatabaei, J. Faiz, H. Lesani, and M.T. Nabavi-Razavi. Modeling and simulation of a salient-pole synchronous generator with dynamic eccentricity using modified winding function theory. *IEEE Transactions on Magnetics*, 40(3):1550–1555, May 2004.
- [6] G. Joksimovic and C. Bruzzese. Static eccentricity detection in synchronous generators by field current and stator voltage signature analysis—Part I: Theory. In *Electrical Machines (ICEM), XIX International Conference. 6–8 September, Rome, Italy*, pages 1–6, 2010.
- [7] B.A.T. Iamamura, Y. Le Menach, A. Tounzi, N. Sadowski, and E. Guillot. Study of static and dynamic eccentricities of a synchronous generator using 3-D FEM. *IEEE Transactions on Magnetics*, 46(8):3516–3519, August 2010.
- [8] J. Faiz, M. Babaei, J. Nazarzadeh, B.M. Ebrahimi, and S. Amini. Time-stepping finite-element analysis of dynamic eccentricity fault in a three-phase salient pole synchronous generator. *Progress in Electromagnetics Research B*, 20:263–284, 2010.
- [9] T.P. Holopainen, A. Tenhunen, E. Lantto, and A. Arkkio. Unbalanced magnetic pull induced by arbitrary eccentric motion of cage rotor in transient operation. Part 1: Analytical model. *Electrical Engineering*, 88(1):13–24, April 2005.
- [10] T.P. Holopainen, A. Tenhunen, E. Lantto, and A. Arkkio. Unbalanced magnetic pull induced by arbitrary eccentric motion of cage rotor in transient operation. Part 2: Verification and numerical parameter estimation. *Electrical Engineering*, 88(1):25–34, March 2005.
- [11] N.L.P. Lundström and J.-O. Aidanpää. Whirling frequencies and amplitudes due to deviations of generator shape. *International Journal of Non-Linear Mechanics*, 43(9):933–940, November 2008.
- [12] Y. Calleecharan and J.-O. Aidanpää. Dynamics of an hydropower generator subjected to unbalanced magnetic pull. *Proceedings of the Institution of Mechanical Engineers, Part C: Journal of Mechanical Engineering Science*, 225(9):2076–2088, 2011.

- [13] Y. Calleecharan and J.-O. Aidanpää. Stability analysis of an hydropower generator subjected to unbalanced magnetic pull. *IET Sci. Meas. Technol.*, 5(6):231–243, November 2011.
- [14] Division for Electricity, The Ångström Laboratory, Uppsala Universitet, Sweden.
- [15] H. Torkaman and E. Afjei. Magnetostatic field analysis regarding the effects of dynamic eccentricity in switched reluctance motor. *Progress in Electromagnetics Research M*, 8:163–180, 2009.
- [16] O. Biro. Computational Electromagnetics (CEM) Conference 2011—Review of Eddy current analysis. [online]. <http://tv.theiet.org/technology/electronics/10890.cfm>.
- [17] D. Marcsa and M. Kuczmann. Finite element analysis of single-phase induction motors. COMSOL Conference, Budapest, Hungary November 24, pp. 1–6, 2008.
- [18] M.V.K. Chari and P. Silvester. Analysis of turboalternator magnetic fields by finite elements. *IEEE Transactions on Power Apparatus and Systems*, PAS-90(2):454–464, March 1971.
- [19] J.R. Brauer. *Magnetic Actuators and Sensors*. Wiley-IEEE Press, 1st edition, February 2006.
- [20] MagNet, Infolytica Corporation, Montréal, Québec, Canada, 2011, Version 7.1.3.
- [21] W.A. Gardner. *Statistical Spectral Analysis: A Non-Probabilistic Theory*. Prentice Hall, January 1988.
- [22] F. Harris. On the use of windows for harmonic analysis with the discrete Fourier transform. In *Proc. of the IEEE*, volume 66, pages 51–83, 1978.
- [23] MATLAB, The MathWorks Inc., Natick, Massachusetts, USA, 2012, Version 7.14.0.739 (R2012a).
- [24] E.W. Kimbark. *Power System Stability Volume III: Synchronous Machines*, IEEE Press Series on Power Engineering. Piscataway, NJ (Wiley IEEE Press, New York), February 1995.

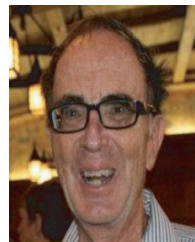
BIOGRAPHIES



Yogeshwarsing Calleecharan received the B.Eng. degree in Mechanical Engineering from the University of Mauritius, Mauritius, in 2000, the M.Sc. degree in Mechanical Engineering from Blekinge Tekniska Högskola, Sweden, in 2003, and the Ph.D. degree in Solid Mechanics from Luleå Tekniska Universitet, Sweden, in 2013. Since 2014 he is a lecturer with the Mechanical and Production Engineering Department, University of Mauritius, Mauritius. His research interests include electromechanics, vibrations and signal analysis, and software development with the Ada programming language.



Jan-Olov Aidanpää received the M.S. degree in Mechanical Engineering from Luleå Tekniska Universitet (LTU), Sweden, in 1987, and the Ph.D. degree in Solid Mechanics from LTU in 1995. Since 2013 he is working as Chair Professor in Computer Aided Design at Luleå Tekniska Universitet, Sweden. His research interest is within non-linear rotor dynamics where he develops measuring techniques and models of hydro and wind power systems.



John R. Brauer earned a bachelor's degree from Marquette University, USA, and master's and Ph.D. degrees from the University of Wisconsin-Madison, USA, all in electrical engineering. He performed engineering research for A. O. Smith Corporation, MSC Software, and Ansoft Corporation, specializing in finite element analysis of electromagnetic devices. He has been Adjunct Professor at Milwaukee School of Engineering, USA, since 1998, and has served as an officer in several professional associations, including the IEEE, where he is a Life Fellow. His publications include over 160 papers and several books. His most recent book is *Magnetic Actuators and Sensors*, 2nd edition, published in 2014 by Wiley IEEE Press.

A New Sorting Algorithm with filling to the left and right

N. Vasilev and A. Bosakova-Ardenska

Abstract— This paper presents an algorithm for sorting by using of LIT (left inversions table). The algorithm is named LR. The time complexity of the proposed algorithm analytically evaluated. Two approaches for acceleration of LR are presented. The proposed algorithm and its two improvements are implemented in C++. Experimental comparisons are done between LR and some known algorithms, and between LR and its two modifications. The experiments show that LR is faster than “bubble sort” and “LtoRA” algorithms but it is slower than the algorithms “insertion sort” and “selection sort”. The experiments also show that for rows in which there is a large number of the repetitions, the modification “LR – repeat” is faster than the original algorithm, “Bubble sort”, “Selection sort” and the modification “LRA – minimax”. The algorithm “LR minimax” is faster than algorithm LR in all cases (when the row has large or small number of repetitions).

Index Terms— Sorting algorithm, Left Inversions Table, Insertion sort, Selection sort

I. INTRODUCTION AND AIMS

THIS paper is a continuation of the work in article [7]. The two papers are part of a research on some sorting methods and the possibility for their improvement. It is considered that near 25% of the work of the computer systems is used for sorting of information [1]. This shows how important it is to find good sorting methods and algorithms. There are many methods and algorithms for sorting and they are studied widely [1,2,3,4,5,6]. This doesn't mean that everything in this area is finished and nothing new and better could be found, especially considering the characteristics of the given row.

The aim of this paper is:

- to propose and investigate a method for sorting of rows by a left inversions table (LIT) with left and right filling which is an improvement of the sorting methods proposed in [7];
- to evaluate the complexity of the proposed method;
- to make a program for the proposed method (algorithm) for row sorting by LIT with right and left filling;

Naiden Borisov Vasilev was head of department of Computer Systems and Technologies in Technical University Sofia, branch in Plovdiv, Bulgaria. (e-mail: mnavasilev@yahoo.com).

Atanaska Dimitrova Bosakova-Ardenska works in University of Food Technologies, Plovdiv in Bulgaria. She is associated professor in department of Computer Systems and Technologies (e-mail: a_bosakova@uft-plovdiv.bg).

- to evaluate and compare experimentally the proposed method: sorting by LIT with right and left filling.

The methods for row sorting considered in [7] are:

- sorting by LIT with filling from left to right;
- sorting by LIT with filling from right to left.

They are based on the proven assertion: the table of the left inversions by positions of a given row a_j ($j = 1, 2, \dots, n$) uniquely defines the sorted ascending or descending row.

LIT of a given row is the sequence of numbers in the j -th position in which the number of the elements d_j is written, left from a_j (j -th element, $j = 1, 2, \dots, n$) and larger than it.

The steps for sorting by LIT are the following:

- 1) constructing the LIT of the given row by counting the larger elements from the left of every element in the row;
- 2) constructing the searching row.

Constructing the searching row begins with the element in the first position of the given row, continues with the second element and so on, until the element in the n -th position. The position for recording of the elements and the number of moved elements depending on the desired sorting, and the direction of moving are shown in Table 1.

TABLE 1. POSITION FOR RECORD OF a_j , $j = 1, 2, \dots, n$, AND NUMBER OF MOVED ELEMENTS FOR SORTING WITH FILLING FROM LEFT TO RIGHT AND FROM RIGHT TO LEFT

Filling	Position for record of a_j		Number of the moved elements	
	Row		Row	
	Ascending	Descending	Ascending	Descending
To the right	$j - d_j$	$d_j + 1$	d_j	$j - d_j - 1$
To the left	$n - d_j$	$n - (j - d_j) + 1$	$j - d_j - 1$	d_j

TABLE 2. TABLE OF LEFT INVERSIONS OF THE GIVEN ROW

Position j in the given row	1	2	3	4	5	6	7	8	9
Value of the element a_j	60	40	70	20	50	30	10	90	80
d_j – num. of the elements from the left bigger than a_j	0	1	0	3	2	4	6	0	1

$p_j = L+d_j$ when $d_j \leq j-d_j-1$ and $p_j = R-(j-d_j-1)$ when $d_j > j-d_j-1$ for descending row.

We will construct the ascending row of the row in the example above.

- $j=1$; the first element a_1 is written in position $p_1 = n = 9$.
- $j=2$; $L=8, R=10$; $d_2 = 1 > 2-1-1 = 0 = 2-d_2-1$; a_2 is written to the left; $p_2 = 8+2-1 = 8$.
- $j=3$; $L=7, R=10$; $d_3 = 0 < 3-0-1 = 2 = 3-d_3-1$; a_3 is written to the right; $p_3 = 10-0 = 10$.
- $j=4$; $L=7, R=11$; $d_4 = 3 > 4-3-1 = 0 = 4-d_4-1$; a_4 is written to the left; $p_4 = 7+4-3-1 = 7$.
- $j=5$; $L=6, R=11$; $d_5 = 2 = 5-2-1 = 2 = 5-d_5-1$; a_5 is written to the right; $p_5 = 11-2 = 9$.

The elements with indices 1 (60) and 3 (70) are moved to the right. They are written in positions 10 and 11.

$j=6$; $L=6, R=12$; $d_6 = 4 > 6-4-1 = 1 = 6-d_6-1$; a_6 is written to the left; $p_6 = 6+6-4-1 = 7$.

The element with index 4 (20) is moved to the left. It is written in position 6.

$j=7$; $L=5, R=12$; $d_7 = 6 > 7-6-1 = 0 = 7-d_7-1$; a_7 is written to the left; $p_7 = 5+7-6-1 = 5$.

$j=8$; $L=4, R=12$; $d_8 = 0 < 8-0-1 = 7 = 8-d_8-1$; a_8 is written to the right; $p_8 = 12-0 = 12$.

$j=9$; $L=4, R=13$; $d_9 = 1 < 9-1-1 = 7 = 9-d_9-1$; a_9 is written to the right; $p_9 = 13-1 = 12$.

The element with index 8 is moved to the right. It is written in position 13.

Figures 2a and 2b present the construction of the ascending and the descending rows sorted by LIT with filling to the left and right. The moved elements are underlined.

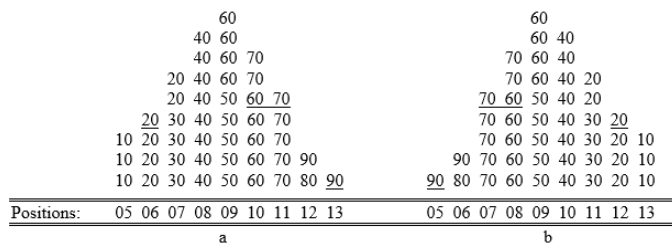


Fig.2. Ascending (a) and descending (b) orders of the given row sorted by LIT with filling to the left and right

We will note that:

- if $d_j = 0$, a_j is written to the right after the last element in the row;
- if $d_j = j-1$, a_j is written to the left before the first element in the row.

In both cases, moves of elements are not executed. The number of the moves for constructing the ascending and the descending rows is the same and its value is 4. The results are summarized in Table 3.

TABLE 3. POSITIONS FOR RECORDING AND DIRECTION OF FILLING BY SORTING TO THE LEFT AND RIGHT

Row	Direction of filling		Position for record of a_j	
	$d_j \leq j-d_j-1$	$d_j > j-d_j-1$	$d_j \leq j-d_j-1$	$d_j > j-d_j-1$
Asc.	To the right	To the left	$R-d_j$	$L+j-d_j-1$
Desc.	To the left	To the right	$L+d_j$	$R-(j-d_j-1)$

IV. EVALUATION OF THE COMPLEXITY OF THE ALGORITHM FOR SORTING BY LIT WITH FILLING TO THE LEFT AND RIGHT

The operations which are used in the proposed algorithm are:

- 1) compare for constructing of the LIT (for counting of the larger elements); the elements of the array are compared;
- 2) record (increment) for counting of the larger elements;
- 3) compare to determine the direction of the minimal move (left or right); the first operand is number and the second one is an expression which contains subtraction (see table 3);
- 4) record (move one position to the left or to the right) of the elements of the array to construct the current sorted row;
- 5) record (move) of the elements in temporary positions in the array for constructing the current sorted row; the record position is a result of addition/subtraction (see table 3);
- 6) record (increment) of nearest vacant left (L) and right (R) positions in the array for sorted row.

Number of the compares for count the bigger elements (left inversions) by position is:

$$C = n(n-1)/2.$$

Number of the records (increments) by counting the bigger elements is:

$$R_{lr} = \sum_{j=1}^n d_j.$$

His values [7] are:

- minimal- 0 (the row is ascending);
- average- $n(n-1)/4$;
- maximal- $n(n-1)/2$ (the row is descending).

The number of compares to determine the direction of minimal move (left or right) is equal to $n-1$.

The number of records (moves one position to left or right) is:

$$S_{lr} = \sum_{j=1}^n \min(d_j, j - d_j - 1)$$

The minimal number of the moves is 0. For rows which has $d_j = 0$ or $j-1$, $j = 1, 2, \dots, n$, operations move aren't done. Every such row can be divided (from left to right) in two rows: one increasing row and one decreasing row like the smallest element in the increasing row is bigger than the biggest element in the decreasing row. Ascending and descending rows are such rows. When sort increasing row the fill up are to the right only. When sort decreasing row the fill up are to the left only. The number of these rows is 2^{n-1} . For $n=4$, the number of these rows is $2^{4-1}=8$. These rows have LIT: 0000, 0100, 0020, 0003, 0120, 0103, 0023 and 0123. (See table 4.)

The maximal number of the moves is: $(n^2-2n)/4$ when n is even and $(n^2-2n+1)/4$ when n is odd. This value is obtained when the LIT are: 0, 0 or 1, 1, 1 or 2, 2, 2 or 3,..., $n/2-1$, $n/2-1$ or $n/2$ if n is even and 0, 0 or 1, 1, 1 or 2, 2, 2 or 3,..., $(n-1)/2-1$ or $(n-1)/2$, $(n-1)/2$ if n is odd. The number of these rows is $2^{n/2}$ if n is even and $2^{(n-1)/2}$ if n is odd. When $n = 4$, the number of these rows is 4. The LIT of these rows are: 0011, 0012, 0111 and 0112. The maximal number of the moves is 2. (See table 4.)

The number of records (moves) of the elements in temporary positions in the array for constructing of the current sorted row is always n (a new array).

The number of records (increments) of the nearest left (L) vacant position and nearest right (R) vacant position in the array is n .

We note that the number of the operations (including the moves) for constructing the ascending and the descending row is the same.

The time for constructing the sorted row with filling to the left and right will be:

$$T_{lr} = t_{11}n(n-1)/2 + t_{21} \sum_{j=1}^n d_j + t_{12}(n-1) + t_{22} \sum_{j=1}^n \min(d_j, j - d_j - 1) + t_{23}n + t_{21}n$$

t_{11} is the time for comparing two elements of the array;

t_{21} is the time for incrementing and recording;

t_{12} is the time for comparing with the first operand being an number, and the second one being a value of the operation subtraction;

t_{22} is the time for recording (moving to the left or right) of a element of the array;

t_{23} is the time for additions/subtractions and recording of the result.

The minimal and maximal time for constructing the sorted row by LIT with filling to the left and right will be:

$$T_{lr_min} = t_{11}n(n-1)/2 + t_{12}(n-1) + t_{23}n + t_{21}n = K$$

$$T_{lr_max} = K + \max(t_{21}n(n-1)/2, t_{21}n^2/4 + t_{22}(n^2 - 2n)/4)$$

$$T_{lr_max} = K + \max(t_{21}n(n-1)/2, t_{21}(n^2 - 1)/4 + t_{22}(n^2 - 2n + 1)/4)$$

The first expression for T_{lr_max} is for n even and the second expression is for n odd.

$n^2/4$ is maximal number of recordings (increments) for the rows with maximal number of moves for n even. $(n^2 - 1)/4$ is maximal number of recordings (increments) for the rows with maximal number of moves for n odd.

The time T_{lr_min} is for the ascending row.

The time T_{lr_max} is for the rows with LIT: 0, 1, 1, 2, 2, 3, ..., $n/2-1$, $n/2-1$, $n/2$ when n is even and 0, 1, 1, 2, 2, 3, ..., $(n-1)/2-1$, $(n-1)/2-1$, $(n-1)/2$, $(n-1)/2$ when n is odd or for the descending row.

The number of operations in the second operand of the addend "max" is equal to the number of operations in the first operand: $n(n-1)/2$. So, the value of max will be determined by the ratio of the values of t_{21} and t_{22} .

Table 4 shows the relationship between operations "move" in the discussed methods for sorting for $n = 4$.

The first column contains all rows (permutations) of the elements of the set $\{1, 2, 3, 4\}$.

In the second column the tables of the left inversions (LIT) for every row are constructed.

In each cell of the third column the moves to the right are sequentially written and summed for the first, second, third and fourth elements of the row (in the cell of the first column) for constructing the ascending row with filling to the right. It can be seen that the numbers (digits) in the second and third column are the same.

In each cell of the fourth column the moves to the left are sequentially written and summed for the first, second, third and fourth elements of the row (in the cell of the first column) for constructing the ascending row with filling to the left. It is seen that the sum of the corresponding digits in the third and fourth columns is equal to the position number of digits minus one.

TABLE 4. MOVES IN THE THREE METHODS FOR SORTING BY LIT FOR N=4.

Row (n=4)	LIT	Moves		
		To the right	To the left	Left and right
1234	0000	0+0+0+0=0	0+1+2+3=6	0+0+0+0=0
1243	0001	0+0+0+1=1	0+1+2+2=5	0+0+0+1=1
1342	0002	0+0+0+2=2	0+1+2+1=4	0+0+0+1=1
2341	0003	0+0+0+3=3	0+1+2+0=3	0+0+0+0=0
1324	0010	0+0+1+0=1	0+1+1+3=5	0+0+1+0=1
1423	0011	0+0+1+1=2	0+1+1+2=4	0+0+1+1=2
1432	0012	0+0+1+2=3	0+1+1+1=3	0+0+1+1=2
2431	0013	0+0+1+3=4	0+1+1+0=2	0+0+1+0=1
2314	0020	0+0+2+0=2	0+1+0+3=4	0+0+0+0=0
2413	0021	0+0+2+1=3	0+1+0+2=3	0+0+0+1=1
3412	0022	0+0+2+2=4	0+1+0+1=2	0+0+0+1=1
3421	0023	0+0+2+3=5	0+1+0+0=1	0+0+0+0=0
2134	0100	0+1+0+0=1	0+0+2+3=5	0+0+0+0=0
2143	0101	0+1+0+1=2	0+0+2+2=4	0+0+0+1=1
3142	0102	0+1+0+2=3	0+0+2+1=3	0+0+0+1=1
3241	0103	0+1+0+3=4	0+0+2+0=2	0+0+0+0=0
3124	0110	0+1+1+0=2	0+0+1+3=4	0+0+1+0=1
4123	0111	0+1+1+1=3	0+0+1+2=3	0+0+1+1=2
4132	0112	0+1+1+2=4	0+0+1+1=2	0+0+1+1=2
4231	0113	0+1+1+3=5	0+0+1+0=1	0+0+1+0=1
3214	0120	0+1+2+0=3	0+0+0+3=3	0+0+0+0=0
4213	0121	0+1+2+1=4	0+0+0+2=2	0+0+0+1=1
4312	0122	0+1+2+2=5	0+0+0+1=1	0+0+0+1=1
4321	0123	0+1+2+3=6	0+0+0+0=0	0+0+0+0=0

In each cell of the fifth column the moves to the left and right are sequentially written and summed for the first, second, third and fourth elements of the row (in the cell of the first column) for constructing the ascending row with filling to the left and right. It is seen that the value of each digit is equal to the value of the smaller of the corresponding digits in the third and fourth columns. The smaller digit determines the direction of the filling.

The maximal number of moves for sorting with filling to the left and right is more than two times smaller than the sorting with filling from left to right.

For example, when $n=1000$, the maximal number of the moves

for constructing the ascending row with filling from left to right is 499500, and the average is 249750. When the filling is to the left and right the maximal number of the moves is 249500. This can be seen in table 4. When $n = 4$, these values are respectively 6, 3 and 2.

In comparison with sorting by LIT with filling from left to right [7] sorting by LIT with filling to the left and right use twice more memory and has additional operations: $n-1$ comparisons to determine the minimal number of moves; n recordings of the nearest left (**L**) or nearest right (**R**) vacant positions.

V. EXPERIMENTAL RESULTS

The proposed methods for sorting which use LIT are:

- filling to the left and right;
- filling to the left and right and comparisons with the current minimal and current maximal elements;
- filling to the left and right with avoiding repeated comparisons.

These methods are implemented in C++. We will name them LR, LR minimax, and LR repeat, respectively.

The aims of the experimental work is the following:

1. To compare the execution times of the proposed algorithms with some known algorithms. We use the algorithms: Bubble, Insertion sort, Selection sort and LtoRA [7].
2. To verify the influence of the proposed improvements (LR minimax, LR repeat) on the execution time of the investigated algorithm (LR).

For experiments a computer system is used with processor Intel Celeron E3300 2,5GHz, RAM 2,96 GB. The elements of the rows are generated by the functions rand() and srand().

The number of the elements of the rows for these experiments is from 2000 to 8000. The elements are integer numbers. Each algorithm sorts 10 times 4 different rows with number of the elements 2000, 3000, 4000, 5000, 6000, 7000 and 8000. The execution time is obtained after averaging the corresponding execution times.

Experiment 1. Sorting by the algorithms: LtoRA, LR, LR minimax, LR repeat, Bubble, Insertion sort and Selection sort integer numbers from 0 to 32767 (a low repetition rate for the elements).

The average times (ms) are shown in Table 5 and Fig.3.

In parentheses is shown the number of operations for sorting the row with algorithms LR, LR minimax and LR repeat. The number of operations is counted with a program.

Working time of the program cannot be considered as a reliable estimation because computers work in a multiprogramming mode and there is no guarantee that the tested program is not interrupted, which could increase its execution time. Also, the execution time is influenced by the memory organization.

As a result, the time for sorting of the same rows can be different. This is why, experimenting with the algorithms LR, LR repeat, LR minimax, first the number of operations for sorting the rows is counted and the obtained values are used as criteria for correct time results. Fig.5 shows result of counting the operations for sorting the row with 4000 elements with algorithm LR repeat (low repetition rate for the elements).

TABLE 5. AVERAGE TIMES (MS) FOR SORTING ROWS WITH LOW REPETITION RATE FOR THE ELEMENTS

Elem. number \ Algorithm	2000	3000	4000	5000	6000	7000	8000
LtoRA	19,9	38,6	78	123,5	177,8	236	311,1
LR	15,2 (85274 36)	35,5 (19113 969)	68,8 (34150 391)	104,7 (53386 151)	154,5 (76723 619)	207,5 (10428 6373)	273,4 (13615 8382)
LR mini max	15,1 (85124 21)	35,5 (19091 956)	67,3 (34118 041)	104,6 (53353 315)	153 (76674 177)	206 (10423 6432)	271,9 (13610 7945)
LR repeat	21,5 (93226 87)	45,8 (20867 827)	81 (36877 231)	120,5 (56958 461)	174,7 (81033 635)	239,3 (10985 6137)	304,9 (14248 2171)
Bubble	46,2	106,1	182,5	285,6	415,1	562,6	742,5
Insert. sort	7,5	9,1	15,5	31,1	43,3	56,3	78
Select. sort	9,1	12,2	25,2	43,1	59,1	78	104,6

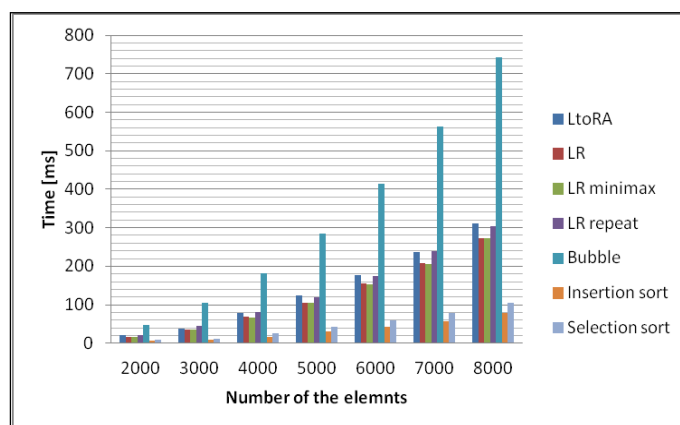


Fig.3 Average times for sorting the rows with low repetition rate for the elements

The experiments show that:

- 1) algorithm LR is faster than algorithms LtoRA and Bubble sort but it is slower than algorithms Insertion sort and Selection sort;
- 2) algorithm "LR minimax" reduced the number of operations (the time) compared with the operations (the time) of the algorithm LR;
- 3) algorithm "LR repeat" increases the number of operations (the time) compared with the operations (the time) of algorithm LR; the number of added operations "compare" is equal to the not inversed and equal pairs of elements in the row; if there are no equal elements, no comparisons are avoided.

Experiment 2. Sorting by the algorithms: LtoRA, LR, Bubble, Insertion sort and Selection sort for integer numbers with high repetition rate for the elements – 10 repetitions on average.

The average times (ms) are shown in Table 6 and Fig.4.

TABLE 6. AVERAGE TIMES (MS) FOR SORTING ROWS WITH HIGH REPETITION OF THE ELEMENTS

Elem. no \ Algorithm	2000	3000	4000	5000	6000	7000	8000
LtoRA	20	43,3	76,5	122	177,7	239,2	308
LR	15,3 (8521 897)	32,5 (1918 3809)	63,8 (3392 7700)	106,2 (5314 1336)	154,5 (7660 5673)	209,1 (10403 4350)	272 (13638 8051)
LR minimax	15,3 (8481 391)	32,5 (1907 2369)	63,7 (3379 7053)	106,1 (5293 6231)	153 (7638 5661)	209 (10374 3277)	270,5 (13609 9578)
LR repeat	6 (2969 425)	7,5 (6665 277)	20,2 (1171 2696)	32,5 (1843 2564)	51,4 (2657 8738)	70,4 (3615 8709)	90,2 (4738 2641)
Bubble	44,7	106	181	285,5	415,3	554,8	747
Insertion sort	4,5	12	18,6	31	43,3	60,9	78
Selection sort	7,5	13,9	25	37	49,8	79,5	101,6

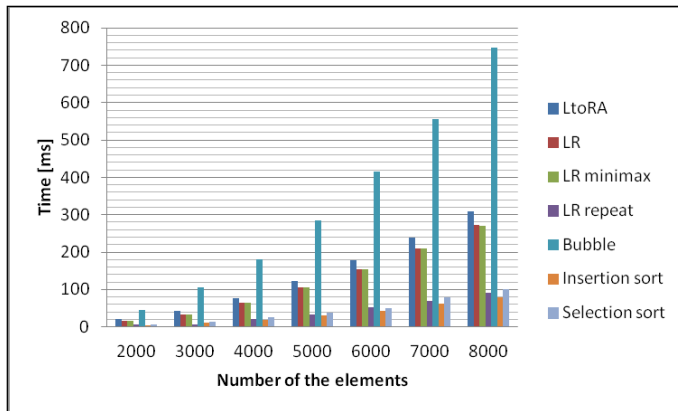


Fig.4 Average times for sorting the rows with a high repetition rate for the elements

The experiments show that:

- 1) algorithm LR is faster than algorithms LtoRA and Bubble sort but it is slower than algorithms Insertion sort and Selection sort;
- 2) algorithm “LR minimax” reduces the number of operations (the time) compared to the operations (the time) of the algorithm LR;
- 3) algorithm “LR repeat” is faster than algorithms LtoRA, LR minimax, Bubble and Selection sort but it is slower than Insertion sort; when the number of the repeated elements is large, the algorithm “LR repeat” is very effective. The number of operations (the time) compared to those of algorithm LR is reduced considerably.

The experiments show that the algorithm “LR repeat” outperforms the algorithm LR when the average number of repetitions in the row is greater than or equal to 2.

```

C:\WINDOWS\system32\cmd.exe
Number of the avoided compares when the left element is bigger - 157305
Number of the avoided compares when the left element is smaller - 169904
Number of the avoided compares - 327209 = 157305+169904
Number of the added compares - 3865528
Number of the equality - 244
-----
The number of inversions is: 3962568
-----
The number of the values 0 in the LIT is k0=12
The number of the values i in the LIT is ki=6
The number of the values in the LIT different from 0 and i is r=3981
The number of the moves to the left is sl=1005198
The number of the moves to the right is sr=1040767
The number of the moves is sl+sr=2045965
The number of elements which are moved to the left is el=1969
The number of elements which are moved to the right is er=2030
=====
The total number of the operation for sorting 4000 numbers is: 36877231
=====
Press any key to continue . . .
    
```

Fig.5. Number of operations for sorting the row with 4000 elements with algorithm “LR repeat” (a low repetition rate for the elements)

VI. CONCLUSION

This paper proposes the algorithm for sorting by LIT (Left Inversions Table) with filling to the left and right. The complexity of the proposed algorithm is evaluated. Its minimal and maximal complexities are derived. An experimental comparison of the proposed algorithm LR with algorithm LtoRA and some known algorithms (Bubble sort, Insertion sort, Selection sort) is also done. Two modifications of the algorithm LR are proposed and realized: “LR – comparisons with the current minimal and maximal values” and “LR with avoiding repeated comparisons”.

The experiments show that:

- a) algorithm LR is faster than algorithms “Bubble sort” and LtoRA but it is slower than algorithms “Insertion sort” and “Selection sort”;
- b) algorithm “LR repeat” is faster than algorithms LR for rows with number of repetitions larger than 2;
- c) obviously there is an average number of repetition for which the algorithm “LR repeat” will be faster than algorithm “Insertion sort”;
- d) algorithm “LR minimax” is faster than algorithms LR;

Finally, algorithm “LR minimax” can be used to sort any row, while using the algorithm “LR repeat” needs a preliminary estimate of the average number of repetitions in the given row.

The future work will continue with:

- 1) developing methods for quick estimation of the average number of repetitions in the row;
- 2) unification and applying both the improvements;
- 3) developing methods (algorithms) with smaller number of the comparisons and moves;
- 4) development and implementation of good parallel algorithms for sorting.

REFERENCES

- [1] Knuth D., The art of computer programming, V3. Sorting and Searching, Addison Wesley Publishing Company, 1973.
- [2] Stoichev St., Synthesis and analysis of algorithms, BPS, Sofia, 2003 (in Bulgarian).
- [3] Nakov P., P. Dobrikov, Programming++Algorithms, TopTeam Co, 2003 Hakov (in Bulgarian).
- [4] Sedgewick R, Algorithms in C, Addison-Wesley, 1990.
- [5] Harris S., J. Ross, Beginning Algorithms, 2005.

- [6] Wirth N., Algorithms+data structures=programs, Prentice-Hall, 1976.
[7] N. Vasilev, A. Bosakova-Ardenska, Algorithms for sorting by left inversions table, International Review on Computers and Software (IReCoS), vol 7 n2 – Part A, 2012, ISSN 1828-6003, pp 642-650.

BIOGRAPHIES



NAIDEN B. VASILEV is associate professor in department of “Computer Systems and Technologies” at Technical University of Plovdiv. He is receives Ph.D. in 1976. His research interests include: parallel algorithms, discrete mathematics and music.



ATANASKA D. BOSAKOVA-ARDENSKA was born in 1980. She received the M.Sc. degree of Computer Systems and Technologies at Technical University of Sofia, Plovdiv branch 2004. She receives Ph.D. in 2009 with thesis “Parallel information processing in image processing systems”. From 2010 she is assistant in department of Computer Systems and Technologies in University of Food Technologies. From 2014 she is associated professor by “Synthesis and Analysis of Algorithms” in department of

Computer Systems and Technologies in University of Food Technologies in Plovdiv, Bulgaria. She is member of USB (Union of Scientist in Bulgaria) and head of Club of Young Scientists in Plovdiv (USB – Plovdiv in Bulgaria). Her research interests include: parallel algorithms, sorting algorithms, image processing, MPI (Message Passing Interface), C++ programming.

Classification of ECG Signals By the Neighborhood Feature Extraction Method

C.Bakir

Abstract— In this study, non-linear dimension reduction methods were applied to ECG signals and success of such dimension reduction techniques for the classification and segmentation of ECG signals were discussed. Also, segmentation of data through neighbourhood feature extraction (NFE) method were enabled by transiting from high dimensioned space to low dimension space by considering the longitudinal combination of ECG signals. Results classification results of NFE algorithm performed through longitudinal combination and as a newly developed method were compared with classification results of ECG signals obtained through dimension reduction by taking one pixel. Results of NFE dimension reduction technique performed by considering the neighbour pixels, advantage of effect on segmentation of ECG signals were presented at empirical results section and the success of suggested method was indicated. Results obtained by performed study are promising for the studies to be conducted in further period.

Index Terms— classification; ECG; kNN; Neighbourhood Feature Extraction; RBF.

I. INTRODUCTION

ELECTROCARDIOGRAM (ECG) means electrical signs, which show how the heart works in the human body and also show heart motions. Cardiac diseases arisen depending on cardiac arrhythmias, and cardiologic disorders and anomalies occurred in heart are diagnosed by ECG signals. Therefore, it is very important today that ECG signals can be analyzed properly [1].

Today most people die depending on cardiac diseases. Therefore, attention must be paid to heart health. ECG records any changes in the electrical signs generated in the heart and dispersing to all body and tries to diagnose any disorders occurred in the heart. ECG shows briefly the heartbeat and is used commonly in signal processing [2].

Most studies are conducted on classification of ECG signals. But, in the studies, it is not ensured exactly that ECG signals may be understood quickly and interpreted properly. The new method developed together with this study is applied successfully to all dimension reduction techniques. Furthermore, success to classify any ECG signals is increased and it is endeavored to guide any studies to be conducted in other biomedical fields as well.

In the study, firstly a stripe selection and feature extraction are conducted for dimension reduction. In this study, it is endeavored to conduct a classification by the instructional methods and by utilizing the feature extraction in ECG data and using the class labels. There are most methods to conduct the feature extraction. Of these methods, the oldest and most known linear technique is PCA [3]. But, the linear techniques are not sufficient to obtain any information. Any non-linear techniques are required to classify any complex data. To that end, most nonlinear techniques are used recently. In our study, the nonlinear techniques, which keep the local properties such as Kernel PCA, Isomap, etc., are used for our existing dataset as well as the non-linear feature extraction techniques, which keep the global properties such as Laplacian Eigenmaps, etc. Furthermore, the linear extraction techniques such as PCA and LDA are also used to compare the classification success with the non-linear techniques [4].

Secondly, we discuss 5, 10, 15, 20 and 50 extensional neighborhoods for our dataset generated by us by these feature extraction methods and try to classify ECG data [5]. In ECG data, each data is stated as a sample point. This example point is called "pixel." The vectors generated for these pixels are valid for all stripes and have a particular value. If class of a pixel is certain, class of the pixel immediately adjacent to that pixel is the same as that pixel and this adjacent pixel shows the extensional neighborhood. $n \times n$ neighbor around this extensional neighborhood is taken for ECG signal as ECG signal is trained. Proximity of the extensional neighborhood between two points is measured by Euclidean distance. Two close data points are similar in extensional neighborhoods and the likelihood that these points are in the same class is high. For $n \times n$ neighbor, similarity reduces as distance increases.

II. METHOD

A large amount of data is dealt with in the real world. Therefore, much more memories and calculations are required to classify data properly. Data is used efficiently as data reduction and cost is reduced. To conduct this transaction without any data loss, the dimension reduction methods are required to ensure the dimension reduction and to reduce number of stripes. The feature extraction constitutes a very important step in processing the high dimensional data. The feature extraction is conducted by the linear or nonlinear methods on the stripes. In this study, firstly the feature extraction is conducted to perform an instructional study, to increase the classification success and to reduce the transaction cost by using the class information.

C. BAKIR, is with Department of Computer Engineering University of Yildiz Technical University, Istanbul, Turkey, (e-mail: cigdem@ce.yildiz.edu.tr).

Signatures are taken that provide any particular properties primarily to process all data. These spectral signatures are identified as ones that represent the spectral distribution in the best way as much as possible. The techniques of nonlinear feature extraction are applied to these spectral signatures instead of all data. The existing dataset is obtained by the dimension reduction techniques used in the study by extracting 5- and 10-dimensional vectors. Furthermore, RBF and kNN interpolation is used to instruct all dataset. The dataset reduced by RBF is learnt by an artificial plexus and it is moved from each spectral signature from a low dimensional space by using a network structure. RBF is formed by linkages between neurons. At the education stage, weights of the neurons are updates by examining inputs and outputs. This transaction continues until the error rate will be minimum [6]. In kNN interpolation method, k is found depending on the nearest samples. The nearest neighborhood of the data normalized in kNN interpolation is found and weights are calculated [7]. In this method, the spectral signatures and distances of each pixel in EKG data are found. Then, the value of k=9 is selected and the nonlinear dimension reduction methods of the spectral signature k nearest to the pixel with a dimension to be reduced are found and the feature vectors are obtained. Here, the purpose is to find the nearest intermediate assessment to be obtained by the nonlinear projection methods. This method is applied to all spectral signatures and the dimension is reduced.

A. Principal Component Analysis (PCA)

Principal Component Analysis (PCA) is most popular orthogonal linear transformation. PCA is an illustration of the data having the biggest variance in the low dimensional space. High variance features are prepared with respect to low variance. M linear mapping of samples of X data matrix is founded that increases the cost function, calculating the covariance matrix. It gives the eigenvectors corresponding to the biggest eigenvalue. PCA uses the Euclidean distance between the data points x_i and x_j . PCA transformation is shown as $\mu^T = X^T W$. W shows the orthogonal matrix; μ^T shows the linear transformation, and W shows the eigenvectors corresponding to the covariance matrix [8].

PCA is a linear illustration of the data. The data is separated by PCA as shown in Equation 1 [8].

$$x_i = \sum_{j=1}^p w_{ij} Q_j \quad (1)$$

B. Linear Discriminant Analysis (LDA)

PCA states a high variety of data by a minimum number of components. But, these components never require best variety to classify them differently to ensure highest separation. To classify the data properly together with LDA, highest separation between different classes of data is ensured. It finds the dimension reduction required to provide this separation, calculating the covariance matrix. Total covariance matrix is calculated, utilizing the covariance matrix within the classes (S_W) and the covariance matrix between the classes (S_B) [1].

$$S_T = S_W + S_B \quad (2)$$

C. Kernel Principal Component Analysis (KPCA)

KPCA is an expanded version of PCA method. But, KPCA is a nonlinear technique, which improves the linear techniques, while PCA is a linear method. Dimension of the data is reduced, using the Kernel matrix. The K kernel matrix is calculated, using the data points x_i and x_j as $k_{ij} = K(x_i, x_j)$. Centers and d vectors are found, changing inputs of the K kernel matrix. Thus, the data is transferred by means of KPCA to a higher dimensional space according to PCA dimension reduction technique. In KPCA, the important thing is to select the kernel function. Kernel function may be a linear kernel, Gauss kernel and polynomial kernel. In the studies conducted in the literature, KPCA provides fairly successful results in face recognition and speech recognition [9,10].

D. Isomap

Isomap is a low dimensional embedding method, which is used in multi-dimensional scaling algorithms on a weighted graphic and uses a geodesic distance instead of an Euclidean distance. The geodesic distance is the shortest distance and to find this distance, neighborhoods between all data points must be found. The geodesic distance data points are calculated by $x_i x_j$ ($i=1,2,\dots,n$) in the neighbor graphic. Furthermore, it is also important to select a neighborhood parameter in Isomap. The linkage in each data point is known as the nearest Euclidean distance in a high dimensional space. The nearest distance between two points is calculated by the Dijkstra algorithm [11].

E. Laplacian Eigenmaps

It ensures that the data is transferred to a low dimensional space, keeping its manifold local properties. The Laplacian method firstly composes the G graphic in conjunction with its nearest neighborhood k and selects a weight. For the data points x_i and x_i , the edge weights are calculated by Gauss. In the cost function in illustration in a y_i low dimensional space, the weights w_i depend on short distances between the data points x_i and x_j . Thus, y_i and y_j minimize the cost function by the spectral graphic theory. M degree matrix is stated as W diagonal matrix in L laplacian graphic. Self-separation of the Laplacian graphic is conducted and a low dimensional embedding is created [12].

III. EXPERIMENTAL STUDY AND RESULTS

In this study, PTB (Physikalish-Technische Bundesantalt) ECG dataset is used. This dataset is generated by taking 549 ECG signals by the German National Metrology Institute from 289 people. 9 different diagnoses are made on the patients depending on heart diseases. Furthermore, each entry contains 15 signals measured simultaneously. Each signal is digitalized approximately by 1000 samples per second [13].

TABLE I
RESULTS OF RBF CLASSIFICATION ALGORITHMS FOR DIMENSIONS 5 AND 10

Feature Extraction Methods	RBF	
	5 dimensions	10 dimensions
PCA	72.65	73.84
LDA	68.66	65.37
KPCA	78.13	80.31
Isomap	79.04	79.56
Laplacian E.	80.25	82.03

TABLE II
RESULTS OF kNN CLASSIFICATION ALGORITHMS FOR DIMENSIONS 5 AND 10

Feature Extraction Methods	kNN	
	5 dimensions	10 dimensions
PCA	75.83	75.25
LDA	65.72	69.84
KPCA	84.35	85.04
Isomap	85.67	83.39
Laplacian E.	86.69	88.34

The results obtained by kNN interpolation for dimensions 5 and 10 are shown in Table 2, while the classification results obtained by RBF for dimensions 5 and 10 are shown in Table 1. In Table 3, the results of classification done by RBF in NFE technique and suggested by ensuring the extensional combination for dimension 5 are shown, and in Table 4, the results of classification done for dimension 10 are shown.

TABLE III
THE RBF CLASSIFICATION RESULTS OF THE DATA OBTAINED BY NFE TECHNIQUE FOR DIMENSIONS 5

Feature Extraction Methods	Neighborhoods Values				
	5	10	15	20	50
PCA	75.87	85.34	87.62	85.34	64.37
LDA	70.12	75.82	79.87	80.12	60.72
KPCA	82.88	90.12	92.11	87.64	70.37
Isomap	83.17	88.72	95.64	87.62	71.64
Laplacian E.	84.62	90.62	97.83	94.62	74.83

TABLE IV
THE RBF CLASSIFICATION RESULTS OF THE DATA OBTAINED BY NFE TECHNIQUE FOR DIMENSIONS 10

Feature Extraction Methods	Neighborhoods Values				
	5	10	15	20	50
PCA	75.01	77.83	80.64	78.62	64.33
LDA	71.64	79.65	74.62	73.13	60.06
KPCA	85.37	87.83	91.62	85.12	73.62
Isomap	82.64	89.67	91.24	83.64	77.37
Laplacian E.	84.65	90.83	95.62	92.47	78.12

TABLE V
THE kNN CLASSIFICATION RESULTS OF THE DATA OBTAINED BY NFE TECHNIQUE FOR DIMENSIONS 5

Feature Extraction Methods	Neighborhoods Values				
	5	10	15	20	50
PCA	80.62	87.64	89.63	82.52	70.03
LDA	70.62	73.52	75.64	73.27	64.87
KPCA	87.64	92.02	96.75	91.54	71.64
Isomap	89.64	93.52	98.64	97.62	78.54
Laplacian E.	89.12	95.52	99.14	96.82	71.87

In Table 5, the results of classification done by kNN interpolation in NFE technique and suggested by ensuring the extensional combination for dimension 5 are shown, and in Table 6, the results of classification done for dimension 10 are shown.

TABLE VI
THE kNN CLASSIFICATION RESULTS OF THE DATA OBTAINED BY NFE TECHNIQUE FOR DIMENSIONS 10

Feature Extraction Methods	Neighborhoods Values				
	5	10	15	20	50
PCA	78.62	83.64	85.72	84.17	65.67
LDA	74.44	76.62	79.87	75.67	61.12
KPCA	90.67	94.86	97.61	95.62	76.15
Isomap	84.61	88.63	90.82	87.46	71.04
Laplacian E.	90.26	95.65	98.79	87.54	78.22

In the study conducted in Table 1 and Table 2, it is observed that the suggested method increases the classification success

considerably based on the results suggested in Tables 3, 4, 5 and 6. Especially the neighborhood value 15 has highest classification success. But, a considerable increase in neighborhood reduces the classification success.

It is observed that NFE technique increase the success in classification of ECG signals more than 10% in both classification algorithms.

IV. CONCLUSION

In this study, non-linear dimension reduction methods were applied to ECG signals. Also, segmentation of data through neighbourhood feature extraction (NFE) method by transiting from high dimensioned space to low dimension space by considering the spatial combination of ECG signals with results classification of traditional nonlinear feature extraction were compared. In this study, an extensional combination is provided and advantages of the dimension reduction on classification are submitted. Success of NFE technique suggested in this study on classification of ECG signals is shown. In any studies to be done in the future, it shall be ensured that NFE technique shall be improved further and applied in different practice fields.

REFERENCES

- [1] Kiranyaz S., Ince T. etc, "Personalized long-term ECG classification: A systematic approach", *Expert Systems with Applications*, vol.38, issue 4, pp.3220-3226, 2011.
- [2] Erdoğan P., Peşçaker A., "Dalgacık Dönüşümü ile EKG Sinyallerinin Özellik Çıkarımı ve Yapay Sinir Ağları ile Sınıflandırılması", *5.Uluslararası İleri Teknolojiler Sempozyumu (IATS'09)*, 2009.
- [3] Martis R., Acharya R. And Min L., "ECG beat classification using PCA, LDA, ICA and Discrete Wavelet Transform", *Elsevier Biomedical Signal Processing and Control*, vol.8, issue 5, pp.437-448, 2013.
- [4] Ceylan R., Ozbay Y., "Comparison of FCM, PCA and WT techniques for classification ECG arrhythmias using neural network", *Expert Systems with Applications*, vol.33, issue 2, pp.286-295, 2007.
- [5] Bakir C., "Nonlinear Feature Extraction for Hyperspectral Images", *International Conference on Advanced Technology & Sciences (ICAT'14)*, pp.945-949, 2014.
- [6] Silipo R., Bortolan G. And Marchesi C., "Design of hybrid architectures based on neural RBF pre-processing for ECG analysis", *International Journal of Approximate Reasoning*, pp.177-196, 1999.
- [7] Castillo O., Melin P. ETC, "Hybrid intelligent system for cardiac arrhythmia classification with Fuzzy K-Nearest Neighbors and neural networks combined with a fuzzy system", *Expert Systems with Applications*, vol.39, issue 3, pp.2947-2955, 2012.
- [8] Maglaveras N., Stamkopolous T. etc, "ECG pattern recognition and classification using nonlinear transformations and neural networks:A review", *Medical Informatics*, vol.52, issue 1-3, pp.191-208, 1998.

- [9] Wen Y., He L. And Shi P., "Face recognition using difference vector plus KPCA", *Digital Signal Processing*, vol.22, issue 1, pp.140-146, 2012.
- [10] Widjaja D., Varon C.etc, "Application of Kernel Principal Component Analysis for Single-Lead-ECG-Derived Respiration", *IEEE Transactions on Biomedical Engineering*, vol.59, no.4, pp.1169-1176, 2012.
- [11] Shalbaf A., Alizadefani Z. And Behram H. "Echocardiography without electrocardiogram using nonlinear dimensionality reduction methods", *J.Med Ultrasonics*, vol.42, pp.137-149, 2015.
- [12] Perry T., Zha H. etc, "Supervised Laplacian Eigenmaps with Applications in Clinical Diagnostics for Pediatric Cardiology", *Computer Science & Learning*, 2012.
- [13] Vozda M., Cerny M., "Methods for derivation of orthogonal leads from 12-lead electrocardiogram:A review", *Biomedical Signal Processing and Control*, vol.19, pp.23-34, 2015.

BIOGRAPHY



CIGDEM BAKIR was born in İstanbul. She received the B.S. degrees in computer engineering from the University of Sakarya, in 2010 and the M.S. degree in computer engineering from Yildiz Technical University, İstanbul, in 2014.

Since 2012, she was a Research Assistant with the Yildiz Technical University. Her research interests include recommendation systems, data mining, image processing and biomedical signal processing.

In-Home PLC Coexistence with Wi-Fi and Ethernet access Networks

E. Hamiti, T. Berisha and F. Peci

Abstract—BPL or PLC is relatively a new technology that is considered an attractive system to deliver broadband communications over power lines. The main objective of paper is to understand the impact of in-home PLC devices in case of integrated environment with other technologies. Initially, FTW Simulator for channel transfer function analysis of an in-home PLC network topology is used. Furthermore, through measurements conducted in laboratory environment different scenarios are built for different test scenarios and the coexistence of in-home PLC, Ethernet and Wi-Fi Networks is investigated. Toward the end of the paper, throughout different scenarios the impact on video quality of in-home PLC, will be closely monitored and evaluated.

Index Terms—BPL, channel transfer function, FTW simulator, in-home PLC.

I. INTRODUCTION

THE PLC (Power-line Communications) in general is a promising solution for first mile and last mile broadband access. It appears that broadband access is a broader concept related to the growth of science, economy aspects and also tourism and culture. In-home PLC, Home-plug AV and indoor BPL (Broadband over Power-lines) are dedicated standards providing a broadband access solution to in-home users. Nowadays there are a lot of PLC devices with different characteristics of transmission speeds and capabilities. Moreover Home-plug and BPL devices include products that have flown from different standards.

In this section the simulations derived from FTW are described and a simulator is used for modeling channel transfer function for in-home PLC [1,2] (FTW is PLC Simulator based on Matlab source code which is used to characterize PLC channels). Through this simulator are conducted a considerable number of simulations for different kind of topologies and characteristics. In power-line communication network the signals propagate

from transmitter to receiver facing a harsh and noisy transmission medium. Using the FTW simulator is possible to derive the best possible frequency band where the voice and data can be transmitted.

The simulations are performed in the frequency band from 100 KHz up to 30 MHz matched to the modeled characteristics of the simulator.

There are a number of basic conducted measurements performed in various scenarios as well. Measurements include different topologies and each of them designed for various purposes. By using various scenarios the importance of PLC is investigated as a redundant link during intermittent drops of one healthy link while video-streaming. In the rest of scenarios the focus is on load-sharing of packets where the topology includes two links for transmitting the signals from transmitter to receiver. The topology is composed of different technologies like Wi-Fi and Ethernet along with in-home PLC devices.

The motivation for building these kind of topologies is derived from the possibilities of using the in-home PLC not only for home use where the inside users can have access to broadband, but also in the environments like mining industry and other kind of industries where the broadband access is necessary even for monitoring purposes. The efficient bandwidth utilization is another target analyzed in measurements conducted on this paper.

The paper is organized as follows: Section II elaborates the channel transfer function (H) for a predefined in-home PLC topology, Section III analyses the laboratory measurements and Section IV gives a conclusion.

II. CHANNEL TRANSFER FUNCTION ANALYSIS THROUGH SIMULATIONS

The proposed simulations in this paper include the in-home PLC network topology that matches as close as possible to a realistic indoor power-line networks in our country (Kosovo, South Eastern Europe). On the other hand the channel transfer function is defined from the theory of two-port network model as a ratio between load voltage V_L and source voltage V_S by:

$$H = \frac{V_L}{V_S} \quad (1)$$

The above can be rewritten as a function of A, B, C, D, ZL, and ZS as follows:

E. Hamiti University of Prishtina, Faculty of Electrical and Computer Engineering, Prishtina, Kosovo, Corresponding author, (email: enver.hamiti@uni-pr.edu)

T. Berisha, University of Prishtina, Faculty of Electrical and Computer Engineering, Prishtina, Kosovo, (email: taulant.berisha@uni-pr.edu)

F. Peci, University of Prishtina, Faculty of Electrical and Computer Engineering, Prishtina, Kosovo, (email: fatos.peci@uni-pr.edu)

$$H = 20 \times \log_{10} \left| \frac{Z_L}{A \times Z_L + B + Z_S \times (C \times Z_L + D)} \right| \quad (2)$$

where A, B, C, D are the 2x2 matrix elements according to the ABCD Line Modeling, whereas Z_S and Z_L are the source impedance and load impedance respectively [3-6].

In this paper the in-home PLC network topology that is matched to our country environments will be presented. Referring to the topology as depicted below (Figure 1), there are a service panel (SP) positioned in the center of topology and outlets (OL) connected to the distribution boxes (DB) etc. The DBs are considered boxes positioned per each room for in-home environments. The SP connects the energy provider side to in-home electrical side.

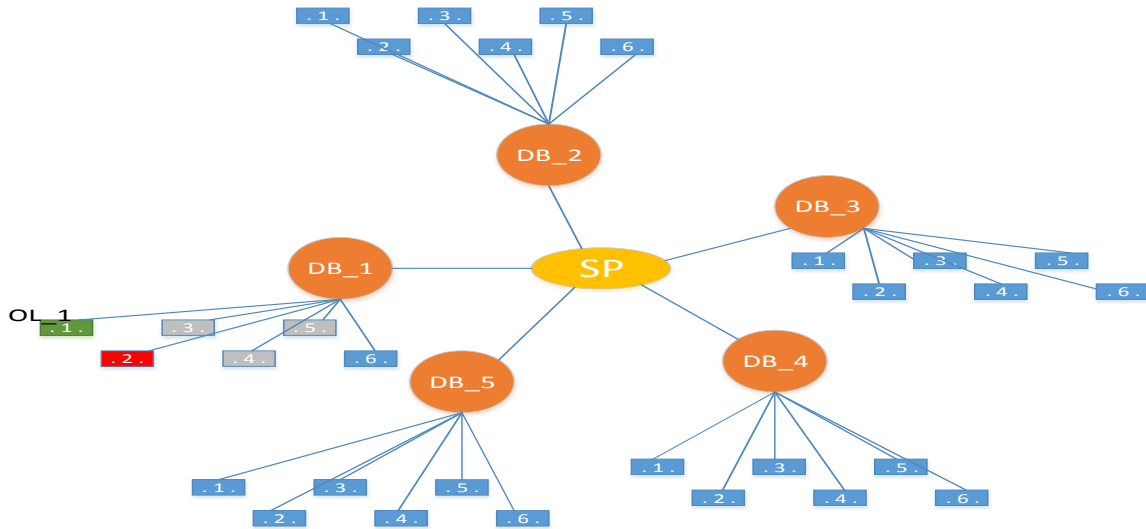


Fig.1. The topology of in-home PLC network for channel transfer function analysis

From the above topology we can see the connections between topology elements. The distance between SP and DBs is 6 m and is the same for five connections, whereas the distance between each DB and OLs connected to it are 5.2, 5.4, 5.6, 5.8, 6.0 and 7 m respectively. Cable types used in topology are of sections 2.5 mm. Transmitter (equivalent as Z_S and colored as green) and receiver (equivalent as Z_L and colored as red) have a common value of 100 Ω . Star connection type is used for connection between OLs and respective DBs.

It is important to see what happens to the channel transfer function for the topology as above on situation where position of receiver changes from OL_2 to OL_3 and so on. Below are depicted the graphic results which will be analyzed on the following.

Figure 2 shows an example from which may be observed that differences between channel transfer functions are slightly change from each other.

The analysis as it can be seen from the legend is performed for the cases where receiver changes the position from one outlet to another within distribution

box (DB_1 in this case) in which is connected to. If the range from transmitter (T) to receiver (R) is increased there is a longer path linking T and R. It is expected to be corrupted the channel performance caused by this increasing. The simulations are conducted from 100 KHz up to 30 MHz as it can be seen from Fig. 2. Also the bandwidth from 7-15 MHz is not suitable for transmission because of high level of attenuation. Apart from transmitter and receiver the topology presented consists of RLC circuits as well. These circuits are considered as appliance circuits when are connected to outlets in randomly way. In the topologies where there is no RLC circuit connected to outlets, the bandwidth up to 5 MHz shows an improvement of attenuation, whereas the bandwidth from 7-15 MHz remains problematic. The receivers from different vendors have their specifications related to the receiving capabilities. The power noise level is not desirable to be lower than around -90 dB for getting the better performance for receiver devices. The careful should be taken mainly in the bandwidths mentioned above although nowadays devices use bandwidth up to 62.5 MHz for networking, HD video-streaming, online gaming and more services.

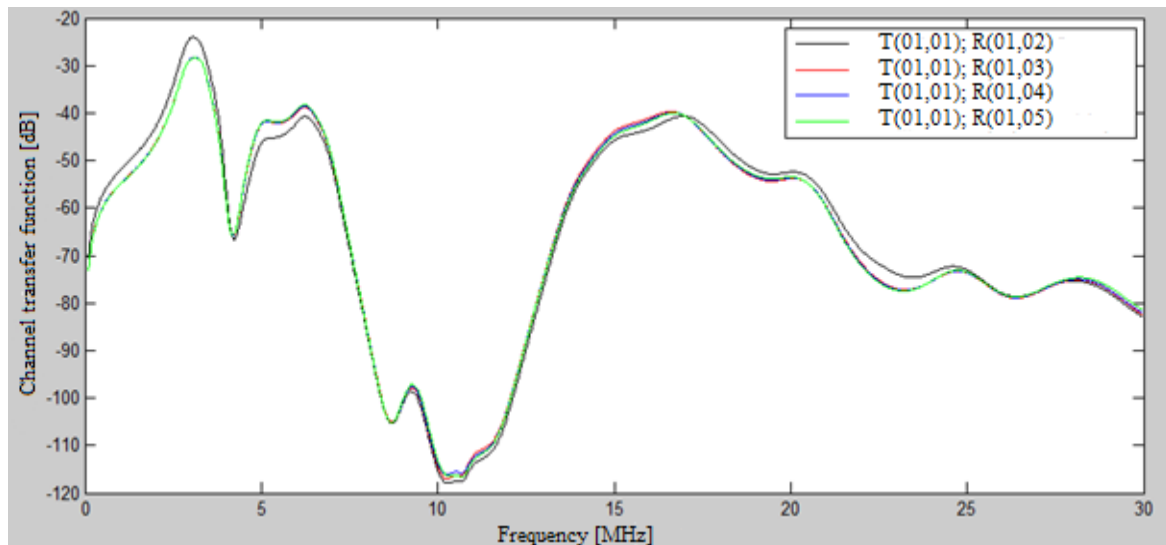


Fig.2. Channel transfer function (H) realizations of 4 different receiver positions

III. LABORATORY TESTBED AND IN-HOME PLC MEASUREMENTS

Using PLC adapters for different environments when there is no need for building infrastructure is optimal solution and even cost-effective. The general purpose of measurements is to investigate the coexistence between technologies like in-home PLC, Wi-Fi and Ethernet. The jitter and latency for video-streaming and similar services like monitoring are to be analyzed whereby the results are shown on the following.

3.1 Laboratory Test-bed

The proposed test-bed in this paper consists of:

- 2 PLC adapters compliant with IEEE1901 and compatible with Homeplug AV [4],
- 2 PCs equipped with 100 and 1000 Mbps NIC (Network Interface Cards),
- 2 Cisco routers
- 1 Cisco Ethernet switch (not presented on the following topologies).

Within this paper three measurement scenarios were conducted:

- Scenario 1: Bottleneck analysis near 100 Mbps and importance of different transmission mediums.
- Scenario 2: High Redundancy analysis in case where the primary link is down (Ethernet link) and video-streaming

quality between PC_1 (transmitter) and PC_2 (receiver).

- Scenario 3: Load-sharing per packet (utilizing two links, PLC in combination with Wi-Fi and Ethernet) analysis and video-streaming quality.

The scenarios are shown on subsequent figures. Scenario 1 (Figure 3) is composed of PLC adapters (HD Power-line Adapter with data rate 500 Mbps) and 2 PCs connected on each side.

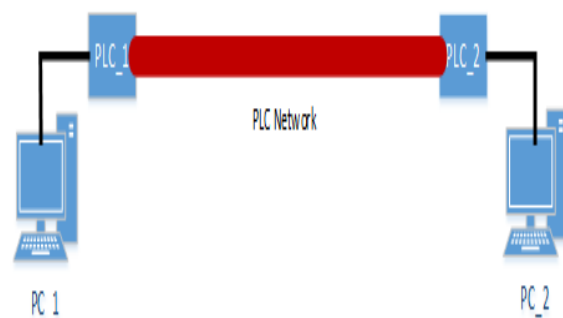


Fig.3. Scenario 1

Scenario 2 is composed from two links whereas scenario 3 is composed from a mixed network. The latest scenario is the most complicated compared to others. The size of video-streaming file is 700 MB which is transmitted through the mixed network and Ethernet network, alternatively, with target to measure the quality of video in transient moments of different scenarios.

PLC adapters are used throughout all the scenarios, capable to transmit in data rates up to 500 Mbps and range distance up to 300 m for in-home environments.

3.1 Bandwidth, Jitter, Latency Measurements and Quality of Video-streaming

Scenario 1 illustrates an example where PLC_1 (transmitter) transmits a video-streaming to PC_2 (receiver) through the Ethernet and PLC Network. The primary objective of this scenario is to measure the video quality at PC_2 for the data rates 10, 100 and 1000 Mbps. PLC adapters have capability of 500 Mbps data rates, but both of PLCs are equipped with 100 Mbps NICs whereas 1000 Mbps NICs are not used. It is obvious that in case of 10 Mbps data rate the video quality transmitted via UDP on port 1234

(User Datagram Protocol) has not changed. In the second test the data rate is increased to 100 Mbps, the incoming rates with value 96.5 Mbps at PC_2 were recorded using **Iptraf** tool [7]. In this case quality of video is qualitatively degraded as it is shown on Figure 4. From this scenario it is understood that even when PLC adapters have a data rate of 500 Mbps, using cat5e Ethernet cables, it is not able to utilize the capacity of PLCs because of auto-negotiation mechanism. This mechanism offers the data rates limited on 10/100/1000 Mbps as Ethernet standard does not support other data rates. The scenario 1 shows such a problematic solution in these situations.



Fig.4. The degradation of video quality for 100 Mbps data rate.

Scenario 2 as depicted on Figure 5 illustrates a different case where the PLC Network is used as a redundant link. On the interfaces of routers is activated the OSPF (Open Shortest Path First) protocol. In this test is forced an Ethernet link dropping down in order to measure the video quality at receiver PC as well as transient period. In case of Ethernet link goes down, it is observed a delay of up to 4 s for the video to turn into acceptable quality.

Figure 6 shows the video quality at receiver side, whereas on right hand side of this one is shown the original image. This is done for comparison reasons where original image is used as a reference of comparison.

From the above figure we are also able to observe the time when the link is on switching phase from Ethernet to PLC link.

The load-sharing is such a mechanism that provides packet balancing which results in utilizing two links (Ethernet and PLC in our case). This is another test where on the router from left hand side the load-sharing per packet is enabled. On both sides (transmitter and receiver) are running the **Jperf** through which it has been able to measure jitter.

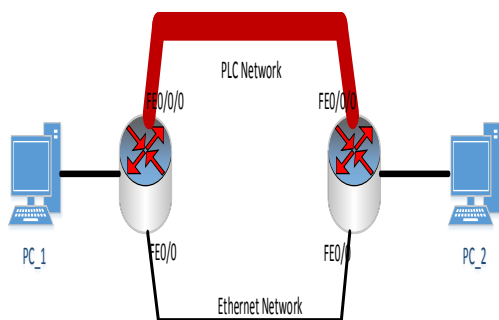


Fig.5. Scenario 2



Fig.6. The degradation of video quality at the moments when link (Ethernet) goes down

Figure 7 shows the jitter results measured for the last 30 s (transmit interval is 60 s with 5 parallel streams). UDP is used with 10 MBps throughput, 41 kB buffer size and 32 kB packet size. Jitter results

show that for this period the maximum value of jitter is 1.25 ms. The real-time applications are sensitive to latency and jitter so a latency of more than 50 ms should be considered for different services.

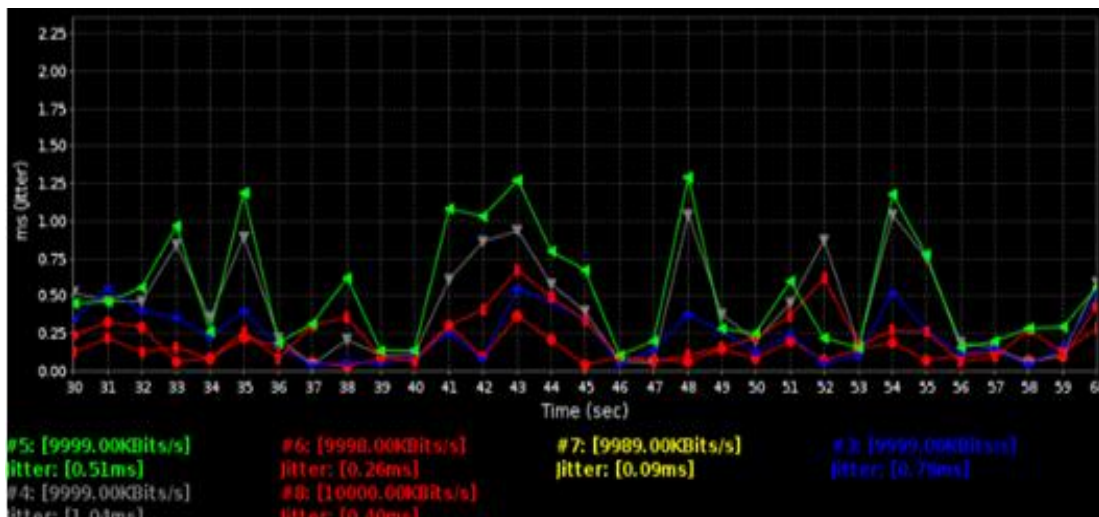


Fig.7. Jitter values for load-sharing per packet

Scenario 3 is more complicated in comparison to other scenarios because the network topology consists of two links (Figure 8) where the upper link is a combination of three technologies, Ethernet, Wi-Fi and PLC.

After configuring the load-sharing per packet on router the traffic is divided, such that one packet goes via upper link (PLC and Wi-Fi) and the next one goes via lower link (Ethernet only).

A Wireshark capture is run on both sides of network topology (PC_1 and PC_2) [8]. Packets sent from transmitter to receiver are different in order.

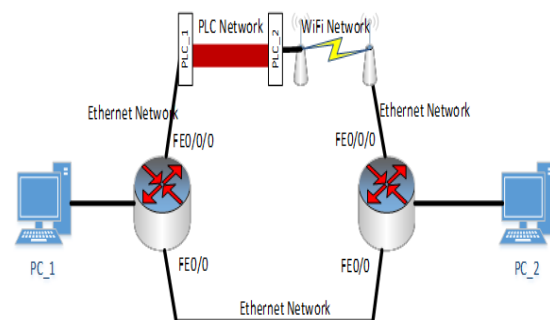


Fig. 8 Scenario 3

The load-sharing per packet affected MPEG packets (Figure 9) where is observed that a few packets to be lost. Therefore, in the situations of packet-sharing enabled the video quality may be degraded.



Fig.9. Video quality at receiver side (left image) in case of load-sharing per packet enabled

If the quality of the received video is compared to the original image captured at the transmitter side there are differences at the certain moments. However, this quality is acceptable because these degradations are appeared only in short intervals and non repeatable. Therefore, in these situations although is utilized the upper and lower capacity of links and also the packet-sharing is enabled this is not any more

excellent video quality guarantee. **Jperf** is run similarly to scenario 2, on PC_1 and PC_2. Figure 10 shows the jitter measurements for 5 parallel streams. The testing interval is 60 s. regarding to the jitter results observed, the value of jitter is significantly higher than the same results from scenario 2. The jitter and also latency are increased due to Wi-Fi and PLC networks.

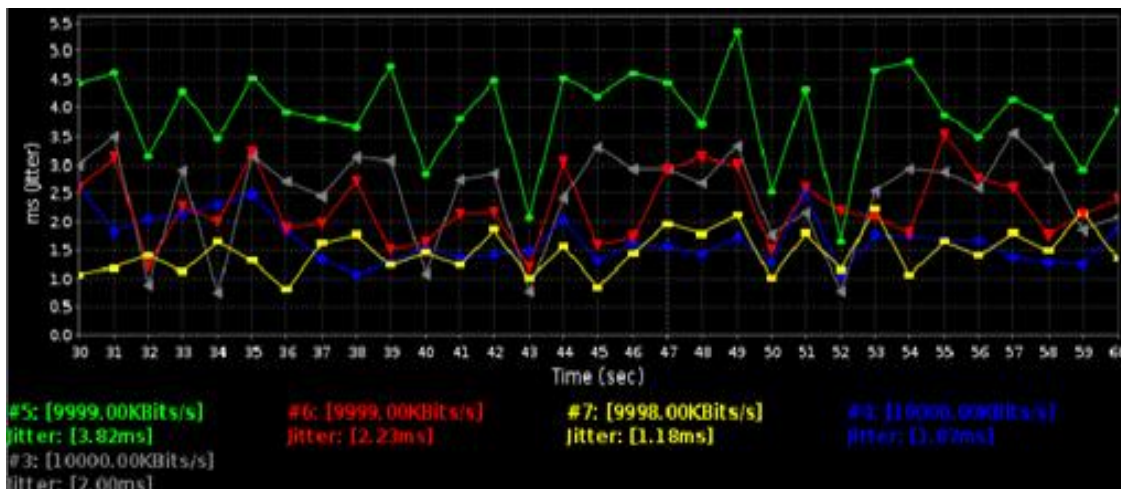


Fig.10. Jitter values for scenario 3 load-sharing per packet

Below are tabulated values for three cases related to the jitter and latency parameters about all mentioned technology combinations. It is interesting to observe the latency of packets for different cases. The mean values of latency are derived from 34 packets measured from ping test. Figure 11 illustrates the latency for every packet including cases of technology combinations.

If we relate Figure 11 and results from Table I (mean value of latency), it is able to observe the whole interval of packets whereby the combination of Wi-Fi+Ethernet+PLC contains the largest values of latency.

TABLE I
JITTER AND LATENCY VALUES FOR DIFFERENT CASES.

Measured values	Load-sharing per packet enabled		
	Wi-Fi + Ethernet + PLC	WiFi+Ethernet	Ethernet + PLC
Max. value of jitter [ms]	5.5	3.5	1.25
Mean value of latency [ms]	5.3235	1.4412	3.0645

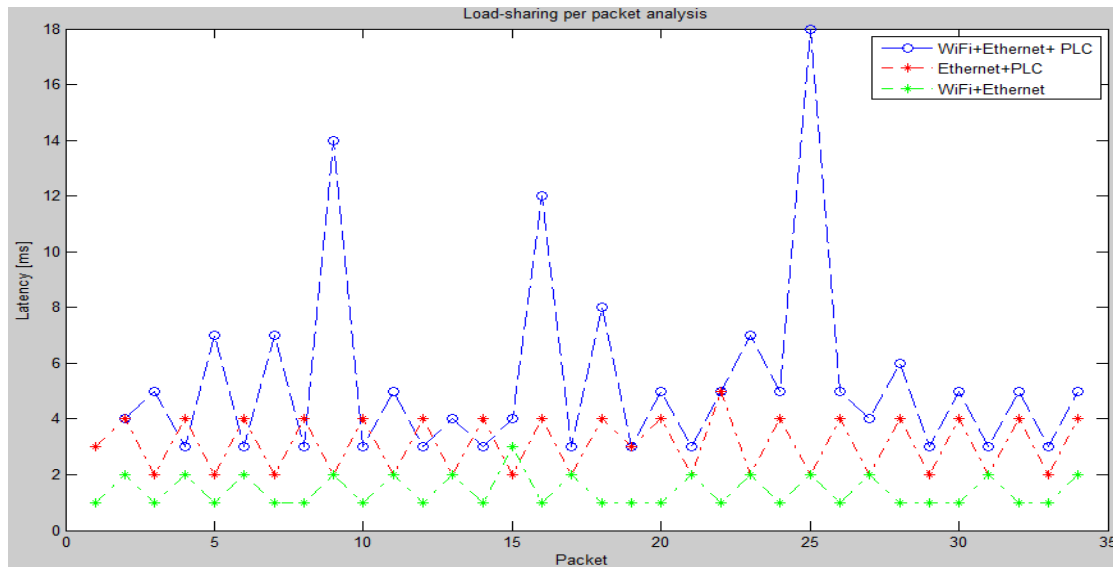


Fig.11. Latency values for 34 packets with various combination of technologies

IV. CONCLUSION

Apart from home use the PLC technology apparently due to its good bandwidth characteristics there may be more alternatives where this technology may penetrate. The environments such as: Mining industry for monitoring purposes or Urgent cases whenever there is an already existent electrical infrastructure.

The channel transfer function is very important, so the results presented in this paper show a problematic bandwidth from 7-15 MHz. The data transmitted should be under control in order to make sure that the power noise level is not being lower than -90 dB. Also differences in distance range between outlets from different distribution boxes may cause changes in channel transfer function more than outlets positioned within the same distribution box. In the situations where the network topology is complicated there are presented more oscillations on channel transfer function.

In case of using PLC as a redundant system, this operates very well regardless some seconds of video degradation. This video degradation occurs to be at the moments when secondary link gets recovered from primary link. In case of using the load-sharing per packet mechanism the situation may change somehow. Although the idea of using the both links is desirable, there is needed more attention when a few technologies are used in combination, as latency and jitter are fundamental parameters for real-time applications.

REFERENCES

- [1] Marrocco G, Statovci D, and Trautmann S. A PLC Broadband Channel Simulator for Indoor Communications, International Symposium on Power Line Communications and Its Applications (ISPLC), pp. 321–326, March 2013.
- [2] FTW PLC Simulator, Online Available. <http://plc.ftw.at>.
- [3] Golden P, Dedieu H, and Jacobsen K. S. Fundamentals of DSL Technology, 1st ed. Auerbach Publications, July 2004.

- [4] IEEE Standard for Broadband over Powerline Networks. Medium access Control and Physical Layer Specifications, IEEE1901, pp. 1–1586, December 2010.
- [5] Andrea M. T, Fabio V. IEEE, Bottom-Up Statistical PLC Channel Modeling Part II: Inferring the Statistics, vol. 25, no. 4, pp. 2356–2363, October 2010.
- [6] Canete F.J, Diez L, Cortes J.A, Entrambasaguas J.T. Broadband modeling of indoor power-line channels, vol. 48, no. 1, pp. 175–183, February 2002.
- [7] IPTraf 3.0.0, National Center for Supercomputing, University of Illinois at Urbana-Champaign: <http://dast.nlanr.net/Projects/Iperf/>, September, 2005.
- [8] Wireshark network protocol analyzer, Wireshark® is available under the GNU General Public License version 2: <https://www.wireshark.org/>.

BIOGRAPHIES



ENVER HAMITI received Dipl. Ing. degree in Electronics and Telecommunications (1990), Mr.sc and Ph.D. in the field of Telecommunications, in 1999 respectively 2006 from the University of Prishtina, Faculty of Electrical and Computer Engineering. He was appointed as Associate Professor in the department of Telecommunications at the University of Prishtina, Faculty of Electrical and Computer Engineering, in 2010. His research interests cover the wide spectrum of wireless communications. In a particular he is interested in: antenna engineering, analytical and computational electromagnetics, microwave systems, modeling techniques for simulation of electromagnetic waves, electromagnetic field propagations and safe wireless and cellular communications. He has authored or co-authored many conference and journal papers.



TAULANT BERISHA received his BS and Msc degree in Electrical Engineering from the University of Prishtina, Faculty of Electrical and Computer Engineering in 2013. His research interests are in the broad area of wireless communications and networking.



FATOS PECI received his BS degree in Electrical Engineering from the University of Prishtina, Faculty of Electrical and Computer Engineering in 2007, while. Master's Science degree in Networking and Telecommunication Engineering at University of Pittsburgh. His research interests are in the broad area of wireless communications and networking, data structures, database systems.

Blending of Genetic Algorithm with Fletcher Reeves Method to Solve Reactive Power Problem

K. Lenin, B.R. Reddy, and M.S. Kalavathi

Abstract—In this study a hybrid algorithm - Fletcher Reeves method and advanced Genetic Algorithm (GA) are suggested to solve reactive power problem. In this approach, each of the G Fletcher Reeves method again with progressive operators are calculated step length. These approaches are extended to a set of multi-point access instead of single point approximation to avoid the convergence of the available method at local optimum and a new method, named Population Based Fletcher Reeves Method (PFR), are proposed to solve the reactive power problem. PFR was tested in standard IEEE 30 bus test system and simulation results demonstrate obviously about the best performance of the recommended algorithm in reducing the real power loss with control variables within the limits.

Index Terms—Hybrid Algorithm, Fletcher Reeves method, Genetic Algorithm, Bound Constrained Optimization problem, Global-optima, optimal reactive power, Transmission loss.

I. INTRODUCTION

TO till date various methodologies has been applied to solve the electrical reactive power problems. The key aspect of solving the reactive power problem is to reduce the real power loss with control variables are within the limits. Previously many type of mathematical methodologies like linear programming, gradient method [1-8] has been utilized to solve the electrical reactive power problem, but they lack in handling the constraints to reach a global optimization solution. In the Next level various types of Evolutionary algorithms [9-20] has been applied to solve the reactive power problem. But every algorithm has some merits and demerits. If one algorithm good in exploration but it lack in exploitation and another algorithm good in exploitation although it lack in exploration. Also some algorithm has poor speed in convergence. In the proposed method the step length of the Fletcher-Reeves method in each iteration is evaluated by GA. The above proposed concept is used to set initial points to overcome the problem of premature convergence. Proposed Population Based Fletcher Reeves Method (PFR) was tested in standard IEEE 30 bus test system and simulation study indicate the best performance of the proposed algorithm.

K.Lenin JNTU, Hyderabad,India , (e-mail: gklenin@gmail.com).

B.R. Reddy, JNTUA, Anantapur University in the field of Electrical Power Systems. (e-mail: bbumanapalli-brreddy@yahoo.co.in)

M.S. Kalavathi, Head of the electrical and electronics engineering department in JNTU, Hyderabad, India (e-mail: munagala.12@yahoo.co.in)

I. OBJECTIVE FUNCTION

A. Active power loss

The objective of the reactive power dispatch problem (RPDP) is to minimize the active power loss (APL) and can be defined in equations as follows:

$$F = PL = \sum_{k \in \text{Nbr}} g_k (V_i^2 + V_j^2 - 2V_i V_j \cos \theta_{ij}) \quad (1)$$

Where F- objective function, PL – power loss, g_k - conductance of branch, V_i and V_j are voltages at buses i, j , Nbr- total number of transmission lines in electric power systems.

B. Voltage profile improvement

To minimize the voltage deviation in PQ buses, the objective function can be written as:

$$F = PL + \omega_v \times VD \quad (2)$$

Where, VD - voltage deviation, ω_v - is a weighting factor of voltage deviation.

And the Voltage deviation given by:

$$VD = \sum_{i=1}^{N_{pq}} |V_i - 1| \quad (3)$$

C. Equality Constraint

The equality constraint of the problem is indicated by the power balance equation are given below:

$$P_G = P_D + P_L \quad (4)$$

Where the total power generation P_G has to cover the total power demand P_D and the power losses P_L .

D. Inequality Constraints

The inequality constraint implies the limits on components in the power system in addition to the limits created to make sure system security. Upper and lower bounds on the active power of slack bus (P_g), and electrical reactive power of generators (Q_g) are written as follows:

$$P_{g\text{slack}}^{\min} \leq P_{g\text{slack}} \leq P_{g\text{slack}}^{\max} \quad (5)$$

$$Q_{gi}^{\min} \leq Q_{gi} \leq Q_{gi}^{\max}, i \in N_g \quad (6)$$

Higher and lower bounds on the bus voltage magnitudes:

$$V_i^{\min} \leq V_i \leq V_i^{\max}, i \in N \quad (7)$$

Higher and lower bounds on the transformers tap ratios:

$$T_i^{\min} \leq T_i \leq T_i^{\max}, i \in N_T \quad (8)$$

Higher and lower bounds on the compensators it can be expressed by the following equation.

$$Q_c^{\min} \leq Q_c \leq Q_c^{\max}, i \in N_C \quad (9)$$

Where N is the total number of buses, NT is the total number of Transformers; Nc is the total number of shunt reactive compensators.

II. FLETCHER-REEVES METHOD

The well-known Fletcher –Reeves method is steepest descent method due to Cauchy is one of the oldest for solving unconstrained minimization problem [21]. In Fletcher- Reeves method, the key task is to find the optimal step length for getting the next better approximations of the decision variables in each iteration. Nearly all the scholars around the world utilized this approach in various applications .Here we are going to blend Genetic algorithm with Fletcher-Reeves to solve the reactive power problem.

III. GENETIC ALGORITHM

Genetic algorithms (GA), the most widely used unique method used in the solution of many problems. To unravel an optimization problem through GA, it is very obligation to plan a suitable chromosome representation of solution. There are dissimilar types [22.23] of acting between which binary and real coding representations are common. In binary coding demonstration each changeable is characterized as binary substrings with ideal precision. In this instance the string length of an isolated will be huge and GA would execute In the following sections. In real coding exemplification all chromosome vectors are encoded as a vector of floating point number of same length as the solution vector. This category of illustration is very elementary to handle and is proficient of representing very quiet large domains. In this exemplification a vector (x_1, x_2, \dots, x_n) is used as a single to represent a solution of the optimization problem. In the subsequent step is to initialize the chromosomes which will take part in the artificial genetic operations like natural genetics. In this way population size of chromosomes are formed in which each element is initially selected arbitrarily within the desired domain. Amongst many processes for selection of an arbitrary number, here we have used the uniform distribution method.

IV. POPULATION BASED FLETCHER-REEVES METHODOLOGY FOR SOLVING RECATIVE POWER PROBLEM

In this paper, a new methodology population based Fletcher Reeves method (PFR) by extending the inkling of single-point exploration to a multi-point exploration. The multiple approximations produce a series of paths among which at least one converges to the global optimum. In this technique of the study, all the chromosomes is upgraded by Fletcher Reeves

method whereas the step length is calculated by GA.

Algorithm

Step-1: Set $k = 0$

Step -2: produce an initial population $x^{(k)}$, by generating each component $x_i^{(k)}$ ($i = 1, 2, \dots, p_size$). (P_size denotes population size)

Step -3: Compute the function values $f(x_i^{(k)})$ for all i

Step -4: Find the best value of f from all $f(x_i^{(k)})$ come along with $x^{(k)}$ and keep it in $f_{old}^{(k)}$ and $x_{old}^{(k)}$

Step-5: Increase the value of k by unity i.e., $k = k+1$

Step-6: Set $i = 1$,

Step-7: Find the search direction $d_i^{(k-1)} = -\nabla f(x_i^{(k-1)})$

Step-8: Find the best found value of step length λ and store this value in $\lambda_i^{(k-1)}$

Step-9: Compute $x_i^{(k)} = x_i^{(k-1)} + \lambda_i^{(k-1)} d_i^{(k-1)}$

Step-10: Compute $d_i^{(k)} = -g_i^{(k)} + \beta_i^{(k-1)} d_i^{(k-1)}$, Where;

$$\beta_i^{(k-1)} = \frac{\langle g_i^{(k)}, g_i^{(k)} \rangle}{\langle g_i^{(k-1)}, g_i^{(k-1)} \rangle} \text{ and } g_i^{(k)} = \nabla f(x_i^{(k)})$$

Step -11: Compute the best found value of step length $\lambda_i^{(k)}$

Step-12: Improve the solution $x_i^{(k+1)} = x_i^{(k)} + \lambda_i^{(k)} d_i^{(k)}$

Step -13: Compute $f(x_i^{(k+1)})$

Step -14: Increase the value of i by unity i.e., $i = i+1$

Step -15: *if* $i < p_size$, *then go to step 7*

Step-16: Find the best value of f from all $f(x_i^{(k)})$ along with $x_i^{(k)}$ and store it in $f_{new}^{(k)}$ and $x_{new}^{(k)}$

Step-17: If the termination criterion is satisfied, go to step-19. Else, go to step-18,

Step -18: *if* $f_{new}^{(k)} < f_{old}^{(k)}$, *assign* $f_{old}^{(k)} = f_{new}^{(k)}$ *and* $x_{old}^{(k)} = x_{new}^{(k)}$ *and then go to step -5*

Step-19: Print the result and stop the process.

V. SIMULATION RESULTS

Validity of PFR algorithm has been verified by testing in IEEE 30-bus system, 41 branch system and it has 6 generator-bus voltage magnitudes, 4 transformer-tap settings, and 2 bus shunt reactive compensators. Bus 1 is taken as slack bus and 2, 5, 8,

11 and 13 are considered as PV generator buses and others are PQ load buses. Variables limits of the control are shows in Table I.

TABLE I
PRIME VARIABLE LIMITS (PU)

List of Variables	Min.	Max.	Type
Generator Bus	0.90	1.11	Continuous
Load Bus	0.91	1.01	Continuous
Transformer-Tap	0.92	1.01	Discrete
Shunt Reactive Compensator	-0.10	0.30	Discrete

In Table II the power limits of generators buses are listed.

TABLE II
GENERATORS POWER LIMITS

Bus	Pg	Pg _{min}	Pg _{max}	Qg _{min}
1	96.00	49	200	-19
2	79.00	18	79	-19
5	49.00	14	49	-11
8	21.00	11	31	-14
11	21.00	11	28	-12
13	21.00	11	39	-14

TABLE III
AFTER OPTIMIZATION VALUES OF CONTROL VARIABLES

Control Variables	PFR
V1	1.0501
V2	1.0408
V5	1.0206
V8	1.0305
V11	1.0702
V13	1.0507
T4,12	0.0000
T6,9	0.0100
T6,10	0.9000
T28,27	0.9100
Q10	0.1000
Q24	0.1000
Real power loss	4.2901
Voltage deviation	0.9091

Table III shows the proposed PFR approach successfully kept the control variables within limits.

Table IV list out the overall comparison of the results of optimal solution obtained by various methods.

TABLE IV
COMPARISON OF RESULTS

Techniques	Real power loss (MW)
SGA (24)	4.9800
PSO (25)	4.9262
LP (26)	5.9880
EP (26)	4.9630
CGA (26)	4.9800
AGA (26)	4.9260
CLPSO(26)	4.7208
HSA (27)	4.7624
BB-BC (28)	4.6900
PFR	4.2901

VI. CONCLUSION

In this paper, Population Based Fletcher Reeves method is efficaciously applied in order to solve Optimal RPDP. The projected PFR algorithm is tested in the standard IEEE 30 bus system operators. Simulation results show the strength of projected PFR methodology for providing improved optimal solution in diminishing the real power loss. Variables of the control obtained from after the optimization via PFR is within the limits.

REFERENCES

- [1] O. Alsac, and B. Scott, "Optimal load flow with steady state security", IEEE Transaction. PAS, pp.745-751, 1973.
- [2] K.Y. Lee, Y.M. Paru, J.L. Oritz –A united approach to optimal real and reactive power dispatch , IEEE Transactions on power Apparatus and systems, PAS-104, pp.1147-1153, 1985.
- [3] A.Monticelli , M .V.F Pereira ,and S. Granville , "Security constrained optimal power flow with post contingency corrective rescheduling" , IEEE Transactions on Power Systems, PWRS-2, no.1, pp.175-182,1987.
- [4] DeebN ,Shahidehpur S.M ,Linear reactive power optimization in a large power network using the decomposition approach. IEEE Transactions on power system, vol.5, no.2, pp.428-435, 1990.
- [5] E. Hobson ,'Network constrained reactive power control using linear programming, ' IEEE Transactions on power systems PAS -99 (4), pp 868-877, 1980
- [6] K.Y. Lee, Y.M Park, and J.L Oritz, "Fuel –cost optimization for both real and reactive power dispatches" , IEE Proc; 131C,(3), pp.85-93.
- [7] M.K. Mangoli, and K.Y. Lee, "Optimal real and reactive power control using linear programming", Electr.Power Syst. Res, vol.26, pp.1-10, 1993.
- [8] C.A. Canizares , A.C.Z.de Souza and V.H. Quintana, " Comparison of performance indices for detection of proximity to voltage collapse", vol. 11, no.3, pp.1441-1450, Aug 1996 .
- [9] S.R.Paranjothi ,andK.Anburaja, "Optimal power flow using refined genetic algorithm", Electr.PowerCompon.Syst, vol.30, pp.1055-1063, 2002.
- [10] D. Devaraj, and B. Yeganarayana, "Genetic algorithm based optimal power flow for security enhancement", IEE proc-Generation.Transmission and. Distribution; 152, 6 November 2005.
- [11] A.Berizzi, C. Bovo, M. Merlo, and M. Delfanti, "A ga approach to compare orpf objective functions including secondary voltage regulation," Electric Power Systems Research, vol.84, no.1, pp.187-194, 2012.
- [12] C.-F. Yang, G. G. Lai, C.-H. Lee, C.-T. Su, and G. W. Chang, "Optimal setting of reactive compensation devices with an improved voltage stability index for voltage stability enhancement," International Journal of Electrical Power and Energy Systems, vol.37, no.1, pp. 50 -57, 2012.
- [13] P. Roy, S. Ghoshal, and S. Thakur, "Optimal var control for improvements in voltage profiles and for real power loss minimization using biogeography based optimization," International Journal of Electrical Power and Energy Systems, vol.43, no.1, pp.830-838, 2012.
- [14] B. Venkatesh, G. Sadasivam, and M. Khan, "A new optimal reactive power scheduling method for loss minimization and voltage stability margin maximization using successive multi-objective fuzzy lp technique," IEEE Transactions on Power Systems, vol.15, no.2, pp. 844-851, may 2000.
- [15] W. Yan, S. Lu, and D. Yu, "A novel optimal reactive power dispatch method based on an improved hybrid evolutionary programming technique," IEEE Transactions on Power Systems, vol. 19, no. 2, pp. 913 – 918, may 2004.
- [16] W. Yan, F. Liu, C. Chung, and K. Wong, "A hybrid genetic algorithminterior point method for optimal reactive power flow," IEEE Transactions on Power Systems, vol.21, no.3, pp.1163-1169, Aug. 2006.

- [17] J. Yu, W. Yan, W. Li, C. Chung, and K. Wong, "An unfixed piecewiseoptimal reactive power-flow model and its algorithm for ac-de systems," IEEE Transactions on Power Systems, vol.23, no.1, pp. 170-176, Feb. 2008.
- [18] F. Capitanescu, "Assessing reactive power reserves with respect to operating constraints and voltage stability," IEEE Transactions on Power Systems, vol.26, no.4, pp.2224–2234, nov.2011.
- [19] Z. Hu, X. Wang, and G. Taylor, "Stochastic optimal reactive power dispatch: Formulation and solution method," International Journal of Electrical Power and Energy Systems, vol.32, no.6, pp.615-621, 2010.
- [20] Kargarian, M. Raoufat, and M. Mohammadi, "Probabilistic reactive power procurement in hybrid electricity markets with uncertain loads," Electric Power Systems Research, vol.82, no. , pp. 68-80, 2012.
- [21] Li Zhang, Weijun Zhou , Donghui Li, "Global convergence of a modified Fletcher–Reeves conjugate gradient method with Armijo-type line search", Numerische Mathematik, October 2006, vol.104, no.4, pp.561-572
- [22] K. Deb, A. Anand, and D. Joshi, A computationally efficient evolutionary algorithm for realparameter optimization. Evolutionary computation, Vol.10, No.4, pp.371-395, 2002.
- [23] K. Deb, and M.Thakur, A new crossover operator for real coded genetic algorithms. Applied Mathematics and Computation, vol.188(1), pp.895-911, 2007.
- [24] Q.H. Wu, Y.J.Cao, and J.Y. Wen. Optimal reactive power dispatch using an adaptive genetic algorithm. Int. J. Elect. Power Energy Syst. vol 20. pp.563-569, Aug 1998.
- [25] B. Zhao, C. X. Guo, and Y.J. CAO. Multiagent-based particle swarm optimization approach for optimal reactive power dispatch. IEEE Trans. Power Syst. Vol.20, no.2, pp.1070-1078, May 2005.
- [26] Mahadevan. K, Kannan P. S. "Comprehensive Learning Particle Swarm Optimization for Reactive Power Dispatch", Applied Soft Computing, Vol.10, No.2, pp.641–52, March 2010.
- [27] A.H. Khazali, M. Kalantar, "Optimal Reactive Power Dispatch based on Harmony Search Algorithm", Electrical Power and Energy Systems, vol.33, no.3, pp.684-692, March 2011.
- [28] S. Sakthivel, M. Gayathri, V. Manimozhi, "A Nature Inspired Optimization Algorithm for Reactive Power Control in a Power System", International Journal of Recent Technology and Engineering (IJRTE) , vol.2, no.1, pp.29-33, March 2013.

BIOGRAPHIES



Kanagasabai Lenin has received his B.E., Degree, electrical and electronics engineering in 1999 from university of madras, Chennai, India and M.E., Degree in power systems in 2000 from Annamalai University, TamilNadu, India. Presently pursuing Ph.D. degree at JNTU, Hyderabad, India.



Bhumanapally Ravindhranath Reddy, Born on 3rd September, 1969. Got his B.Tech in Electrical & Electronics Engineering from the J.N.T.U. College of Engg., Anantapur in the year 1991. Completed his M.Tech in Energy Systems in IPGSR of J.N.T.University Hyderabad in the year 1997. Obtained his doctoral degree from JNTUA, Anantapur University in the field of Electrical Power Systems. Published 12 Research Papers and presently guiding 6 Ph.D. Scholars. He was specialized in Power Systems,

High Voltage Engineering and Control Systems. His research interests include Simulation studies on Transients of different power system equipment.



M. Surya Kalavathi has received her B.Tech. Electrical and Electronics Engineering from SVU, Andhra Pradesh, India and M.Tech. power system operation and control from SVU, Andhra Pradesh, India. She received her Ph.D. Degree from JNTU, Hyderabad and Post doc. From CMU – USA. Currently she is Professor and Head of the electrical and electronics engineering department in JNTU, Hyderabad, India and she has Published 16 Research Papers and presently guiding 5 Ph.D. Scholars.

She has specialized in Power Systems, High Voltage Engineering and Control Systems. Her research interests include Simulation studies on Transients of different power system equipment. She has 18 years of experience. She has invited for various lectures in institutes.

Design of a MRAS, Speed and Flux Estimators used in Sensorless Control of Induction Motors

N. Ben Si Ali and N. Benalia

Abstract— Model reference adaptive system (MRAS) based techniques are one of the best methods to estimate the rotor speed. Speed and torque control of an induction motor is usually attained by application of a speed or position sensor. However, these require the additional mounting space, reduce the reliability and increase the cost of the motor. The recent trend in field oriented control (FOC) is towards the use of sensorless techniques that avert the use of speed sensor and flux sensor. This paper seeks to provide a direct comparison between two technics of induction motor MRAS based speed estimators, one based on the rotor flux and the other based on the back EMF. Comparison between the two techniques is made through computer simulations.

Keywords- Induction motor drive, adaptive observer, MRAS, stability analysis.

I. INTRODUCTION

MODEL Reference Adaptive System (MRAS) represents one of the most attractive and popular solutions for sensorless control of induction motor drives. Many electronic drivers for the induction motor control are based on sensorless technologies. Adaptive observers introduced by [1,2] were a powerful prolongation of initial sensor based observers.

The MRAS approach has the immediate advantage in that the model is basic and very easy to practice. The most common MRAS structure is that based on the rotor flux error vector [3] that provides the advantage of producing rotor flux angle forecast for the field orientation plan. Other MRAS structures have also been proposed recently that use the back EMF and the reactive power as the error vectors estimators [4,5].

In this paper two methods of MRAS based speed estimators are proposed. One based on rotor flux estimation and the second based on back EMF estimation.

N. Ben Si Ali, Department of Electrical Engineering, Badji Mokhtar university, Annaba, Algeria, (e-mail: bensialin@yahoo.fr)

N. Benalia, Department of Electrical Engineering, Badji Mokhtar university, Annaba, Algeria, (e-mail benalianadia13@yahoo.com)

II. MACHINE MODELLING

Basic equations of induction motor in a general reference frame in terms of complex space vector quantities are [6]:

$$\underline{u}_s = R_s \underline{i}_s + \frac{d}{dt} \underline{\psi}_s + j\omega_s \underline{\psi}_s \quad (1a)$$

$$0 = R_r \underline{i}_r + \frac{d}{dt} \underline{\psi}_r + j(\omega_s - \omega) \underline{\psi}_r \quad (1b)$$

Where:

$\underline{u}_s = u_{sd} + ju_{sq}$: Stator voltage vector

$\underline{i}_s = i_{sd} + ji_{sq}$: Stator current vector

$\underline{i}_r = i_{rd} + ji_{rq}$: Rotor current vector

$\underline{\psi}_r = \psi_{rd} + j\psi_{rq}$: Rotor flux vector

$\underline{\psi}_s = \psi_{sd} + j\psi_{sq}$: Stator flux vector

L_s, L_r, L_m : Stator, rotor and mutual inductance respectively.

R_s, R_r : Stator and rotor resistance

$\sigma = 1 - \frac{L_m^2}{L_s L_r}$: Leakage coefficient

ω_s, ω are the stator angular frequency, the motor angular velocity respectively.

The stator and rotor flux linkages are:

$$\underline{\psi}_s = L_s \underline{i}_s + L_m \underline{i}_r \quad (2a)$$

$$\underline{\psi}_r = L_r \underline{i}_r + L_m \underline{i}_s \quad (2b)$$

Under the rotor flux orientation conditions (FOC) the rotor flux is aligned on the d-axis. The electromagnetic torque equation is:

$$T_{em} = \frac{3}{2} p \frac{L_m}{L_r} \psi_r i_{sq} \quad (3)$$

The bloc diagram of sensorless indirect field oriented control induction motor drive is indicated on Fig.1.

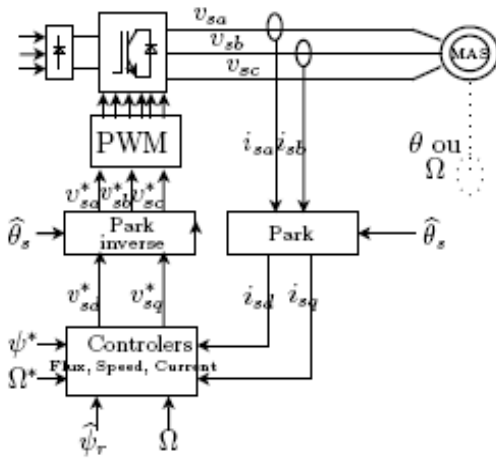


Fig.1. Block diagram of RFOC IM simulator

III. MODEL REFERENCE ADAPTIVE SYSTEM

There are three approaches developed in literature of MRAS based speed estimators [7]:

- The rotor flux error based MRAS scheme
- The back EMF error based MRAS scheme
- Stator current error based MRAS scheme

The model reference approach (MRAS) makes use of two machine models of different structures that estimate the same state variable on the basis of different sets of inputs variables [3]. MRAS estimators consist of a reference model (which does not include the speed estimate) and an adjustable model (which include the speed estimate).

IV. MRAS BASED ON ROTOR FLUX ESTIMATION

In this approach, reference model is the voltage model it's the induction motor model. Its equation is derived from (1) and (2). In the stationary reference frame ($\omega_s = 0$), so:

$$\underline{\psi}_{-rv} = \int \left(\underline{u}_{-s} R_s i_{-s} - \sigma L_s \frac{d}{dt} i_{-s} \right) dt \quad (4)$$

The adjustable model is the current model its equation is obtained from (1b) and (2)

$$\frac{d}{dt} \underline{\psi}_{-ri} + \frac{1}{T_r} \underline{\psi}_{-ri} = j \hat{\omega} \underline{\psi}_{-ri} + \frac{L_m}{T_r} i_{-s} \quad (5)$$

Model (5), generates the rotor flux estimate from the measured stator current and from the estimated speed ($\hat{\omega}$) which is obtained through a PI controller from an error signal ϵ . This error represents difference between the two estimated flux vectors.

Where $\underline{\psi}_{-rv}$ the rotor flux estimated by the reference model (voltage model), and $\underline{\psi}_{-ri}$ is the rotor flux estimated by the adjustable model (current model).

Fig.2 illustrates the basic structure of rotor flux based MRAS approach.

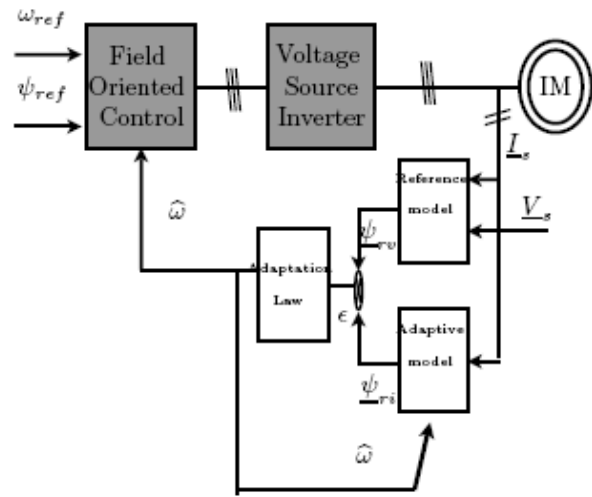


Fig.2. Block diagram of rotor flux MRAS method

A. ADAPTATION LAW

From model (4), rotor flux is

$$\frac{d}{dt} \underline{\psi}_{-r} = \left(-\frac{1}{T_r} + j\omega \right) \underline{\psi}_{-r} + \frac{L_m}{T_r} i_{-s} \quad (6)$$

From model (5), estimated rotor flux is

$$\frac{d}{dt} \hat{\underline{\psi}}_{-r} = \left(-\frac{1}{T_r} + j\hat{\omega} \right) \hat{\underline{\psi}}_{-r} + \frac{L_m}{T_r} i_{-s} \quad (7)$$

System describing estimation error is

$$\frac{d}{dt} \underline{e}_{-\psi} = \left(-\frac{1}{T_r} + j\omega \right) \underline{e}_{-\psi} + j(\omega - \hat{\omega}) \hat{\underline{\psi}}_{-r} \quad (8)$$

It's important to ensure system (8) stability. It's guaranteed if error ϵ tend to zero. The adaptation law is obtained from Lyapunov theory [1].

The estimated speed expression can be written as:

$$\hat{\omega} = \left(K_p + \frac{K_i}{s} \right) \epsilon \quad (9)$$

With:

$$\varepsilon = \Im(\psi_r \hat{\psi}'_r) = \psi_{r\beta} \hat{\psi}'_{r\alpha} - \psi_{r\alpha} \hat{\psi}'_{r\beta}$$

Figures (3), (4) are obtained with nominal torque $T_{Lo} = 7 (N.m)$ applied at $t=2s$. Fig.3 indicates the system behavior during steady state condition at high speed (150 rad/s) and during transient with speed inversion. Fig.4 shows the system performance in the low speed region (10 rad/s).

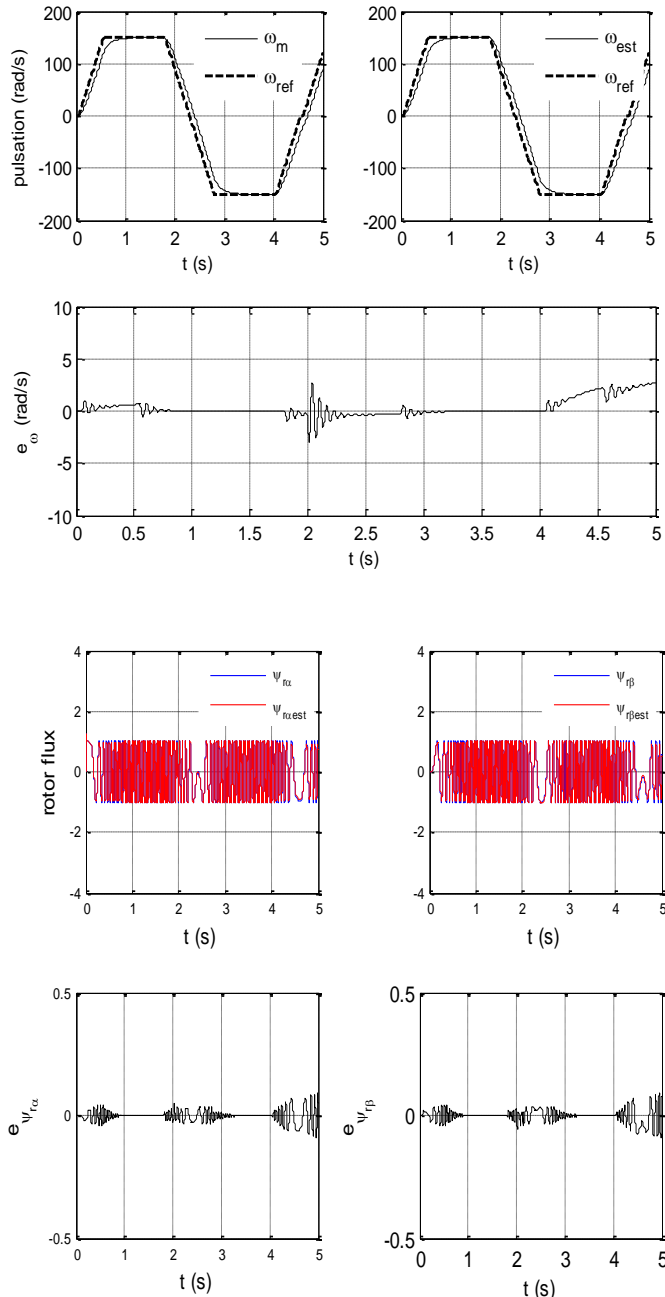


Fig. 3. Four quadrant operation at high speed for $K_p = 10, K_i = 10000$

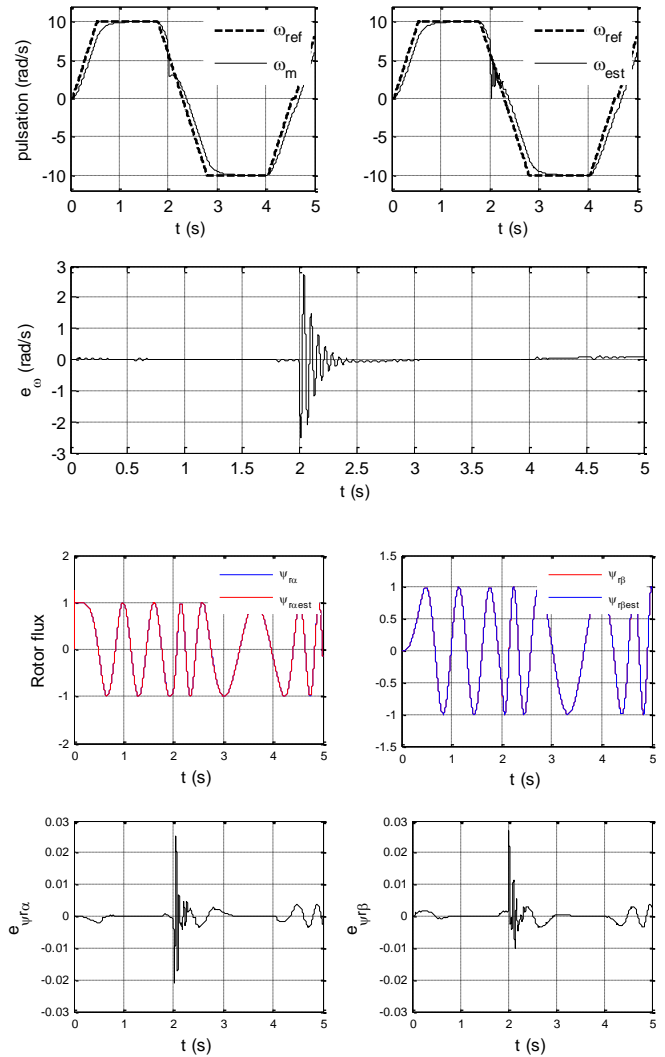


Fig.4. Four quadrant operation at low speed for $K_p = 10, K_i = 10000$

Simulation results indicate that the fluxes of the adjustable model converge to the reference fluxes, the speed prediction has small or no steady-state error and the dynamics of the speed estimate is acceptable. Generally, the classical MRAS works very well if ideal integration can be used in both models. Nevertheless, in a real system, pure integration cannot be implemented.

V. MRAS BASED ON BACK EMF ESTIMATION

The primary method suffers from problems associated with pure integration. To avoid the problems, an MRAS based on back EMF is proposed. The rotor speed is generated from an error signal calculated by the dot product of the stator current vector and the back EMF difference vector [7,8].

The reference model is derived from (4):

$$\frac{d}{dt} \psi_{rv} = \frac{L_r}{L_m} (u_s - R_s i_s - \sigma L_s \frac{d}{dt} i_s) = E_v \quad (10)$$

The adjustable model is derived from Eq. (5)

$$\frac{d}{dt} \hat{\psi}_{-ri} = \left(-\frac{1}{T_r} + j\hat{\omega}\right) \hat{\psi}_{-ri} + \frac{L_m}{T_r} i_s = \hat{E}_i \quad (11)$$

The adaptive law of the estimator is given by [7]:

$$\hat{\omega} = \left(K_p + \frac{K_i}{s}\right) \varepsilon \quad (12)$$

With:

$$\varepsilon = (j i_s)^T \Delta \underline{E}_{vi} \quad (13)$$

$\Delta \underline{E}_{vi} = \underline{E}_v - \hat{\underline{E}}_i$: It's the back EMF difference vector.

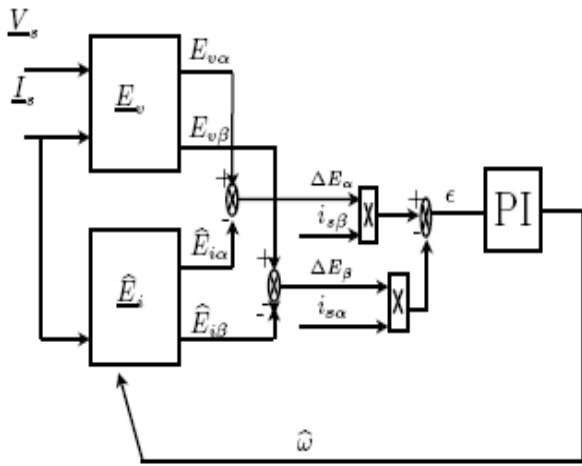


Fig. 5. Block diagram of back EMF based approach

Fig.5 indicates the block diagram of the proposed MRAS based on back EMF calculation. For this case simulations are done for different operating points in monitoring and regenerating modes Fig.6.

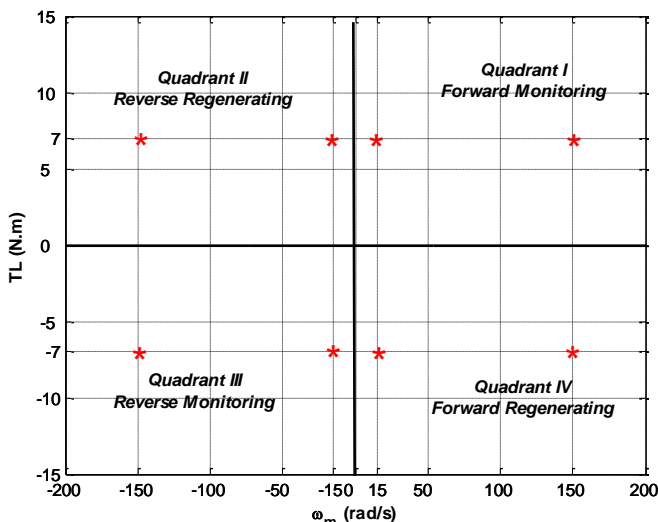


Fig.6. Operating points in the torque speed plane

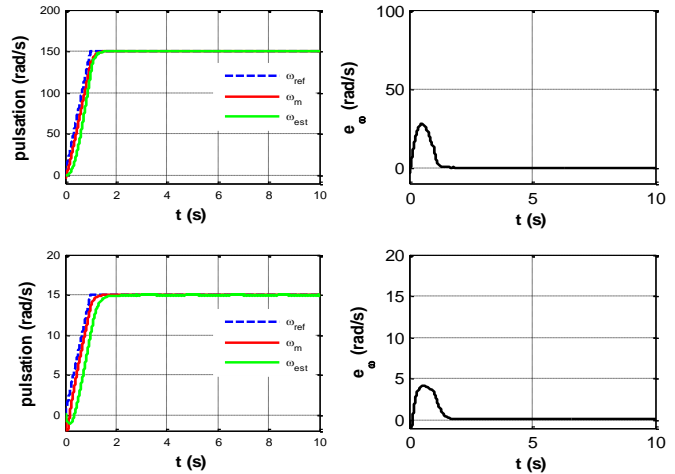


Fig. 7. Quadrant I Forward monitoring mode: reference speeds $\omega_{ref} = 150(\text{rad/s})$, $\omega_{ref} = 15(\text{rad/s})$ and load torque $T_{Lo} = 7(\text{N.m})$

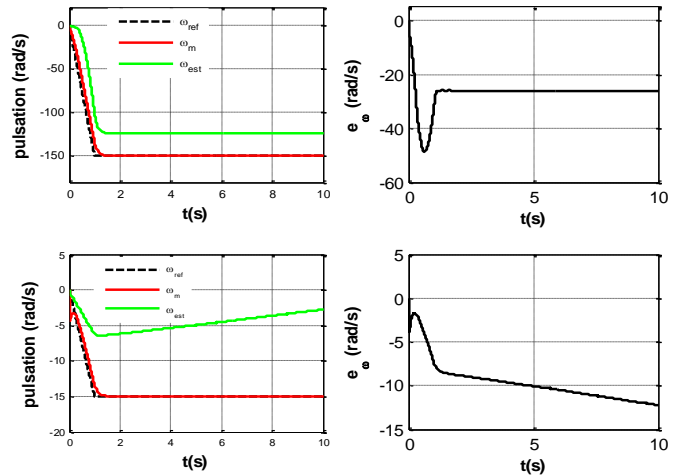


Fig.8. Quadrant II Reverse regenerating mode: reference speeds $\omega_{ref} = -150(\text{rad/s})$, $\omega_{ref} = -15(\text{rad/s})$ and load torque $T_{Lo} = 7(\text{N.m})$

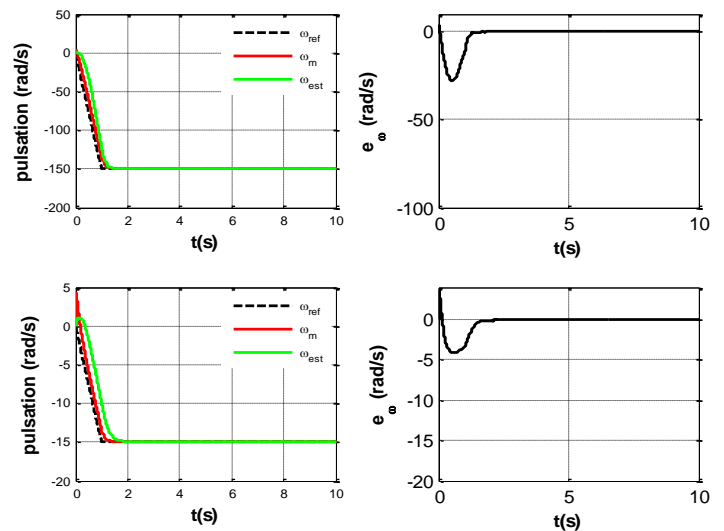


Fig.9. Quadrant III Reverse monitoring mode: reference speeds $\omega_{ref} = -150(\text{rad/s})$, $\omega_{ref} = -15(\text{rad/s})$ and load torque $T_{Lo} = -7(\text{N.m})$

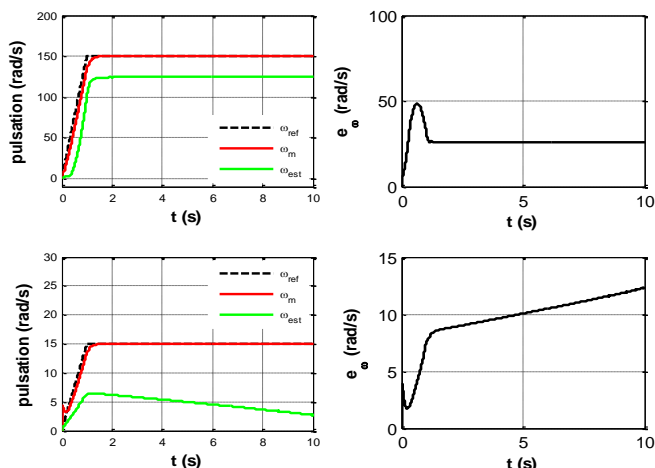


Fig.10. Quadrant IV Forward regenerating mode: reference speeds $\omega_{ref} = 150(\text{rad/s})$, $\omega_{ref} = 15(\text{rad/s})$ and load torque $T_{Lo} = -7(\text{N.m})$

Fig.7 and Fig.9 shows the system behavior for high and low speed drive. It can be seen that in monitoring mode (Quadrant I and Quadrant III), estimated speed converge to real rotor speed, speed error tend to zero. Fig.8 and Fig10 show that divergence is highlighted between real speed and estimated speed. Stability of this system is not guaranteed in regenerating mode (Quadrant II and Quadrant IV).

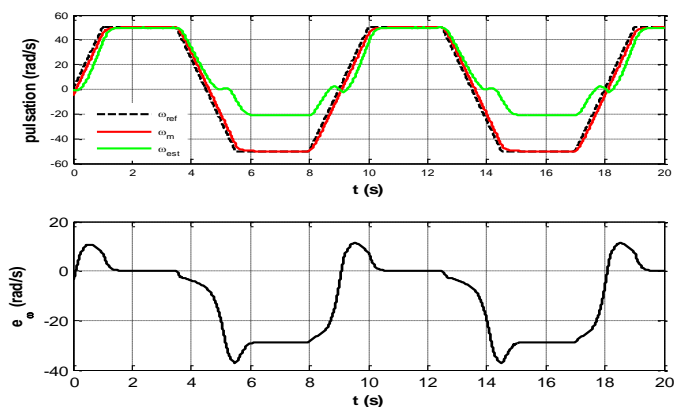


Fig.11. Reversing speed operation: $\omega_{ref} = 50(\text{rad/s})$ to $\omega_{ref} = -50(\text{rad/s})$

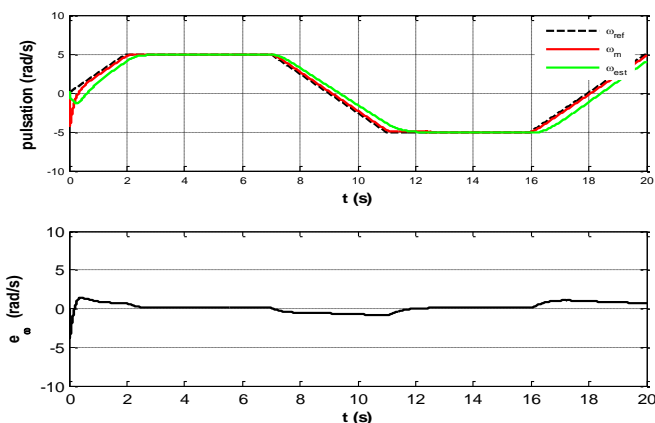


Fig.12. Reversing speed operation: $\omega_{ref} = 5(\text{rad/s})$ to $\omega_{ref} = -5(\text{rad/s})$

Dynamic performances were tested during transient with speed inversion from $\omega = 50(\text{rad/s})$ to $\omega = -50(\text{rad/s})$ (Fig.11) and from $\omega = 5(\text{rad/s})$ to $\omega = -5(\text{rad/s})$ (Fig.12) under nominal torque $T_{Lo} = 7(\text{N.m})$. Results obtained confirm that system is stable in monitoring mode and unstable for zero speed and unstable in regenerating mode but not for all operating points in torque speed plane.

For $\omega_{ref} = -50(\text{rad/s})$ and load torque $T_{Lo} = 7(\text{N.m})$ system is unstable (figure 11). For $\omega_{ref} = -5(\text{rad/s})$ and load torque $T_{Lo} = 7(\text{N.m})$ system is stable (Fig.12).

V. CONCLUSIONS

MRAS based on rotor flux estimation had well tracking performances at high speed and even at low speed operation. Estimated and measured speeds, are equal each other not only for the steady-state operation but also under speed reference and load torque changes but pure integration process causes drift problems. MRAS based on back EMF estimation approach can be easily practiced but it suffers from instabilities in re-generating mode. The sensorless control based on back EMF degrades fast at low speed, at zero speed. To ensure good behavior, first stability analysis must be done to know unstable zones then adaptation law will be modified to have good tracking performances.

ACKNOWLEDGMENT

The study is selected from 1st International Conference on Electrical Energy and Systems October 22-24th.

REFERENCES

- [1] H. Kubota and K. Matsuse, " DSP-Based Speed Adaptive Flux Observer of Induction Motor", IEEE Transactions on Industry Applications, vol. 29, no.2, 1993.
- [2] C. Schauder, "Adaptive speed identification for vector control of Induction Motor without rotational transducers", in Conf. Rec. IEEE IAS Annu. Mtg., p. 493-499, 1988.
- [3] J. Holtz, "Methods for Speed Sensorless Control of AC Drives", Published i K. Rajashekara (editor) Sensorless Control of AC Motors. IEEE press book. 1996.
- [4] M. Rashed and F. Stronach, "A stable MRAS-based sensorless vector control induction motor drive at low speeds", in Conf. Rec. IEEE IEMDC, 2003.
- [5] M. Suman and C. Chakraborty, "Model Reference Adaptive Controller-Based Rotor Resistance and Speed Estimation Techniques for Vector Controlled Induction Motor Drive Utilizing Reactive Power", IEEE Transactions on industrial electronics, vol.55, no.2, 2008.
- [6] C. Chaigne, E. Etien, S. Cauet, L. Rambault, "Commande vectorielle sans capteur des machines asynchrones", Hermes science, Lavoisier, 2005.
- [7] N. Marwali and A. Keyhani, "Comparative Study of Rotor Flux Based MRAS and Back EMF Based MRAS Speed Estimators for Speed

Sensorless Vector Control of Induction Machines”, IEEE Industry Applications Society Annual Meeting, New Orleans, Louisiana, 1997.

- [8] M. Rashed and F. Stronach and P. Vas, “A stable back EMF MRAS-based sensorless low speed induction motor drive insensitive to stator resistance variation”, IEE Proc-Electr, Power Appl, vol.151, no.6, 2004.

BIOGRAPHIES



NADIA BEN SI ALI was born in Annaba in Algeria. She received the engineering and DEA. Degrees from Badji Mokhtar Annaba University, Algeria in 1994 and 1997 respectively. She obtained the Ph.D. degree in 2008 from Badji Mokhtar Annaba University, Algeria. She is with the electrical Engineering Department of the same university. Her fields of research are electrical power converters and sensorless control of motors drive.



NADIA BENALIA was born in Annaba in Algeria. She received the engineering and DEA. Degrees from Badji Mokhtar Annaba University, Algeria in 1993 and 1996 respectively. She obtained the Ph.D. degree in 2010 from Badji Mokhtar Annaba University, Algeria. She is with the electrical Engineering Department of the same university. Her fields of research are optimization using genetic algorithms and stability of electrical networks.

Laboratory SCADA Systems – the State of Art and the Challenges

S. Lishev, R. Popov, and A. Georgiev

Abstract— The present review considers the hardware and control system structure of the modern SCADA systems. The commonly used communication infrastructure and data transmission protocols are described. Especially the trends in using wireless communication technology applications are analyzed. A number of different SCADA system applications are represented and its advantages and disadvantages are also discussed.

Index Terms— SCADA systems, remote laboratory, wireless data network, communication protocols.

I. INTRODUCTION

SUPERVISORY Control and Data Acquisition Systems, known as SCADA systems, belong to the group of systems for management of processes with the name - Industrial Control Systems - ICS and are used to manage geographically dispersed sites, which are scattered thousands of square kilometers. They can be pipelines, water supply systems, power lines, railway transport, and various production and experimental systems. An essential characteristic is the requirement for reliable real-time management. SCADA systems can be of varying degree of complexity depending on the controlled process and the specific implementation [1,2].

During last years the SCADA systems are commonly used in the field of scientific investigation process, where more and more complex systems are examined. The R&D in this field adds challenges and specific requirements to measurement, monitoring and control system, used under installation tests.

II. THE STRUCTURE OF THE SCADA SYSTEMS

A. Hardware and communication architecture

Despite all the differences SCADA systems share a common structure related to the different units and their functions. Management actions related to the production process are performed by remote terminals (Remote Terminal

S. Lishev is with the Department of Optoelectronics and Laser Engineering, Technical University of Sofia, Branch Plovdiv, Bulgaria (e-mail: stefan_lishev@abv.bg).

R. Popov is with the Department of Electronics, Communications and Information Technologies, Plovdiv University “Paisii Hilendarski”, Bulgaria (e-mail: rum_pop@yahoo.com).

A. Georgiev is with the Department of Mechanics, Technical University of Sofia, Branch Plovdiv, Bulgaria (e-mail: AGeorgiev@gmx.de).

Units or RTU), PLCs (Programmable Logic Controllers or PLC) and intelligent electronic devices (IED - Intelligent Electronic Device) in automatic mode, which transmit telemetry data to the system and/or change the state of the objects based on the control messages. RTU devices communicate with the MTU (Master Terminal Unit), which has a direct connection to the HMI (Human Machine Interface). By the HMI the parameters of the managed process are monitored, the measured values are archived and new control values are issued if needed [3,4]. The overall structure is presented in Fig. 1.

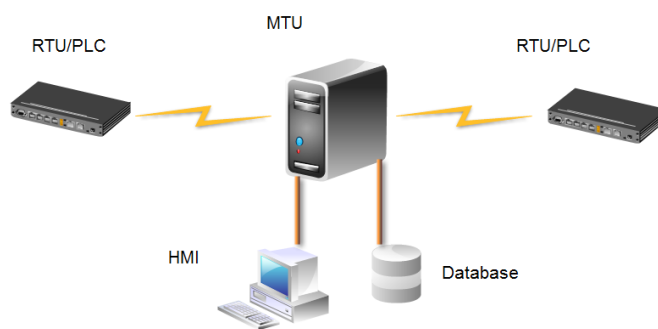


Fig. 1 Common structure of SCADA system

The MTU monitor and control the entire information flow in the SCADA system and by HMI provides convenient human-machine interface [5]. MTU manages all related remote terminals that can be located physically on a large area. In modern SCADA systems it is always based on computer on which operates specialized SCADA software. It may consist of a group of servers, where each one performs a different part of the task – database connection, communication with the RTU devices, communication and user interface and etc. MTU can monitor and manage the process, even when the operator is missing. This is achieved by incorporating a schedule of commands and actions that to be carried out in the process management [3].

RTU devices interact directly with controlled process in real time via a link with thermometers, level meters, valves, actuators and other sensors and devices that have a direct connection with the physical processes. By them the remote terminals perform the basic tasks - management and data collection. RTU devices usually have no information on what they measure - they follow the control commands of the main terminal and sent information of the result [6]. Communication with the various sensors and actuators is done through serial protocols - RS485, Industrial Ethernet and others that are using various media as a physical layer - copper

cable - twisted pair, coaxial cable or optical fiber. Often are used wireless protocols - ZigBee, Wi-Fi [7,8]. Most RTU devices store collected information in memory and wait for request from the main terminal to send it. Management instructions are usually stored locally because of the limited speed of the communication with the MTU device. These instructions are usually placed in programmable logic controllers, which in the past were separated from RTU devices. Over time, the border between them has languished and terms have become interchangeable [9].

The HMI is used to monitor and control the managed process by human. It consists of one or many computer terminals connected to the main terminal MTU by the network, which provide a suitable interface for management - monitors, keyboards, mice and etc. Specialized software for SCADA is used, which ensures an intuitive visualization of the managed process, so that the operator can quickly respond in case of emergency or other extreme event. The basic requirements for human-machine interface are to provide global visibility of the managed process, information on its progress, and to allow monitoring to be carried out at different levels of abstraction. Alarms and error messages and deviations from norms are an important part of the functions of the HMI [10].

An important part of the structure of the SCADA system is the medium of communication between server and RTU devices. It can be realized through cable, telephone or radio. Primary requirement is to be "transparent" - link-level abstraction of commands and responses should not depend on whether an RTU device is connected via cable or radio.

B. SCADA control systems architecture

It could be distinguished three main ways of connecting different units in terms of how to implement management [7]:

- local control;
- centralized control;
- distributed control.

The first type of control is done locally and the controller manages the process, sensors and actuators. It has a human machine interface that can be used to set control parameters and to monitor various parameters of the process. The connection to the supervisor level serves for simple commands to start/end or change a parameter, and sending status information and alarms. This type of management is usually used for simple systems.

In the second type the sensors and actuators are connected to the control room, where are located the MTU, HMI and all other units. The advantage of this architecture is that the operator can monitor and manage the entire system from one place and can react quickly in case of emergency. The disadvantage is the high price because connections to the sensors and actuators in the managed process must be duplicated, and the main controller has to ensure the sustainability of the system to accidents. This type of management has been used in the past, but now is rarely used.

The third type of architecture - distributed control, is one of the most commonly used because it combines the advantages of the other two. Controllers that perform control are near the managed process, but are connected by a network to a central

controller in the control room. It receives a full management information and can change individual parameters and the entire algorithm and sequence of control. This type of architecture has a high degree of reliability because a fault in a controller does not affect the work of others and also individual controllers can continue to operate in case of loss of connection with the master terminal. The disadvantage of such systems is security, because it can be made intrusion in the algorithm of operation if it is used the global network. Therefore, if using this architecture, it is required to take special actions to protect from intrusion.

III. COMMUNICATION PROTOCOLS

Protocols for communication between different parts of a SCADA system are essential to the functionality and reliability of the system. Various protocols define the rules and scheme of communication between remote terminals and the main terminal - commands MTU-RTU, status information, presentation and transformation of data, setting the addresses of remote terminals, monitoring and control. Protocols for SCADA systems are designed to be compact [4]. Typically used model is "master/slave" - remote terminals wait for command or query for status and then send a reply. In some cases, they can send messages on its own initiative - when there is a failure of the sensor, actuator, or other emergency situation [5]. For this reason, each protocol consists of two parts - the format of the messages from MTU to RTU devices, and format of the messages in the opposite direction - RTU-MTU. Mainly are used Internet-based protocols [6].

Some of the most frequently used protocols are [5]:

A. Modbus

Modbus is an entirely open serial protocol that is widely used for industrial automation [11]. In terms of the OSI model is the 7th level - application layer. It provides client-server communication between devices connected to different networks. When used on the TCP/IP stack data exchange is carried out through port 502 [12]. Modbus is suitable in cases where the transfer rate is low.

B. DNP3

DNP3 (Distributed network protocol) protocol is based on the three-layer model EPA (Enhanced Performance Architecture) to effectively connect IED in SCADA systems. It can be used to exchange messages between IED and RTU, and between the RTU and the main terminal. It is characterized by that it ensures high data integrity, has a flexible structure and a small amount of overhead. For this reason it can be used in a low-speed connection with a speed even of 1200 b/s. Most often it is specified on physical layer such as RS-232 or RS-485, using copper wire, optical fiber, radio or satellite. Newer implementations use an Ethernet connection [12].

C. IEC 60870-5

Protocol proposed by the International Electrotechnical Commission - IEC to be used in the electrical industry, but is also used in other industries. Fully open protocol for controlling processes that are distributed on a large territory controlled by SCADA systems - Telemetry and Control [13].

D. Profibus

It is based on the model master/slave, where the master device sends periodic queries to slave devices, and they should answer in the given time. Profibus supports more than one master device, because the right of access is given from one master device to the next [13].

E. Foundation Fieldbus

It is a protocol designed for communication in the field between networked devices - sensors, actuators, PLC controllers, drives and human-machine interfaces [14].

F. CANopen

The communication protocol of high level is based on CAN (Controller Area Network) protocol. It is designed for embedded systems, mainly automobiles and industrial systems, where there is movement. In terms of the OSI model it implement the above five layers - network, transport, session, application and presentation layer. The lower two - physical and data link are realized by CAN protocol [15]. In SCADA systems is used to connect sensors and actuators to PLC / RTU controllers.

In recent years a set of new protocols are implemented for use in SCADA systems. Most of them are developed on the basis of the existing telecommunication network protocols, such as TCP/IP, GPRS, 3G/4G mobile network data exchange protocols, WiFi network protocols, low range data transmission wireless protocols ZigBee, Bluetooth, e.c.t.

IV. OVERVIEW OF THE EXISTING SCADA SYSTEMS - HARDWARE AND SOFTWARE TOOLS

The general concept of SCADA systems can be implemented in different ways according to the specific needs and requirements. We will look at various hardware and software tools in relatively simple systems, such as research laboratories with remote access, as well as more complex industrial applications. There are realized tree of the most commonly implemented in recent years approaches:

- PC – PLC approach;
- PLC WEB server approach
- PC – DAQ board or embedded control board approach.

The any combination of these approaches is also usefull.

A. PC – PLC approach

A commonly used approach is – an industrial computer with SCADA software, connected to PLC controllers, which control the physical process. The control functions are performed locally, by PLC and supervisory level sets the parameters of control and collects the results.

In [16] a system for laboratory remote access is described. It consisting of a couple of PLC Siemens S7-200, connected through CAN bus to a computer, on which operates LabVIEW™ [17] software. The structure of a remote-controlled laboratory is shown on Fig. 2. Two experimental setups are connected to the PLC controllers – an elevator experimental platform and a screw experimental platform. Each PLC has the capability to expand functionality through additional modules – they can support protocols such as PROFIBUS, RS485 and Industrial Ethernet. The computer is

equipped with interface module ZLG CAN PCI-5110 for CAN connection, and PLC controllers are connected via their RS485 port to an intelligent interface converter CAN485MB. Control instructions are located in the PLC. The capabilities of LabVIEW software to generate HTML pages from the front panel of virtual instruments allow remote Web access to control parameters.

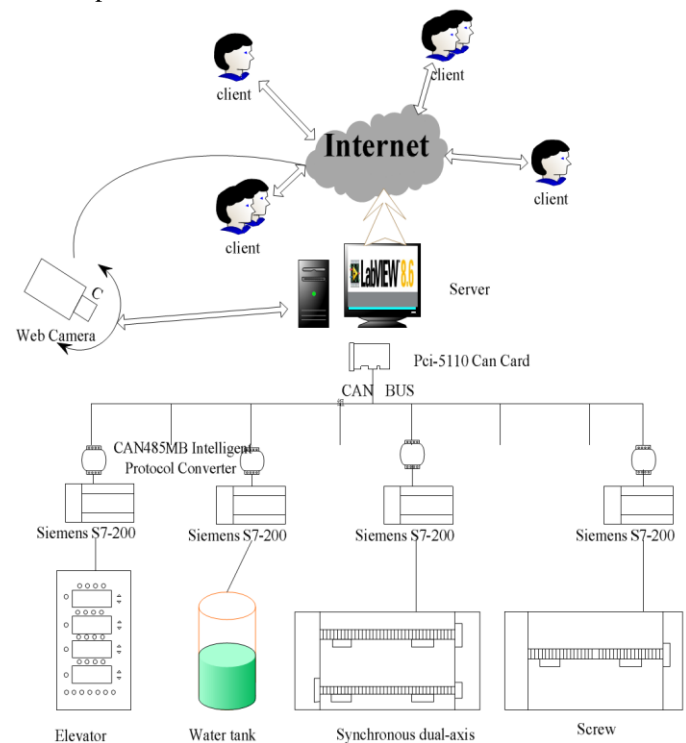


Fig. 2 Structure of a remote-controlled laboratory - source [16]

In [18] is offered a similar solution for Web-based laboratory for experiments - devices that are managed are 3-phase induction motor, position encoder and magnetic powder brake. The system (Fig. 3) has a local control, but allows remotely changing the operating points and the algorithm that is used.

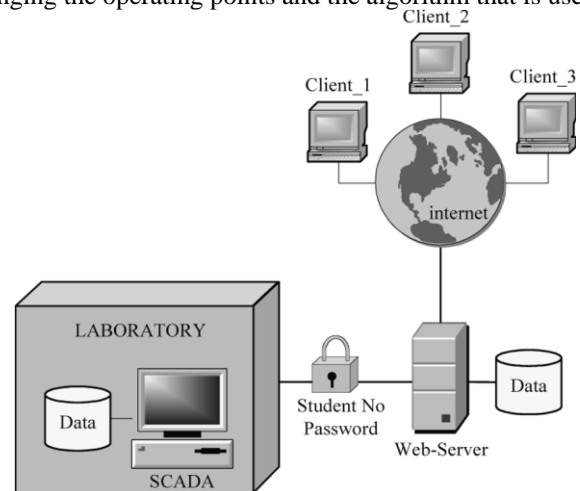


Fig. 3 Web-based remote laboratory - source [18]

The design is based on PLC Siemens S7-200 and PC with SCADA software SIMATIC WinCC. The programming of the controller is done by SIEMENS Step7 Microwin. It can use

two languages - a list of commands and ladder diagram. The connection between the PLC and the PC is done via RS485 interface converter and PPI (Point-to-Point-Interface) connection to RS232 port. Remote access is done by a Web server whose Web interface is built using Visual Studio ASP.NET. At one time, only one user can use the control functions by registering with a user name and password.

B. PLC WEB server approach

We will look at another example of a laboratory that is based on the programmable logic controller Siemens S7-200. The laboratory has several workstations for experiments [19]. Each workstation consists of a digital oscilloscope Tektronics TDS3014B, equipped with an Ethernet interface, a training model of a rectifier with change of phase angle and PLC controller (Fig. 4). Workstations are connected by a switch to a personal computer that combines the functions of SCADA and Web server. The use of Ethernet technology has its advantages because it is supported by multiple devices, besides almost every programming language allows the creation of programs with Internet connectivity [13].

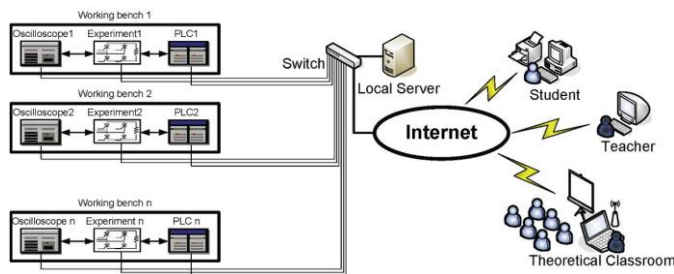


Fig. 4 Remote laboratory architecture - source [19]

In [20] a low cost, easy to implement system that is described. It uses (Fig. 5) a PLC controller VIPA and industrial router eWON4005CD.

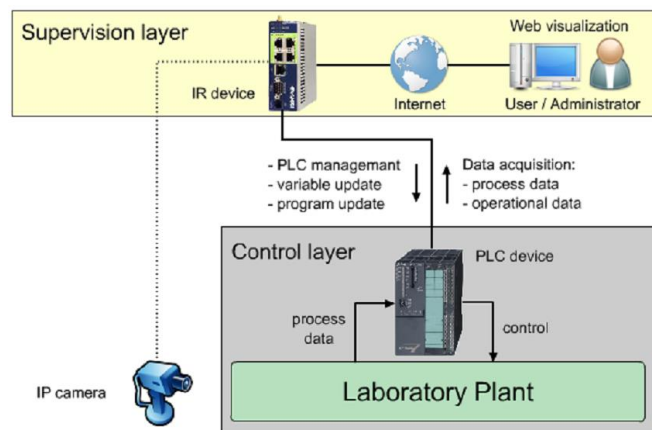


Fig. 5 Operational architecture of on-line laboratory plant - source [20]

The PLC and the laboratory equipment form the control level. To create a control program Siemens Step 7 software environment is used.

PLC controller is connected to the Internet through a router that supports Web and FTP server, remote management of PLC, data logging and translation of industrial protocols such as Modbus and Profibus. The user can connect via browser running on the personal computer or even a smartphone. The router and the connected user form the supervisory layer. The implementation of Web GUI used HTML5, CSS, jQuery and XML. Created experimental installation shows that traditional approaches to building remote laboratory equipment can be simplified with the use of appropriate software and hardware resources.

In [21] we see an example of industrial control system, which uses optical fiber link between PLC controllers and remote control room, in which is located the main terminal. The use of fiber optic cable has a number of advantages such as high speed transfer, resistance to electromagnetic interference, small physical size. The described system uses several HMI stations, so changing a parameter or occurrence of alarm can be registered by all operators, which makes it a good protection to human error.

In other project [22] the Global System for Mobile Communications is chosen for the wireless communication. The system topology is shown on Fig. 6. Continuous monitoring of the process can be done through the SCADA software by interfacing it with an industrial modem to PLC. This could update us continuously about the process parameters. The type of PLC chosen here is 1762 MicroLogix 1200 Controllers. It contains isolated RS-232/RS-485 combo port for serial and networked communication. Tag Database, generated by SCADA software maintains a list of tags which are configured with an address, which could be either input address or output address from the PLC. These addresses are continuously monitored by the SCADA to provide a continuous real time representation of the process. There is possibility to monitor to certain tags directly from GSM mobile phone by using short message services (SMS).

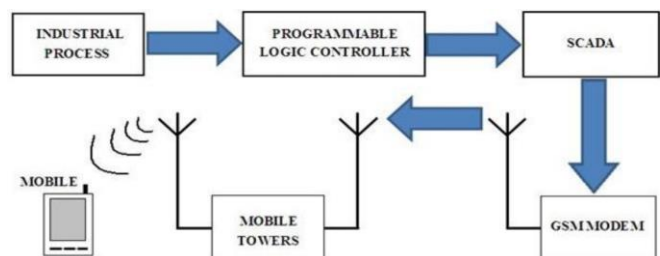


Fig. 6 - The remote monitoring system topology - source [22]

In [23] a SCADA/PLC system is used to control a whole oil refinery instead of the conventional control through DCS. It consists of four main units: a crude oil storage unit, a crude oil pretreatment unit, a distillation unit and products storage/dispatch unit (Fig. 7). The Multipoint Interface/Decentralized Peripherals (MPI/DP) connection in main control loop is used, instead of Ethernet connection by the reason of higher data transfer speed through the system. Fig. 7 shows the GUI home page with the operation sequence diagram.

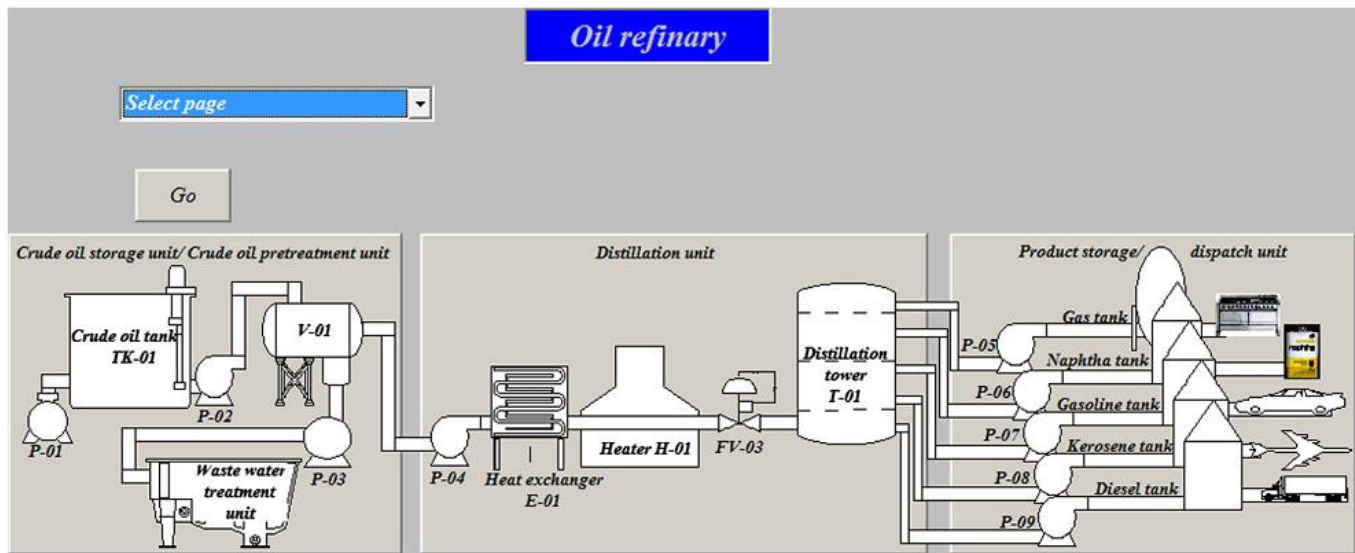


Fig. 7. The oil plant home page GUI with the operation sequence diagram - source [24]

C. PC – DAQ board or embedded control board approach

Another approach used in the implementation of specialized SCADA systems is to use a combination of computer as the main terminal unit connected to Data Acquisition Board (DAQ board) or a specialized embedded system controller, designed for specific needs. If only DAQ boards are connected the system is a centralized control type. In a case, when specialized embedded system controllers are also included and performed local control functions – the system is distributed control type. The last scenario is typically applied when high speed equipment is controlled in real time mode, which requires a high exchange rate of information between controller and equipment.

In [24] a microcontroller system for regulating the temperature, developed by board with digital and analog inputs and outputs is described. It is based on a 8-bit microcontroller ATMEGA 2560 from the company Atmel. The supervision level consists of PC with SCADA software Vijeo Citect v7.2 from Schneider Electric. Communication between the board with microcontroller and computer is done through the Modbus protocol running on the physical layer RS232. Temperature control is achieved by proportional control of the fan speed or by turning it on/off. The authors are proposing system with low cost and good scalability, because with the necessary hardware and software tools the inputs and outputs could be easily increased, in case to meet the needs of running a small factory. Such solution with microcontroller for temperature measurement is described in [25] where a LabVIEW is used as SCADA software and the connection to the PC is made also by RS232 interface.

A hybrid heating system, consisting of solar collectors, thermal accumulators based on phase change material and borehole heat exchangers is described in [26] Dozens of parameters are measured - temperatures, flow rates, electrical power and energy, solar radiations and others. The SCADA system consists of DAQ board LabJack™ UE9, connected to a

computer by Ethernet with option to connect to Wi-Fi router. The various sensors and actuators are connected to a dedicated signal conditioning and interface board, which converts the signals so that they are compatible with the inputs and outputs of the DAQ module. The Data collection and management of the different modes of the system operation is performed by the software. The front panel of the operator interface is presented on Fig. 8.

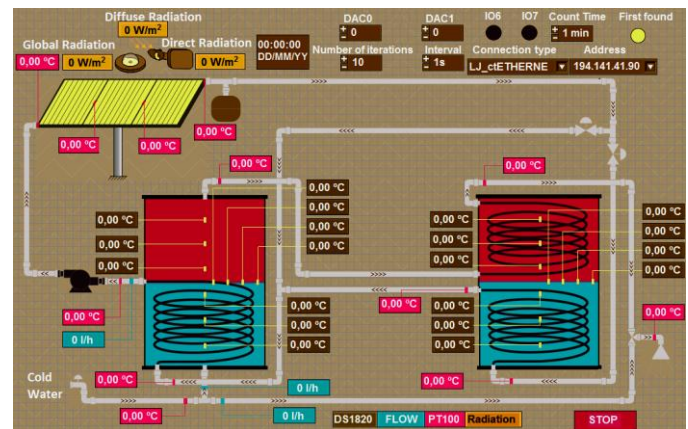


Fig. 8 The HMI panel for controlling a hybrid thermal system - source [24]

LabVIEW application generates on a WEB server the secured html page with the same HMI monitoring screen and an ActiveX controls. It is available through the Internet from the remote computers. Another page is generated to be displayed by the smartphone browser.

In [27] a different type of system is described in terms of HMI operator interface. The system is used for the production of composite materials by pulsed plasma sintering by performing control and monitoring of the manufacturing process. The main element of the system is PLC controller with a processor RX3i CPE305. The controller consists of separate modules - serial communication MODBUS, digital inputs for 24V, relay outputs, Ethernet module with analog

inputs. As operator interface is used Touch-screen display, working with SCADA Software Proficiency, who has the capability to operate on different platforms.

V. CONCLUSIONS

Development of SCADA systems, in recent years indicates the presence of several distinct trends. Increasingly heterogeneous structure applies of their construction, both in terms of hardware resources, and in terms of communication networks used in them.

The most often-purpose structure in large SCADA systems distributed in large geographical regions is PC – PLC approach with integrated WEB server.

In smaller systems, particularly in research laboratories and laboratories for distance learning often applied PC – DAQ board or embedded control board approach.

The transmission of communication through the Internet allows global access and remote monitoring of the system. This has already become a standard feature in modern SCADA systems. Web-based SCADA system uses the Internet to transfer data between the RTUs and the MTU and/or between the operators' workstations and the MTU. The connection over the Internet requires the use of additional resources to protect the system from unauthorized access and hacker attacks.

Wireless communications is rapidly growing segment of the communications industry, with the potential to provide high-speed and high-quality information. More and more often in SCADA systems a wireless communication technologies are used for short range (WiFi, Bluetooth, ZigBee), and for long range (Private Radio Networks - PRN, Satellite, 3G, 4G) data transmission. Wireless SCADA replaces or extends the fieldbus to the Internet. It is required in those applications when wireline communications to the remote site is prohibitively expensive or it is too time consuming to construct wireline communications. It can reduce the cost of installing the system. It is also easy to expand.

New trends in teaching and learning strategies, in which blended learning is one of the most promising, can benefit from remote laboratories as valuable pedagogical add-ons. Experiments conducted in a real laboratory are undoubtedly the essential learning experience. However, remote laboratory facilities allow the students to access the laboratory infrastructure at nonworking hours. From the point of view of the teaching institution that offered services, this pleases the students very much.

VI. ACKNOWLEDGEMENT

The work was financially supported by internal project at the Technical University of Sofia to support PhD students ref. No:152ΠД0045-24/ 27.03.2015.

REFERENCES

- [1] Branislav Atlagić, Mihalj Šagi, "Proposal of a modern SCADA system architecture", *Proc. of 19th Telecommunications forum TELFOR 2011* Serbia, Belgrade, November 22-24, 2011, pp. 1430 – 1433.
- [2] E. Stoilov, "Security in process control systems", Sofia, 2010, pp. 3 – 5.
- [3] Stuart A. Boyer, "Supervisory control and data acquisition, 3rd edition" ISA-The Instrumentation, Systems, and Automation Society, ISBN 1-55617-877-8, 2004, pp. 9 – 15.
- [4] Minkyu Choi, "A Study of the Evolution of Wireless Communications for SCADA Systems", *CST 2013, ASTL Vol. 27*, 2013 © SERSC 2013, pp. 192 – 195.
- [5] Shahzad, A., S. Musa, A. Aborujilah and M. Irfan, "The SCADA review: system components, architecture, protocols and future security trends", *American Journal of Applied Sciences* 11 (8): 1418- 1425, ISSN: 1546-9239, doi:10. 3844 /ajassp. 2014. 1418. 1425, 2014, pp. 1418 – 1425.
- [6] Aditya Bagri, Richa Netto, Dhruvil Jhaveri, "Supervisory Control and Data Acquisition", *International Journal of Computer Applications* (0975 – 8887) Volume 102 – No.10, September 2014, <http://research.ijcaonline.org/volume102/number10/pxc38987/97.pdf>.
- [7] Technical manual TM 5-601, "Supervisory control and data acquisition (SCADA) systems for command, control, communications, computer, intelligence, surveillance, and reconnaissance (c4isr) facilities", Headquarters, department of the army, Washington, DC, USA, 21 January 2006, pp. 3-1 – 3-4.
- [8] Mehdi J. Marie, Ghaida A. AL-Suhail, Hussein T. Kadhim, "Developing Al-Najaf Cement Plant using Wireless SCADA System", *International Journal of Computer Applications* (0975 – 8887) Volume 64– No.13, February
- [9] Technical information bulletin NCS TIB 04-1 "Supervisory Control and Data Acquisition (SCADA) Systems", Office of the manager national communications system P.O. Box 4052 Arlington, VA 22204-4052, October 2004, pp. 4 – 14.
- [10] Mohamed N. Lakhoua, "Application of Functional Analysis on a SCADA System of a Thermal Power Plants" *Advances in Electrical and Computer Engineering* Volume 9, Number 2, 2009, doi: 10.4316/AECE.2009.02014, pp. 90 – 98.
- [11] Savaş Şahin, "Modbus-Based SCADA/HMI Applications", *Journal of Information Technology and Application in Education* Vol. 2 Iss. 2, June 2013, pp. 61 – 66, www.jitae.org.
- [12] Jay Makhija, "Comparison of protocols used in remote monitoring: DNP 3.0, IEC 870-5-101 & Modbus", M.Tech. Credit Seminar Report, Electronics Systems Group, EE Dept, IIT Bombay, November 2003, sem03_paper_03307905.pdf.
- [13] Dong-joo Kang and Rosslin John Robles, "Compartmentalization of Protocols in SCADA Communication", *Int. Journal of Advanced Science and Technology* Volume 8, July, 2009, pp 27 – 36.
- [14] Jean-Pierre Thomesse, "Fieldbus technology in industrial automation", *Proceedings of the IEEE, Institute of Electrical and Electronics Engineers (IEEE)*, 2005, 93 (6), pp.1073-1101.
- [15] <http://www.ni.com/white-paper/14162/en/>
- [16] Li Pengfei and Nie Luhua. 2009. "Remote Control Laboratory Based On LabVIEW". In *Proceedings of the 2009 Second International Conference on Intelligent Computation Technology and Automation - Volume 04 (ICICTA '09)*, Vol. 4. IEEE Computer Society, Washington, DC, USA, pp. 84-87.
- [17] <http://www.ni.com/labview/>.
- [18] Zafer Aydogmus, Omur Aydogmus, "A Web-based Remote Access Laboratory using SCADA", *IEEE Transactions on Education*, Vol. 52, No. 1, February 2009, pp 126 – 132.
- [19] Rui Marques, Jaime Rocha, Silvano Rafael, J. F. Martins, "Design and Implementation of a Reconfigurable Remote Laboratory Using Oscilloscope/PLC Network for WWW Access", *IEEE Transactions on industrial electronics*, Vol. 55, No. 6, June 2008, pp 2425 – 2432.
- [20] Halás Rudolf, Durina Pavol. "Remote Laboratory Plant Control", *STOC 2012 - Student competition*, Ostrava, Czech Republic, 2012, <http://akce.fs.vsb.cz/2012/stoc2012/>.
- [21] Rajeev Kumar, M.L.Dewal, "Multi-Supervisory Control and Data Display", *International Journal of Computer Applications* (0975 – 8887) Vol. 2 – No.1, May 2010, <http://citeseerx.ist.psu.edu/viewdoc/download?doi=10.1.1.206.4898&rep=rep1&type=pdf>
- [22] R. K. Glisten, A. Lakshmi Sangeetha, N. Bharathi. "Remote Monitoring of PLC- SCADA based Industrial Processes using GSM Technology", *Int. Conf. on Innovations In Intelligent Instrumentation, Optimization And Signal Processing "ICIIOISP-2013"* pp. 15-20.

- [23] Iman Morsi, Loay Mohy El-Din, "SCADA system for oil refinery control," *Measurement*, 47, 2014, pp. 5-13.
- [24] Mayur Avhad, Vinit Divekar, Harshad Golatkar, Sanket Joshi, "Microcontroller based Automation system using Industry standard SCADA", *Annual IEEE India Conference (INDICON) 2013*.
- [25] Mr. Neeraj Khera, Sumit Balgavhar, "Design of microcontroller based wireless SCADA system for real time data", *UACEE International Journal of Advances in Electronics Engineering Volume 2 : Issue 1 ISSN 2278 - 215X (Online)*, pp 18 – 20.
- [26] R. Popov, A. Georgiev. SCADA system for study of installation consisting of solar collectors, phase change materials and borehole storages. *Proc. of the 2nd Int. Conf. on Sustainable Energy Storage, June 19-21, 2013, Trinity College Dublin, Ireland*, pp. 206-211.
- [27] B. Sakowicz, D. Makowski, P. Sekalski, P. Marciniak, R. Kotas, G. Skrabalak, R. Talar, M. Rosinski, and A. Napieralski, "Control and Monitoring System for Composite Materials Fabrication Based on PPS Method", *International Journal of Modeling and Optimization*, Vol. 3, No. 5, October 2013, pp 445 – 449.

BIOGRAPHIES



STEFAN LISHEV was born in Plovdiv, Bulgaria, in 1985. He received the M.S degree (Computer Systems and Technologies) in Technical University of Sofia, branch Plovdiv, in 2010. From 2009 to 2013, he was software engineer at "RGB&" Ltd. He is National Instruments Certified LabVIEW Associate Developer since 2014.

His research interest are in Embedded Systems, Software Engineering, High Fidelity Audio Applications, Digital Signal Processing, Artificial Intelligence.



RUMEN POPOV was born in Plovdiv, Bulgaria, in 1964. He received the M.S. degree (Automatic Control Systems) in Technical University of Tula, Russia, in 1990 and the Ph.D. in Technical University of Ruse, Bulgaria in 2009.

From 1990 to 1991, he was a Research Engineer with the Aviotronics SA, Plovdiv at Radio Electronic Systems department. Since 1991, he has been an Assistant Professor with the Control Systems Department, Technical University of Sofia, branch Plovdiv. He became an associated professor

at the Technical University of Sofia, Bulgaria in 2011. At present hi is an associated professor at Department of Electronics, Communications and Information Technologies in Plovdiv University "Paisii Hilendarski" He is the author of more than 53 articles. His research interests include Measurement and Automation, Renewable Energy Systems, Sun - Tracking systems.

His main courses are in Measurement Systems, SCADA Systems, and Aviation Electricity and Electronics. Assoc. Prof. Popov is a member of the Bulgarian Geothermal Association since 2011.



ALEKSANDAR GEORGIEV was born in Dobrich, Bulgaria in 1958. He received the MSc degree in Mechanical Engineering from the Technical University (TU) of Sofia, Bulgaria in 1981 and received the PhD degree in 1988 at the same university.

His research interests are in Renewable Energy Sources, Solar Heating and Cooling Systems, Sun - Tracking systems and Shallow Geothermal Energy.

He became a full professor at the European Polytechnic University in Pernik (EPU), Bulgaria.

Prof. Georgiev is a member of the Bulgarian Geothermal Association since 2011. He is presently active at the Department of Mechanics at the TU Sofia, branch Plovdiv in Bulgaria.

His lectures (in Bulgarian and English) are in the field of the Thermal Energy Systems, they are hold in both universities (EPU Pernik and TU Sofia).



ISSN: 2147- 284X
Vol: 3
No: 3
Year: December 2015

CONTENTS

- Y. Calleecharan;** Spectral analysis and second-order cyclostationary analysis of the non-stationary stochastic motion of a boring bar on a lathe,103-114
- Metia and S. Ghosh;** Fuzzy based DG allocation for Loss Minimization in a Radial Distribution System,.....115-123
- Y. Calleecharan, J.O. Aidanpää, and J.R. Brauer;** No-load electromagnetic simulations of a hydropower generator considering the effect of rotor whirling,.....124-134
- N. Vasilev and A. Bosakova-Ardenska;** A New Sorting Algorithm with filling to the left and right,135-141
- C. Bakir;** Classification of ECG Signals By the Neighborhood Feature Extraction Method, ..142-145
- E. Hamiti, T. Berisha and F. Peci;** In-Home PLC Coexistence with Wi-Fi and Ethernet access Networks,146-153
- K. Lenin, B.R. Reddy, and M.S. Kalavathi;** Blending of Genetic Algorithm with Fletcher Reeves Method to Solve Reactive Power Problem,.....154-157
- N. Ben Si Ali and N. Benalia;** Design of a MRAS, Speed and Flux Estimators used in Sensorless Control of Induction Motors,.....158-163
- S. Lishev, R. Popov, and A. Georgiev;** Laboratory SCADA Systems – the State of Art and the Challenges,164-170

BALKAN JOURNAL OF ELECTRICAL & COMPUTER ENGINEERING

(An International Peer Reviewed, Indexed and Open Access Journal)

Contact

Istanbul Technical University
Department of Electrical Engineering,
Ayazaga Campus, Maslak, Istanbul-Turkey

Web: <https://www.bajece.com>
<http://dergipark.ulakbim.gov.tr/bajece/>

e-mail: editor@bajece.com
bajece.editor@gmail.com

